NONLINEAR DYNAMICAL ASPECTS of THE DIELECTRIC WAVEGUIDE SURFACE PLASMON JOSEPHSON JUNCTION

by

Yasa Ekşioğlu Özok

A Thesis Submitted to the
Graduate School of Sciences and Engineering
in Partial Fulfillment of the Requirements for
the Degree of

Doctor of Philosophy

in

Physics

Koç University

September, 2011

Koç University

Graduate School of Sciences and Engineering

This is to certify that I have examined this copy of a doctoral dissertation by

Yasa Ekşioğlu Özok

and have found that it is complete and satisfactory in all respects,

and that any and all revisions required by the final

examining committee have been made.

Chair of Supervisory Committee:

Reading Committee:

_____

Assist. Prof. Kaan Güven

_____

Assoc. Prof. Özgür E. Müstecaplıoğlu

_____

Assoc. Prof. M. Özgür Oktel

_____

Assoc. Prof. Alper Tunga Erdoğan

_____

Assist. Prof. Levent Subaşı

Date: _____

To my mother, my grandmother and my husband

ABSTRACT

In this thesis, we formulate and investigate the dynamical properties of a coupled optic-plasmonic system based on classical treatment, which consists of an optical soliton in a nonlinear dielectric waveguide and a surface-plasmon along a metal surface. Particular to this system, the coupling parameter depends on the soliton amplitude, and thus becomes an inherent dynamical parameter rather than being a coupling "constant". This is an essential property that differentiates this two-level system from others. We formulate the dynamics of the system by the fractional population imbalance, and the relative phase between the soliton and surface-plasmon modes. The fractional population imbalance is a measure of how the total electric field intensity (or the number of photons) is divided between the soliton and surface plasmon modes. Remarkably, this formulation reveals a surprising analogy to the dynamics of Bosonic Josephson junction (BJJ) of weakly coupled Bose-Einstein condensates of atomic physics at very low temperatures. In the BJJ, the atoms (bosons) populate a two level system formed by a double-well optical trap. The wells are separated by a thin barrier (junction) which allows tunneling between the two levels. There, however, the coupling between the levels depends on the barrier, which is constant or tunable externally. A further analogy is established with a classical mechanical system known as the momentum shortened pendulum. The main model parameters consists of the surface-plasmon propagation constant, the nonlinearity of the dielectric medium, and the distance between the soliton and the metal surface. We employ the linear stability analysis method to exploit the dynamical features in the phase-space for certain regimes of these model parameters. Fixed points are determined and the eigenvalues of the respective Jacobian matrix are calculated. Phase space trajectories are determined and compared to that of the BJJ system. The dissipation effects

are investigated by introducing a phase-velocity damping term (which corresponds to a damping to the angular velocity of the pendulum in the mechanical analogue). Finally, we investigated damped-driven system to observe Shapiro-resonances in the stroboscopic phase portrait, under weak damping. The effect of the values of the distance between surface plasmon and optical soliton on Shapiro resonances is discussed. In addition to this, the Shapiro resonances are investigated by increasing the value of the damping in the system.

ÖZETÇE

Bu tez çalışmasında, nonlineer dielektrik dalga kılavuzundaki optik soliton ile metal yüzey boyunca yer alan yüzey plasmonlarının oluşturduğu optik-plazmonik bağlı sistemin dinamik özelliklerini, klasik çerçevede formüle ederek araştırdık. Bu sisteme özgü olarak, bağlama parametresi solitonun genliği ile değişmektedir ve bu sebeple sabit bir değerden çok dinamik bir parametre olarak düşünülmelidir. Bu durum, iki seviyeli sistemi diğer sistemlerden ayıran esas özelliktir. Sistemin dinamiğini, fraksiyonel popülasyon oransızlığı ile soliton ve plazmon modlar arasındaki bağıl faz terimini kullanarak formüle ettik. Burada fraksiyonel popülasyon oransızlığı, toplam elektrik alan şiddetinin (veya foton sayısının) soliton ve yüzey plazmon modlar arasında nasıl bölündüğünü ölçmektedir. Bu formülasyon ile atomik fizikteki çok düşük sıcaklıklarda zayıf etkileşen Bose-Einstein yoğuşmasının Bozonik Josephson eklemi (BJJ) dinamiğine şaşırtıcı bir benzerlik ortaya koymaktadır. BJJ sistemlerinde, atomlar (bozonlar) çift kuyu optik tuzaklama ile oluşturulmuş iki seviyeli sisteme yerleşirler. Bu kuyular, iki seviye arasında tünellenmeye izin veren ince bir bariyer (jonksiyon) ile ayrılmaktadır. Ancak, bu seviyeler arasındaki bağlama sabit ya da dışarıdan ayarlanabilen bir değer alan bariyere bağlıdır. Klasik mekanik sistemlerdeki momentumu kısaltılan sarkaç sistemini ele alarak benzerlik kurulabilmektedir. Modelin temel parametreleri; yüzey plazmon ilerleme sabiti, ortamın nonlineer dielektrik sabiti ve soliton ile metal yüzey arasındaki uzaklıktan oluşur. Biz bu modelde belirli parametreler için faz uzayının dinamik özelliklerini anlamak amacıyla lineer stabilite analizi metodunu ele aldık. Burada sabit noktalar bulunarak bunlara karşılık gelen Jacobi matrisinin özdeğerleri hesaplandı. Faz uzayının yörüngeleri tanımlanarak BJJ sistemi ile karşılaştırıldı. Sistemdeki dağılma etkileri, faz-hız sönümlenme terimi (sarkacın açısal hızının sönümlenmesine karşılık gelir) dinamik denklemlerde kul-

lanılarak araştırıldı. Son olarak, Shapiro rezonanlarını gözlemleyebilmek için sistemimizi zayıf sönümlenme ve dış sürücü etkisi altında ele aldık. Sistemi, stroboskopik faz uzayında inceledik. Yüzey plazmonlar ve optik solitonlar arasındaki uzaklığın değerinin Shapiro rezonanslarına etkisini tartıştık. Buna ek olarak, sistemde sönümlenme teriminin değerini artırarak Shapiro rezonanslarını inceledik.

ACKNOWLEDGMENTS

First of all, I would like to thank my supervisor Assist. Prof. Kaan Güven whose encouragement, guidance and support from the initial to the final level enabled me to develop an understanding of my research work. During thesis work, his wide knowledge and great efforts to explain things clearly and simply significantly helped me to understand and develop the work presented. And, I also acknowledge for his endeavor.

I would like to thank to my thesis committee member Assoc. Prof. Özgür E. Müstecaplıoğlu for his advice, suggestions and crucial contribution throughout my PhD study. The scientific discussions with him helped me for progressing.

I would like to thank my thesis committee member Assoc. Prof. M. Özgür Oktel for scientific discussions and suggestions on my research subject during our periodic meetings.

I would like to thank my thesis committee members Assoc. Prof. Alper Tunga Erdoğan and Assist. Prof. Levent Subaşı for their patience and tolerance.

The department of Physics of Koç University, has provided an excellent professional environment for my research. I enjoyed very much to study at Koç University, where any kind of financial, technical, or mental support is unexceptional. I would like to thank all the academic and the administrative personel of Koç University, especially Prof. Dr. Tekin Dereli, director of the Graduate School of Sciences and Engineering.

I would like to thank to graduate students my great friends Melisa Natali (Çizmeciyan) Sözüdoğru, Neslihan Oflaz, Fatih Pelik, Neşe Aral, Seçil Gürkan, Duygu Can, Ahad Khaleghi, Ramazan Uzel, A. Ümit C. Hardal, Ulaş S. Gökay, Şeyda İpek, Mustafa Gündoğan, Utkan Gündoğdu, Sevilay Bilgin, Ceren Yılmaz, Ali Baş, Can Güven, Arif Engin Çetin and many others. We had many enjoyable hours during the coffee breaks

and lunch times.

I would like to thank my mother. She has always been with me supporting my ideas, my beliefs and my way of life. I consider myself lucky she encouraged me about all decisions in my career.

Last but not least, I would like to thank to my husband Ferhat Özok, for always being with me, encouraging, supporting, and tolerating me during my doctoral studies.

TABLE OF CONTENTS

List of Tables **xii**

List of Figures **xiii**

Nomenclature **xiv**

Chapter 1: Introduction **1**

1.1 Surface Plasmons 3

1.2 Optical Solitons 4

1.3 Josephson Junction Systems in Physics 7

1.3.1 Superconducting Josephson Junction (SJJ) 8

1.3.2 Bosonic Josephson Junction(BJJ) 12

Chapter 2: Theoretical Model and Dynamical Stability Analysis **16**

2.1 Description of the Model 16

2.2 Bosonic Josephson Junction Formulation 18

2.2.1 Bosonic Josephson Junction 20

2.2.2 Non-Rigid Pendulum Analogy 21

2.3 Linear Stability Analysis of a Dynamical System 23

Chapter 3: Dynamical Analysis : Results **35**

3.1 Fixed Point Analysis 35

3.2 Phase Space Analysis 37

3.3 Phase Space Comparison with Bosonic Josephson Junction Model . . 42

3.4 Spatial Propagation Properties 42

3.4.1 Plot and Analysis of $Z(\xi)$, $\phi(\xi)$, and $q(\xi)$ 42
3.4.2 Total Wave Function 44
3.5 Experimental Aspects 48

Chapter 4: Dissipative DWSP-JJ Model **50**
4.1 Dissipative Model 50
4.2 Phase Space Analysis 51
4.3 Spatial Propagation Properties 53

Chapter 5: Shapiro Effect **58**
5.1 Shapiro Resonances in Damped Driven BJJ systems 60
5.2 Shapiro Resonaces in Damped Driven DWSP-JJ System 61

Chapter 6: Conclusion and Outlook **72**
6.1 Outlook 73

Appendix A: The Linerization of coupled harmonic oscillator Equations **74**

Appendix B: The Dynamical Equations of the DWSP-JJ in Bosonic Josephson Analogy **76**

Bibliography **78**

Vita **84**

LIST OF TABLES

LIST OF FIGURES

1.1 Schematic presentation of charges and electromagnetic field of surface plasmon propagating in x direction. On the right side electric field E_z is shown. H_y shows the magnetic field in y direction of this p-polarized wave [17, 18]. 4

1.2 Schematic presentation of soliton propagation [24]. 5

1.3 Schematic showing the spatial beam profiles (a) beam self-focusing (b) normal beam diffraction (c) soliton propagation [33]. 7

1.4 Schematic diagram for DC Josephson effect. Two superconductors SI and SII are separated by a very thin insulator (denoted by green). DC Josephson supercurrent (up to a maximum value Ic) flows without dissipation through the insulating layer [47]. 9

1.5 Schematic diagram for AC Josephson effect with applied finite DC voltage across both the ends [47]. 9

1.6 Schematic of a josephson Junction. S_L and S_R are left and right superconductors. Ψ_L and Ψ_R are left and right pair wavefunctions [38]. 10

1.7 Schematic view of SJJ model with cooper pair representation [38]. . . 10

1.8 Bose Einstein condensation of Rb^{87} atoms, as observed by absorption of laser light [54, 55]. At $T \simeq 200nK$ a macroscopic fraction of atoms condenses, corresponding to the central peak [57]. 12

1.9 Asymmetric double-well trap for BEC N_1, N_2 the number of particles and the E_1^0 and E_2^0 the on site energies of trap 1 and 2 respectively [38, 59] 13

2.1 Schematic view of the coupled surface plasmon optical soliton model, d is the distance between the metal and the soliton propagation axis. The lateral field profiles $|\Psi_p^2|$ and $|\Psi_s^2|$ are plotted. 17
2.2 Schematic view of the Bose-Einstein condensate in a double-well trap(Figure taken from Ref. [62]). 19
2.3 Phase space trajectories (*Left panel*) with corresponding real space motions of the non-rigid pendulum (*Right panel*) different trajectories are expressed with different colors Note the fixed points for $\phi = 0$ and $\phi = \pi$ modes around which closed (red, black, violet) and open (green, blue, orange) trajectories are shown(Figure taken from Ref. [57]). . . 22
2.4 The fixed points Z with $kd = 3$, $0.05 < \Lambda < 0.175$ and $0.1 < \nu_p < 0.35$ (a) $\phi = 0$, (b)$\phi = \pi$. 26
2.5 The fixed points Z with $kd = 6$, $0.05 < \Lambda < 0.175$ and $0.1 < \nu_p < 0.35$ (a) $\phi = 0$, (b)$\phi = \pi$. 26
2.6 The fixed points Z with $kd = 12$, $0.05 < \Lambda < 0.175$ and $0.1 < \nu_p < 0.35$ (a) $\phi = 0$, (b)$\phi = \pi$. 27
2.7 The Jacobian eigenvalue of the fixed point for $\phi = 0$ with $kd = 3$, $0.05 < \Lambda < 0.175$ and $0.1 < \nu_p < 0.35$ (a) real part is zero (b) imaginary part stable single fixed point 28
2.8 The Jacobian eigenvalue of the fixed point for $\phi = 0$ with $kd = 6$, $0.05 < \Lambda < 0.175$ and $0.1 < \nu_p < 0.35$ (a) real part is zero (b) imaginary part stable single fixed point 28
2.9 The Jacobian eigenvalue of the fixed point for $\phi = 0$ with $kd = 12$, $0.05 < \Lambda < 0.175$ and $0.1 < \nu_p < 0.35$ (a) real part is zero (b) imaginary part stable single fixed point 29

2.10 The Jacobian eigenvalue of the first fixed point for $\phi = \pi$ with $kd = 3$, $0.05 < \Lambda < 0.175$ and $0.1 < \nu_p < 0.35$ (a) real part of eigenvalues are zero (b) imaginary part stable fixed point. For the second fixed point (c) real part is not zero at certain Λ and ν_p, so unstable fixed point (d) eigenvalues are zoomed for $0.161 < \Lambda < 0.171$ and $0.165 < \nu_p < 0.185$ (e) imaginary part of eigenvalues are zero. For the third fixed point (f) real part is zero (g) $\Lambda > 0.15$ and $0.1 < \nu_p < 0.35$ imaginary stable fixed point (h) eigenvalues are zoomed for $0.165 < \Lambda < 0.169$ with $0.165 < \nu_p < 0.175$. 30

2.11 The Jacobian eigenvalue of the first fixed point for $\phi = \pi$ with $kd = 6$, $0.05 < \Lambda < 0.175$ and $0.1 < \nu_p < 0.35$ (a) real part is zero (b) imaginary part stable fixed point. For the second fixed point(c) real part unstable fixed point for certain Λ, and ν_p (d) imaginary part is zero. For the third fixed point (e) real part is zero (f) for certain Λ, and ν_p imaginary part stable fixed point. 33

2.12 The Jacobian eigenvalue of the first fixed point for $\phi = \pi$ with $kd = 12$, $0.05 < \Lambda < 0.175$ and $0.1 < \nu_p < 0.35$ (a) real part zero (b) imaginary part stable fixed point. For the second fixed point For the second fixed point(c) real part unstable fixed point for certain Λ, and ν_p (d) imaginary part is zero. For the third fixed point (e) real part is zero (f) for certain Λ and ν_p imaginary part stable fixed point. 34

3.1 $f(Z)$ (Eq. **??**) for zero-phase modes plotted at $\nu_p = 0.15$ with various values of ΔE and (a) $kd = 3$ (b) $kd = 6$ and (c) $kd = 12$ The critical points are the roots of $f(Z) = 0$. 36

3.2 $f(Z)$ (Eq. **??**) for π-phase modes plotted at $\nu_p = 0.15$ with various values of ΔE and (a) $kd = 3$ (b) $kd = 6$ and (c) $kd = 9$ The critical points are the root(s) of $f(Z) = 0$. 36

3.3 Phase-space trajectories of DWSP-JJ with $kd = 12$, $\nu_p = 0.15$ (a) $\Delta E = 0$, $\Lambda = 0.15$ (b) $\Delta E = 0.025$, $\Lambda = 0.175$ (c) $\Delta E = -0.025$, $\Lambda = 0.125$. 37
3.4 Several phase-space trajectories of DWSP-JJ system for $\nu_p = 0.1$, $kd = 6$ (a) $\Lambda = 0.07$, (b) $\Lambda = 0.1$, (c) $\Lambda = 0.14$. 39
3.5 Several phase-space trajectories of DWSP-JJ system for $\Lambda = 0.1$, $kd = 6$ (a) $\nu_p = 0.1$, (b) $\nu_p = 0.2$ (c) $\nu_p = 0.3$. 39
3.6 Several phase-space trajectories of DWSP-JJ system for $\Delta E = 0$, $\nu_p = 0.1$, $\Lambda = 0.1$, (a) $kd = 3$, (b) $kd = 6$, (c) $kd = 12$. 41
3.7 Several phase-space trajectories of DWSP-JJ system for (a)$\Delta E = -0.025$, $\nu_p = 0.15$, $kd = 6$, (b) $\Delta E = 0.025$, $\nu_p = 0.15$, $kd = 6$, (c) $\Delta E = 0.025$, $\nu_p = 0.15$, $kd = 3$. 41
3.8 Comparison of the phase-space trajectories of (a) BJJ ($q \equiv 0.03$, $\Delta E = 0$, $\Lambda = 0.15$) and (b) DWSP-JJ ($kd = 6$, $\Delta E = 0$, $\Lambda = 0.15$) and (c) SJJ models 43
3.9 Spatial propagation of (a) Z (b) $q(Z)$, and (c) ϕ for initial values of $\phi(0) = 0$ and $Z = -0.997$(blue-triangle), $Z = 0.03$(red-circle), $Z = 0.879$(pink-square), $Z = 0.997$ (black-dashed line). 45
3.10 Spatial propagation of(a) Z (b) $q(Z)$, and (c) ϕ for initial values of $\phi(0) = \pi$ and $Z = -0.997$(blue-triangle), $Z = -0.942$(red-circle), $Z = -0.69$(pink-square), $Z = 0.96$ (black-dashed line). 45
3.11 The corresponding phase portraits for (a) $Z = -0.997$, $Z = 0.03$, $Z = 0.997$ at $\phi(0) = 0$ (b) $Z = -0.997$, $Z = -0.69$, $Z = 0.96$ at $\phi(0) = \pi$. 46
3.12 $|\Psi|^2$ vs kx and ξ. $\Delta E = -0.025$, $\nu_p = 0.15$, $kd = 6$, $\Lambda = 0.125$ (a) $\phi(0) = 0$ $Z(0) = 0.997$, (b) $\phi(0) = 0$ $Z(0) = 0.03$,(c) $\phi(0) = 0$ $Z(0) = -0.997$. 47

3.13 $|\Psi|^2$ vs kx and ξ. $\Delta E = -0.025$, $\nu_p = 0.15$, $kd = 6$, $\Lambda = 0.125$ (a) $Z(0) = 0.96$, $\phi(0) = \pi$ (b) $Z(0) = -0.69$, $\phi(0) = \pi$ (c) $Z(0) = -0.997$, $\phi(0) = \pi$. 48

4.1 Phase portraits of the damped system $Z(0) = -0.63$, $\phi(0) = -3.2$, $\Delta E = -0.025$, $\Lambda = 0.125$, $kd = 6$ (a) $\zeta = 0.005$, (b) $\zeta = 0.05$ (c) $\zeta = 0.15$. 52

4.2 Phase portraits of the damped system $Z(0) = -0.25$, $\phi(0) = -0.92$, $\Delta E = -0.025$, $\Lambda = 0.125$, $kd = 6$ (a) $\zeta = 0.05$ (b) $\zeta = 0.15$. 52

4.3 Phase portraits of the damped system $kd = 6$, $\Delta E = -0.025$, $\Lambda = 0.125$ (a) $Z(0) = -0.28$, $\phi(0) = 1$, $\zeta = 0.05$ (b) $Z(0) = 0.96$, $\phi(0) = 1$, $\zeta = 0.15$. 53

4.4 Phase portraits of the damped system $kd = 6$, $\Delta E = -0.025$, $\Lambda = 0.125$ (a) $\phi(0) = -3$, $\zeta = 0.15$ (b) $\phi(0) = 1$, $\zeta = 0.05$. 53

4.5 Propagation of (a) Z , (b) ϕ/π, (c) coupling parameter $q(Z)$ for $Z(0) = -0.63$, $\phi(0) = -3.2$ damped system $\zeta = 5 \times 10^{-3}$, $\Delta E = -0.025$, $\Lambda = 0.125$, $kd = 6$. 54

4.6 Propagation of (a) Z , (b) ϕ/π, (c) coupling parameter $q(Z)$ for $Z(0) = -0.63$, $\phi(0) = -3.2$ damped system $\zeta = 5 \times 10^{-2}$, $\Delta E = -0.025$, $\Lambda = 0.125$, $kd = 6$. 55

4.7 Propagation of (a) Z , (b) ϕ/π, (c) coupling parameter $q(Z)$ for $Z(0) = -0.63$, $\phi(0) = -3.2$ damped system $\zeta = 0.15$, $\Delta E = -0.025$, $\Lambda = 0.125$, $kd = 6$. 55

4.8 Propagation of (a) Z , (b) ϕ/π, (c) coupling parameter $q(Z)$ for $Z(0) = -0.25$, $\phi(0) = -0.92$ damped system $\zeta = 5 \times 10^{-2}$, $\Delta E = -0.025$, $\Lambda = 0.125$, $kd = 6$. 56

4.9 Propagation of (a) Z , (b) ϕ/π, (c) coupling parameter $q(Z)$ for $Z(0) = -0.25$, $\phi(0) = -0.92$ damped system $\zeta = 0.15$, $\Delta E = -0.025$, $\Lambda = 0.125$, $kd = 6$. 56

4.10 Propagation of (a) Z , (b) ϕ/π, (c) coupling parameter $q(Z)$ for $Z(0) = -0.28$, $\phi(0) = 1$ damped system $\zeta = 0.15$, $\Delta E = -0.2$, $\Lambda = 0.1$, $kd = 6$. 57

4.11 Propagation of (a) Z , (b) ϕ/π, (c) coupling parameter $q(Z)$ for $Z(0) = 0.96$, $\phi(0) = 1$ damped system $\zeta = 0.05$, $\Delta E = -0.2$, $\Lambda = 0.1$, $kd = 6$. 57

5.1 Current-Voltage charactistics of Josephson Junction [42]. 60

5.2 The shapiro resonances in BJJ system ($\bar{z} = 0.1$). Population imbalance $z(t)$ vs t and different collection of initial values of relative phase ϕ. The parameters are $\Lambda = 1 \times 10^4$, $\gamma = 1 \times 10^{-5}$, $\Omega = 1 \times 10^3$, $\epsilon = 100$. 61

5.3 Initial value of population imbalance $Z(0) = 0.15$ with initial value of relative phase $\phi(0) = 9\pi/5$. The parameters $\Lambda = 0.1$, $\zeta = 8 \times 10^{-5}$, $\Omega = 0.01$, $q(Z) = 1 \times 10^{-5}$. The driven case $\varepsilon = 1 \times 10^{-3}$, Shapiro resonances at $\bar{Z} = 0.1$ (blue line). For the undriven case ($\varepsilon = 0$), under damped system decays towards equilibrium (red line). 65

5.4 The shapiro resonances in DWSP-JJ system ($\bar{Z} = 0.1$). Population imbalance Z vs ξ and different collection of initial values of relative phase ϕ. The parameters are $\Lambda = 0.1$, $\zeta = 8 \times 10^{-5}$, $\Omega = 0.01$, $\varepsilon = 1 \times 10^{-3}$, and $q(Z) = 1 \times 10^{-5}$ 66

5.5 Phase portraits of the driven $\varepsilon = 1 \times 10^{-3}$ undamped $\zeta = 0$ system at stroboscopic times $2\pi/\Omega(1 : 4000)$, $\Lambda = 0.1$, $\Omega = 0.01$, (a) $kd = 15$ (b)$kd = 19$ (c) $kd = 24$. 66

5.6 The driven and damped system. Population imbalance vs ξ; $kd = 19$, $\Lambda = 0.1$, $\zeta = 1 \times 10^{-4}$, $\varepsilon = 1 \times 10^{-3}$, $\Omega = 0.01$ (a) $Z(0) = 0.12$, $\phi(0) = 0.4$, $\phi(0) = 0$ (b)= $Z(0) = 0.15$, $\phi(0) = -0.3$, $\phi(0) = 0.8$. . . . 67

5.7 The driven and damped system. Population imbalance vs ξ; $kd = 24$, $\Lambda = 0.1$, $\zeta = 1 \times 10^{-4}$, $\varepsilon = 1 \times 10^{-3}$, $\Omega = 0.01$ (a) $Z(0) = 0.12$, $\phi(0) = 0.7$, $\phi(0) = -0.3$ (b)= $Z(0) = -0.15$, $\phi(0) = -0.7$, $\phi(0) = -0.1$. 67

5.8 The driven and damped system. Population imbalance vs ξ; $kd = 19$, $\Lambda = 0.1$, $\varepsilon = 1 \times 10^{-3}$, $\Omega = 0.01$ (a) $\zeta = 2.2 \times 10^{-4}$, $Z(0) = 0.12$, $\phi(0) = 0.4$, $\phi(0) = 0$ (b)Figure with zoom in. 68

5.9 The driven and damped system. Population imbalance vs ξ; $kd = 19$, $\Lambda = 0.1$, $\varepsilon = 1 \times 10^{-3}$, $\Omega = 0.01$ (a)$\zeta = 1.1 \times 10^{-4}$ $Z(0) = -0.15$, $\phi(0) = -0.3$, $\phi(0) = 0.8$ (b)Figure with zoom in. 69

5.10 The driven and damped system. Population imbalance vs ξ; $kd = 24$, $\Lambda = 0.1$, $\varepsilon = 1 \times 10^{-3}$, $\Omega = 0.01$ (a) $\zeta = 1.1 \times 10^{-4}$, $Z(0) = 0.12$, $\phi(0) = -0.3$, $\phi(0) = 0.7$ (b)Figure with zoom in. 69

5.11 The driven and damped system. Population imbalance vs ξ; $kd = 24$, $\Lambda = 0.1$, $\varepsilon = 1 \times 10^{-3}$, $\Omega = 0.01$ (a) $\zeta = 1.1 \times 10^{-4}$, $Z(0) = -0.15$, $\phi(0) = -0.7$, $\phi(0) = -0.1$ (b)Figure with zoom in. 70

5.12 The driven and damped system. Population imbalance vs ξ; $kd = 24$, $\Lambda = 0.1$, $\varepsilon = 1 \times 10^{-3}$, $\Omega = 0.01$, $Z(0) = 0.12$, $\phi(0) = 0.7$, $\phi(0) = -0.3$ (a) $\zeta = 1 \times 10^{-4}$ (b)$\zeta = 1.1 \times 10^{-4}$. 71

5.13 The driven and damped system. Population imbalance vs ξ; $kd = 24$, $\Lambda = 0.1$, $\varepsilon = 1 \times 10^{-3}$, $\Omega = 0.01$, $Z(0) = -0.15$, $\phi(0) = -0.7$, $\phi(0) = -0.1$ (a) $\zeta = 1 \times 10^{-4}$ (b)$\zeta = 1.1 \times 10^{-4}$. 71

NOMENCLATURE

SP	Surface Plasmon
JJ	Josephson Junction
SJJ	Superconducting Josephson Junction
BJJ	Bosonic Josephson Junction
BEC	Bose-Einstein Condensation
DWSP-JJ	Dielectric Waveguide Surface Plasmon Josephson Junction
NLSE	Nonlinear Schrödinger Equation

Chapter 1

INTRODUCTION

The storage and control of electrons can be provided by electronic circuits, however the performance of electronic circuits is rather limited when digital information needs to be sent from one point to another. This problem is solved by introducing photonics that offers an effective solution by implementing optical communication systems based on optical fibers and photonic circuits. Unfortunately, the micrometer-scale bulky components of photonics have limited the integration of these components into electronic chips, which are measured in nanometers. The size-compatibility problem can be solved with surface plasmon based circuits, which merge electronics and photonics at the nanoscale. Surface plasmons [1, 2] are electromagnetic waves that propagate along the surface of a conductor. The interaction of light with matter in nanostructured metallic structures has led to a new branch of photonics called plasmonics [3, 4, 5]. Plasmonics has developed into one of the most active research fields of modern optics that have been observed at nanoscales in the structures incorporating metals, with many promising applications such as in lasing, sensing, and waveguiding at subwavelength scales [4]. In addition to this, waveguiding in plasmonic nanoguides and circuits represent a great interest for telecommunication, computing, as well as information processing [6, 7]. The advantage of the surface plasmon-based devices is that the properties of surface plasmons in particular, their interaction with light can be manipulated by changing the structure of metal's surface. This manipulation offers the potential for developing new types of photonic devices. Several applications have been proposed and already realized [8].

The surface plasmons can be excited via the evanescent wave generated by the total

internal reflection [9, 10, 11] or via a periodic structure producing evanescent modes. In order to extend the capabilities of nanoscale metal structures, the coupling between the surface plasmons [12, 13, 14] and optical solitons [15, 16] can be considered. Due to the nonlinear nature of soliton, the coupling of such a system is nonlinear by itself. The motivation of this work derives from the need in manipulating the excitation and propagation of surface-plasmons optically, which may be utilized in optic or plasmonic applications. This system can be modeled as fiber(soliton), and metal(surface plasmon) coupled system. The photonic transfer can be provided between metal and fiber. In the surface plasmon-soliton case, the lateral tail of the soliton field can act as a source to excite the surface-plasmons which leads to manipulate the system by the soliton amplitude. The control parameter is no longer the wavelength but the soliton amplitude. It is formulated by an effective coupling parameter between the soliton and the surface-plasmon. Hence, the dynamics between the soliton and surface-plasmon under this coupling has to be investigated. The outline of this thesis is as follows :

In Chapter 1, we briefly explain the surface plasmon and optical soliton. Next, the Josephson junction systems described by introducing the superconducting Josephson junctions and bosonic josephson junctions.

In Chapter 2, we describe the main theoretical model of the coupled surface plasmon-optical soliton system. The dielectric waveguide surface plasmon Josephson junction (DWSP-JJ) is introduced. Subsequently, the application of the Josephson junction (JJ) formulation to DWSP-JJ model and the comparison with the Bosonic Josephson Junction (BJJ) model are presented. A general description of the linear stability analysis and its application to DWSP-JJ model are shown.

In Chapter 3, the dynamical analysis of the weakly coupled DWSP-JJ model is presented and the phase portrait of the model is shown for different values of the control parameters. We also show the phase portrait comparison of BJJ and DWSP-JJ models. Subsequently, propagation properties along the interface and the experimental feasibility are discussed.

In Chapter 4, we focus on DWSP-JJ coupled system in the presence of damping. The equation of motion for the system is introduced and dynamical analysis is given. Additionally, the corresponding spatial propagation properties are presented.
In Chapter 5, shapiro effect is briefly explained and shapiro resonances both in BJJ and DWSP-JJ systems are presented. In the final Chapter 6, a brief summary concludes the work, describing all important findings and giving an outlook for possible routes to follow with this work.

1.1 Surface Plasmons

Metals provide the best evidence of plasmons since they have a high density of electrons free to move. The electrons oscillate in response to the applied electromagnetic field and their motion is damped due to the collisions with collision frequency α=$1/\tau$ where τ is the relaxation time of free electron gas. The response of the metal to the applied field is different at low and high frequencies. For considering the low incoming waves frequencies(ω), metals retain their metallic character($\omega < \omega_p$) whereas for higher frequencies, light penetrates into the metal($\omega > \omega_p$) and transparency regime occurs. After the external field is removed, electrons repel each other and positive ions attract them so they oscillate back and forth with the bulk plasma frequency (ω_p) until the energy is dissipated [4]. Plasma frequency is given by

$$\omega_p{}^2 = \frac{ne^2}{m_e\epsilon_0} \tag{1.1}$$

where n is the electron density, m_e is the effective mass of electrons and ϵ_0 is the permittivity of the free space.
The electric charges on a metal boundary can form a metallic fluctuations which are called surface plasmon oscillations [17]. The existence of surface plasmons is demonstrated [19] in electron energy loss experiments. Surface plasmons can be considered as non-propagating collective vibrations of the electron plasma near the metal surface. They represent electromagnetic surface waves which have maximum intensity on the surface and exponentially decaying fields perpendicular to it [20]. The exponential

dependence of the field can be seen in Fig 1.1. The frequency of the surface plasmon is [21]:

$$\omega_{sp} = \frac{\omega_p}{\sqrt{1+\epsilon_2}} \tag{1.2}$$

where ω_p is the bulk plasmon frequency, and ϵ_2 is the permittivity of the dielectric interface.

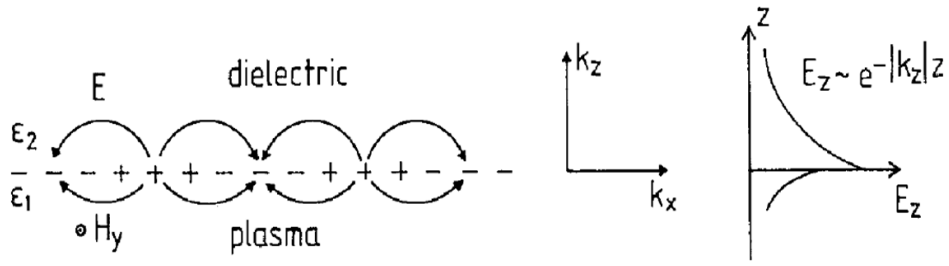

Figure 1.1: Schematic presentation of charges and electromagnetic field of surface plasmon propagating in x direction. On the right side electric field E_z is shown. H_y shows the magnetic field in y direction of this p-polarized wave [17, 18].

1.2 Optical Solitons

In 1834, a solitary wave was discovered by John Scott Russell who observed solitary wave in the Edinburgh-Glasgow canal [22]. The solitary waves were later called solitons by Zabusky and Kruskal [23]. The solitons can propagate without distortion and maintain their shape not to be affected by dispersion as shown in Fig. 1.2.

The optical pulses are subject to dispersion as they travel in a medium with linear dielectric response. When light propagates through a material, the electric field induces a polarization to electrons of the material and slows below $3 \times 10^8 m/s$ in vacuum. In a medium both chromatic dispersion and self-phase modulation separately affect the propagation of an optical pulse. Therefore, in order to generate a soliton, the effects of chromatic dispersion and self-phase modulation should cancel each other. If the light source were completely monochromatic, then it would generate photons at single frequency which travel with the same speed. The photons in an optical pulse

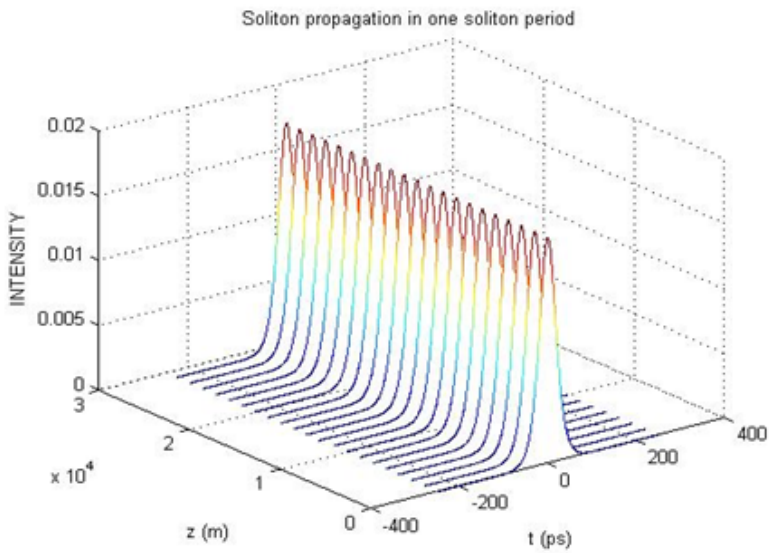

Figure 1.2: Schematic presentation of soliton propagation [24].

propagates with different speeds. This cause the pulse broadening which is known as the chromatic dispersion. It is one of the major problems. The other difficulty is the self-phase modulation. The nonlinear refractive index of the material depends on both frequency of light and its intensity Eq. 1.4. The self-modulation generates a phase shift in optical pulse according to the intensity dependent nonlinear refractive index. The phase shift changes the distance between the peaks and the oscillation frequency along the horizontal axis. The degree of polarization increases nonlinearly with light intensity as can be seen in Eq. 1.3. The nonlinear refractive index of a material increases with increasing light intensity. The induced polarization in a nonlinear dielectric takes the form :

$$P = \epsilon_0 \chi E + \epsilon_0 \chi^{(2)} |E|^2 + \epsilon_0 \chi^{(3)} |E|^2 E... \tag{1.3}$$

where χ is the dielectric susceptibility. The $\chi^{(2)}$ is zero for an optical fiber and higher order terms are neglected. Hence, only the first and third terms are considered. The electric field of a plane wave is $E = E_0 cos(wt - kz)$ with the corresponding intensity $I = \frac{c\epsilon n_0 E_0^2}{2}$. The Kerr [25] effect changes nonlinear refractive index to balance diffraction effects with nonlinear medium [26]. The general relation between polarization

and refractive index is $P = \epsilon_0(n^2 - 1)E$. The nonlinear refractive index yields:

$$n = n_0 + n_2|E|^2 \tag{1.4}$$

where

$$n_2 = \frac{3\chi^{(3)}}{4c\epsilon_0 n_0^2} \tag{1.5}$$

The basic equation governing the propagation of pulses in optical fiber is the time dependent Nonlinear Schrödinger Equation (NLSE). It describes the evolution of optical wave packets in nonlinear dielectric medium. The pulse in a nonlinear dispersive medium is expressed with NLSE :

$$-i\frac{\partial u}{\partial z} = \frac{1}{2}\frac{\partial u^2}{\partial t^2} + |u|^2 u \tag{1.6}$$

The solution of the NLSE is given by:

$$u(z,t) = sech(t)e^{iz/2} \tag{1.7}$$

The Zakharov and Shabat used the Inverse Scattering Method to solve the NLSE [27]. In nonlinear optics, solitons are classified as temporal and spatial solitons [28, 29, 30, 31, 32]. Temporal solitons represent optical pulses with conserving their form in time. Spatial solitons present self-guided beams that remain confined in the transverse directions and represents an exact balance between diffraction and nonlinearly induced self-lensing or self-focusing effects, as shown schematically in Fig. 1.3. The NLSE is valid both pulse (temporal) and beam (spatial) propagation in a medium with Kerr nonlinearity. If the properties of the pulse are just right, the instantaneous effects of self-phase modulation and dispersion cancel each other out completely, and the pulse remains unchirped and retains its initial width along the entire length of the fiber. In other words, the soliton is formed. The formation of solitons are satisfied with the following relations :

$$P = \frac{-\beta_2}{\gamma T_0} \tag{1.8}$$

where P is the peak power of the pulse, β_2 is the dispersion parameter, γ is the nonlinear coefficient, (T_0) is the half-width of the pulse at its maximum intensity

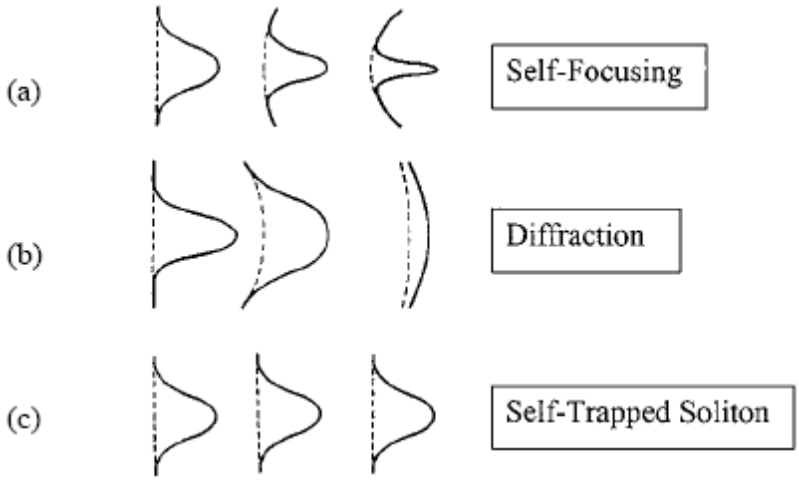

Figure 1.3: Schematic showing the spatial beam profiles (a) beam self-focusing (b) normal beam diffraction (c) soliton propagation [33].

point.

$$\beta_2 = \frac{\lambda_3 \delta^2 n}{2\pi^2 c^2 \delta\lambda^2} \tag{1.9}$$

$$\gamma = \frac{2\pi n^2}{\lambda A_{eff}} \tag{1.10}$$

where λ is wavelength of the pulse, c is the speed of light in vacuum, n is the nonlinear refractive index, n_2 is the nonlinear index coefficient, and A_{eff} is the effective core area of the fiber.

1.3 Josephson Junction Systems in Physics

In this Section, we explain the Josephson effect in different physical systems. The definition of the system is given and types of the Josephson junction are explained in Section 1.3.1. Next, we introduce the Bosonic Josepson Junction (BJJ) and show its analogy with the SJJ in Section 1.3.2. The dynamical equations both SJJ and BJJ models are described.

1.3.1 Superconducting Josephson Junction (SJJ)

In 1962 Brian Josephson [34] suggested a simple model of two Superconductors separated by a thin insulator, no voltage between them, would have a current pass from one metal to another. This is classically not possible, but in quantum mechanics tunneling process can make it possible. Brian Josephson was the first to predict the tunneling of superconducting Cooper pairs [35, 36, 37] and recieved the Nobel Prize in 1973. The simple model of two superconductors seperated by a thin insulator is known as the Josephson Junction [38, 39, 40]. The insulating barrier between superconductor [41] layers is very thin that electrons can cross through the barrier. If the thickness of the barrier is less than 30 A^0, single electrons can tunnel between the two superconductors. If the thickness of the barrier is decreased to 10 A^0 or below a weak link of two superconductors is generated. The wavefunction of the superconductors begin to overlap. This overlap corresponds to Cooper pair transport from one superconductor to another, which is called Josephson tunnelling. In contrast to single electrons, Cooper pairs have integer spin and they obey the Bose-Einstein Statistics. The electrons in one superconductor can be described with one wave function. The phase difference between the wave functions in the two superconductors induces a supercurrent described by :

$$I = I_c sin\phi \tag{1.11}$$

This phenomenon is known as the DC Josephson effect (Fig. 1.4). This supercurrent flows without any voltage drop over the junction. When a bias voltage is applied over the junction, the phase angles will increase over time. This phenomenon is known as the AC Josephson effect(Fig. 1.5).

$$\dot{\phi} = \frac{2eV}{\hbar} \tag{1.12}$$

The Superconductors on the left S_L and on the right S_R are separated by the insulating barrier in Fig 1.6. The Josephson Junction equations [42, 43, 44, 45, 46] can be derived in the following approach :

The Schrödinger Equation for each macroscopic wave equations are:

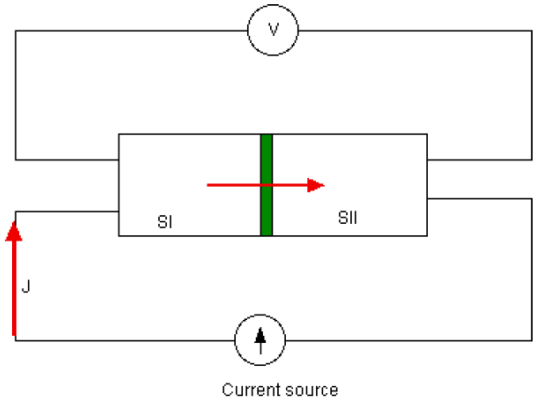

Figure 1.4: Schematic diagram for DC Josephson effect. Two superconductors SI and SII are separated by a very thin insulator (denoted by green). DC Josephson supercurrent (up to a maximum value Ic) flows without dissipation through the insulating layer [47].

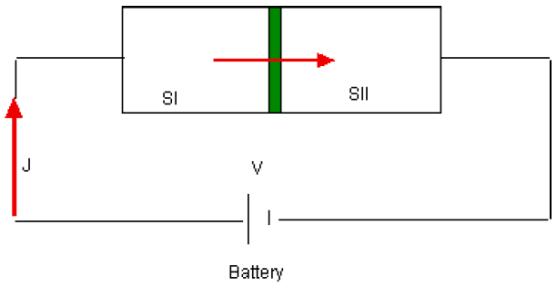

Figure 1.5: Schematic diagram for AC Josephson effect with applied finite DC voltage across both the ends [47].

$$i\hbar\frac{\partial\Psi_L}{\partial t} = E_L\Psi_L \tag{1.13}$$

$$i\hbar\frac{\partial\Psi_R}{\partial t} = E_R\Psi_R \tag{1.14}$$

The system is coupled via additional tunneling energy term in the presence of weak coupling yields;

$$i\hbar\frac{\partial\Psi_L}{\partial t} = E_L\Psi_L + K\Psi_R \tag{1.15}$$

$$i\hbar\frac{\partial\Psi_R}{\partial t} = E_R\Psi_R + K\Psi_L \tag{1.16}$$

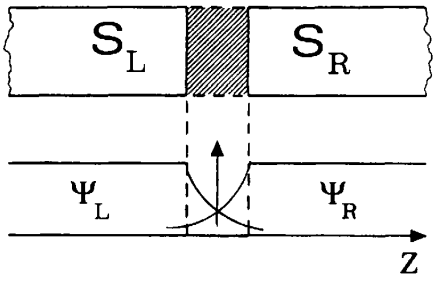

Figure 1.6: Schematic of a josephson Junction. S_L and S_R are left and right superconductors. Ψ_L and Ψ_R are left and right pair wavefunctions [38].

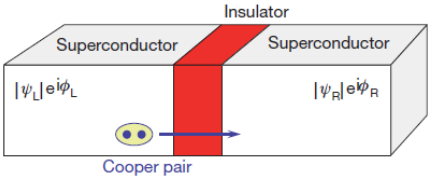

Figure 1.7: Schematic view of SJJ model with cooper pair representation [38].

K is the coupling amplitude of the two state which give a measure of the coupling interaction between the two superconductors and it depends on the specific Junction structure. E_L and E_R are ground state energies of the two superconductors and given by $E_L = 2\mu_L$ and $E_R = 2\mu_R$ where μ_L and μ_R are the two chemical potentials. Assume that there is a DC potential difference across the junction so chemical potentials are shifted by amount eV $(E_L - E_R = 2eV)$ yields:

$$i\hbar\frac{\partial\Psi_L}{\partial t} = eVE_L\Psi_L + K\Psi_R \tag{1.17}$$

$$i\hbar\frac{\partial\Psi_R}{\partial t} = -eVE_R\Psi_R + K\Psi_L \tag{1.18}$$

The two macroscopic wave functions are described in the following ansatz :

$$\Psi_L = \sqrt{\rho_L}e^{i\phi_L} \tag{1.19}$$

$$\Psi_R = \sqrt{\rho_R}e^{i\phi_R} \tag{1.20}$$

where ρ_L and ρ_R are the Cooper pair densities $(\rho = |\psi|^2)$ and ϕ_L and ϕ_R are the phases of the cooper pair wavefunctions. The substitution of wavefunctions Eq. 1.19,

Eq. 1.20 into equations Eq. 1.15, Eq. 1.16 yields new equations.Then separate the real and imaginary terms in each equation we get($\phi = \phi_L - \phi_R$);

$$\frac{\partial \rho_L}{\partial t} = \frac{2}{\hbar} K \sqrt{\rho_L \rho_R} \sin\phi \tag{1.21}$$

$$\frac{\partial \rho_R}{\partial t} = -\frac{2}{\hbar} K \sqrt{\rho_L \rho_R} \sin\phi \tag{1.22}$$

$$\frac{\partial \phi_L}{\partial t} = \frac{K}{\hbar} \sqrt{\frac{\rho_L}{\rho_R}} \cos\phi + \frac{eV}{\hbar} \tag{1.23}$$

$$\frac{\partial \phi_R}{\partial t} = -\frac{K}{\hbar} \sqrt{\frac{\rho_L}{\rho_R}} \cos\phi - \frac{eV}{\hbar} \tag{1.24}$$

The pair current density $J \equiv \frac{\partial \phi_L}{\partial t} = -\frac{\partial \phi_R}{\partial t}$:

$$J = \frac{2K}{\hbar} \sqrt{\rho_L \rho_R} \tag{1.25}$$

assume that $\rho_L = \rho_R = \rho_0$ $J = \frac{2K}{\hbar} \rho_0 sin\phi$ with $J_0 = \frac{2K}{\hbar} \rho_0$ is the Cooper pair tunnelling current density. The two Josephson equations are derived;

$$J = J_0 sin\phi \tag{1.26}$$

$$\dot{\Phi} = \frac{2eV}{\hbar} \tag{1.27}$$

In the absence of an external voltage $V = 0$ the phase difference is constant. In this case a finite current can flow through the barrier without any voltage drop across the junction. This phenomenon called DC Josephson effect [48]. If a constant voltage is applied to the Josephson Junction Eq. 1.27 and by considering this equation it can easily be shown that relative phase is no longer constant.

$$\phi(t) = \phi_0 + \frac{2eV}{\hbar} t \tag{1.28}$$

It is linearly increasing in time and $J = J_0 \sin(\phi_0 + \omega_{ac} t)$ alternative current with frequency $\omega_{ac} = \frac{2eV}{\hbar}$. This is called AC Josephson Effect.

1.3.2 Bosonic Josephson Junction(BJJ)

Bose-Einstein condensation (BEC) was predicted by Satyendra Nath Bose [49] in 1924. The possibility of condensing massive Bosonic particles (which have integer spin) into a single quantum mechanical state was predicted by Albert Einstein [50, 51] based on a work of S.N. Bose on the statistical properties of photons in 1924. A dilute gas of weakly interacting bosons confined in an external potential and cooled by several techniques to temperature near absolute zero ($0K$) is known as the Bose-Einstein condensation [52, 53]. Below a certain critical temperature bosonic particles occupy the same lowest energy quantum mechanical state, they are coherent source of matter waves. This phenomena was first experimentally realized in 1995 [54, 55] and for their achievements Cornell, Wieman and Ketterle receieved 2001 Nobel Prize in physics. The Bose-Einstein condensates at low temperature can be used to realize a bosonic

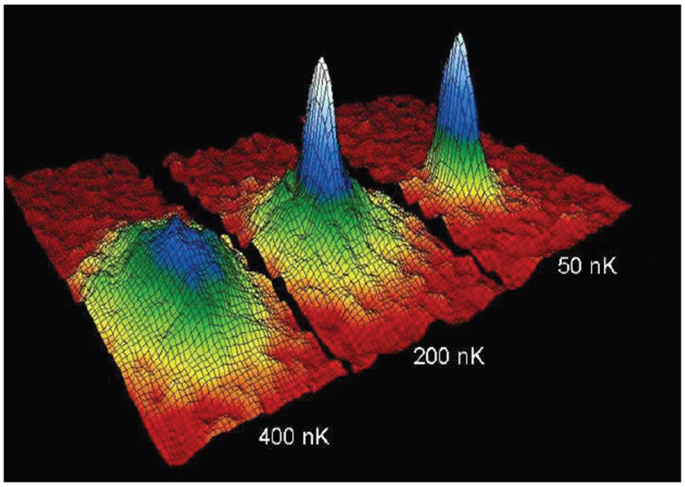

Figure 1.8: Bose Einstein condensation of Rb^{87} atoms, as observed by absorption of laser light [54, 55]. At $T \simeq 200nK$ a macroscopic fraction of atoms condenses, corresponding to the central peak [57].

Josephson Junction. BEC is loaded into an optical lattice potential generated by a standing wave laser field. the macroscopic quantum coherence of BEC results in coherent quantum tunnelling of atoms between two modes(two BEC's) Fig. 1.9. This

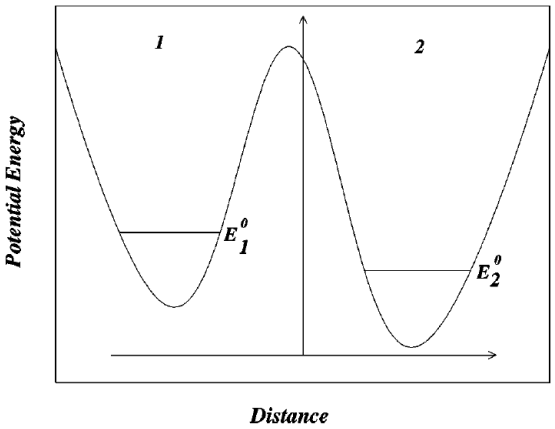

Figure 1.9: Asymmetric double-well trap for BEC N_1, N_2 the number of particles and the E_1^0 and E_2^0 the on site energies of trap 1 and 2 respectively [38, 59]

.

case is similar to the coherent tunneling of Cooper pairs in a Josephson Junction [56]. The dynamical equations of the Bosonic Josephson Junction are described with non-linear two mode approximation. The weakly coupled two mode system is via the variational wave function as:

$$\psi(r,t) = \psi_1(t)\phi_1(r) + \psi_2(t)\phi_2(r) \tag{1.29}$$

with

$$\psi_{1,2}(r,t) = \sqrt{N_{1,2}(t)}e^{i\phi_{1,2}} \tag{1.30}$$

where $N_{1,2}$ is the number of atoms and ϕ_1,ϕ_2 the phase in the corresponding well, and a constant total number of atoms $N_1 + N_2 = |\psi_1|^2 + |\psi_1|^2 \equiv N_T$. The nonlinear two-mode dynamical equations [58, 59, 60] are:

$$i\hbar\frac{\partial\psi_1}{\partial t} = ({E_1}^0 + U_1N_1)\psi_1 - K\psi_2 \tag{1.31}$$

$$i\hbar\frac{\partial\psi_2}{\partial t} = ({E_2}^0 + U_2N_2)\psi_2 - K\psi_1 \tag{1.32}$$

In Eq. 1.31, and Eq. 1.32 the $E_{1,2}$ are the onsite energies for well 1,2. K is the coupling constant, $U_{1,2}$ are the inter atomic interaction energies.

$$E_{1,2}^0 = \int [\frac{\hbar^2}{2m}|\nabla\phi_{1,2}|^2 + |\phi_{1,2}|^2 V_{ext}]dr \tag{1.33}$$

$$K = -\int [\frac{\hbar^2}{2m}\nabla\phi_1\nabla\phi_2 + \phi_1 V_{ext}\phi_2]dr \tag{1.34}$$

$$U_{1,2} = g\int |\phi_{1,2}|^2 dr \tag{1.35}$$

The relative phase difference :

$$\phi(t) = \phi_2(t) - \phi_1(t) \tag{1.36}$$

The fractional imbalance :

$$Z(t) = \frac{N_1(t) - N_2(t)}{N_T(t)} \tag{1.37}$$

In order to obtain to coupled differential equations for the two dynamic variables z, ϕ, substitude Eq. 1.30 into Eq. 1.31 and Eq. 1.32. Then separate the real and imaginary terms in each equation :

$$\dot{N_1} = -\frac{2K}{\hbar}\sqrt{N_1 N_2}sin\phi \tag{1.38}$$

$$\dot{\phi_1} = -\frac{K}{\hbar}\sqrt{\frac{N_2}{N_1}}cos\phi - \frac{1}{\hbar}(E_1 + U_1 N_1) \tag{1.39}$$

$$\dot{N_2} = \frac{2K}{\hbar}\sqrt{N_1 N_2}sin\phi \tag{1.40}$$

$$\dot{\phi_2} = -\frac{K}{\hbar}\sqrt{\frac{N_1}{N_2}}\cos\phi - \frac{1}{\hbar}(E_2 + U_2 N_2) \tag{1.41}$$

The derivative of z and ϕ with equations 1.38, 1.39, 1.40, 1.41 yields ;

$$\dot{z}(t) = -\frac{2K}{\hbar}\sqrt{N_1 N_2}sin\phi \tag{1.42}$$

$$\dot{\phi}(t) = -\frac{K}{\hbar}\frac{N_1 - N_2}{\sqrt{N_1 N_2}}\cos\phi + \frac{1}{\hbar}(E_1 + E_2) + \frac{U_1 N_1 - U_2 N_2}{\hbar} \tag{1.43}$$

By introducing dimensionless parameters ΔE, Λ. The dynamic equations of the system is obtained: Here, the time is expressed in unit of $\frac{\hbar}{2K}$

$$\Delta E = \frac{E_1^0 - E_2^0}{2K} + \frac{U_1 - U_2}{4K}N_T \tag{1.44}$$

$$\Lambda = \frac{U_1 + U_2}{4K}N_T \tag{1.45}$$

$$\dot{z}(t) = -\sqrt{1 - z^2}\sin\phi(t) \tag{1.46}$$

$$\dot{\phi}(t) = \Delta E + \Lambda z + \frac{z}{\sqrt{1 - z^2}}\cos\phi(t) \tag{1.47}$$

Nonrigid pendulum [61] with a length $l = \sqrt{1-z^2}$ is defined. If we identify the relative phase ϕ with the displacement angle and fractional imbalance z with the angular momentum of the pendulum interwell trap tunneling current is given by;

$$I = \frac{\dot{z}(t)N_T}{2} = I_0\sqrt{1-z^2}\sin\phi \tag{1.48}$$

where $I_0 = -\frac{KN_T}{\hbar}$ corresponds to maximum allowed Cooper pair current in the superconducting analog.

These equations are very similar to SJJ equations but due to the interatomic interactions nonlinearity appears and this leads to a new affects which are not observed in SJJ. The SJJ is generally discussed in terms of rigid pendulum analogy, while BJJ in a double well trap is explained in term of non-rigid pendulum analogy, with a length dependent on the angular momentum. In SJJ model, superconducting grains are two equal-volume so population imbalance is zero. The dynamical variable is the voltage ($\dot{\phi} = \frac{2eV}{\hbar}$). In isolated double-well BJJ model the nonrigid pendulum dynamics are associated with superfluid density oscillations of an isolated system. An isolated SJJ allows coherent Cooper pair oscillation in small plasma frequency limit.

Chapter 2

THEORETICAL MODEL AND DYNAMICAL STABILITY ANALYSIS

In this Chapter, we describe the main theoretical model of the coupled surface plasmon-optical soliton system. The dielectric waveguide surface plasmon Josephson junction (DWSP-JJ) is introduced in Section 2.1. The application of the Josephson junction (JJ) formulation to DWSP-JJ model and the comparison with the Bosonic Josephson Junction (BJJ) model are presented in Section 2.2. We also describe an analogous mechanical system known as the nonrigid pendulum. A general description of the linear stability analysis and its application to DWSP-JJ model are presented in the last section.

2.1 Description of the Model

The resonant interaction between the co-propagating surface-plasmons on a metal surface and solitons in a nonlinear dielectric medium has been investigated recently [15]. It is shown that the interaction depends on the soliton amplitude which may provide way of manipulating the surface plasmon propagation. Figure 2.1 shows a schematic view of the dielectric metal interface. The nonlinearity in the dielectric is assumed to be confined at a distance d from the metal interface such that the surface-plasmon propagation retains linearity, and the weak coupling between the soliton and surface plasmon fields can be treated perturbatively. The translational invariance is assumed to be in the z direction and the propagation direction is chosen in the y direction. It should be noted that the present model does not include the dissipation effects, which will be considered in Chapter 4.

The total wave function is represented via the ansatz [15]:

$$\Psi(x,y) = \Psi_p(x,y) + \Psi_s(x,y) \tag{2.1}$$

$$\Psi_p(x,y) = c_p(y)\psi_p(x) \tag{2.2}$$

$$\Psi_s(x,y) = c_s(y)\psi_s(x) \tag{2.3}$$

where $\psi_p(x)=e^{-\kappa_p x}$ with $\kappa_p = \sqrt{k_p^2 - k^2}$ and $\psi_s(x,|c_s|)=sech[\kappa_s(x-d)]$ with $\kappa_s = k\sqrt{\gamma/2}|c_s|$. c_p and c_s are the amplitudes of plasmon and soliton respectively. The incoming light wavevector is denoted by k and the surface-plasmon wave vector is denoted by k_p. γ is the nonlinearity parameter of the dielectric medium. The to-

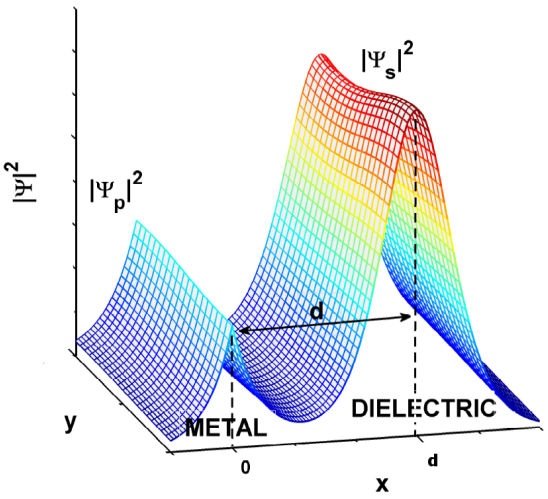

Figure 2.1: Schematic view of the coupled surface plasmon optical soliton model, d is the distance between the metal and the soliton propagation axis. The lateral field profiles $|\Psi_p^2|$ and $|\Psi_s^2|$ are plotted.

tal electric field of the co-propagating surface-plasmon (SP) optical soliton in the dielectric ($x \geq 0$) [16] is written in the form,

$$E(x,y) = c_p(y)e^{-\kappa_p x} + \frac{c_s(y)}{\cosh\left[\kappa_s(x-d)\right]}, \tag{2.4}$$

The Maxwell wave equations for the c_p, c_s are as follows:

$$\ddot{c_p} + \beta_p^2 c_p = q(|c_s|)c_s, \tag{2.5}$$

$$\ddot{c_s} + \beta_s^2 c_s = q(|c_s|)c_p. \tag{2.6}$$

Here, $\beta_p = k_p/k$ and $\beta_s = 1 + \gamma|c_s|^2/4$ are the propagation constants of plasmon and soliton respectively. The coupling parameter, q, depends on the lateral tail of the soliton field which acts as a source to excite surface plasmons. Therefore, up to a numerical factor, the coupling parameter q should be proportional to the soliton field at the metal surface $\Psi_s(x = 0) = c_s\psi_s(x = 0)$ [15]. For weak coupling this estimation yields :

$$q(|c_s|) \approx \psi_s(x = 0) = 2/(e^{k\sqrt{\gamma/2}|c_s|d} + e^{-k\sqrt{\gamma/2}|c_s|d}) \tag{2.7}$$

$$q(|c_s|) \approx \psi_s(x = 0) \approx 2(e^{-k\sqrt{\gamma/2}|c_s|d}) \tag{2.8}$$

In order to linearize the coupled wave functions, we substitute $c_{p,s} = \mathscr{C}_{p,s}e^{i\xi}$ and apply slowly varying amplitude approximation. Here, $\xi = ky$ is the dimensionless propagation coordinate. The following set of equations is obtained (see Appendix A for details):

$$i\dot{\mathscr{C}}_p = \nu_p\mathscr{C}_p - \frac{q(|\mathscr{C}_s|)}{2}\mathscr{C}_p, \tag{2.9}$$

$$i\dot{\mathscr{C}}_s = -\frac{q(|\mathscr{C}_s|))}{2}\mathscr{C}_p + \nu_s(|\mathscr{C}_s|)\mathscr{C}_s. \tag{2.10}$$

In (2.10), $\nu_p \equiv \beta_p - 1 \ll 1$, $\nu_s \equiv \beta_s - 1 \ll 1$ are the small deviations of the dimensionless propagation constants of the SP and the soliton, respectively.

2.2 Bosonic Josephson Junction Formulation

In this section, the connection between the SP-soliton optical system and the Bosonic Josephson Junction (BJJ) is presented. Using linearized coupled equations, we introduce new dynamical variables Z and ϕ. Z is the fractional population imbalance ($Z \equiv (|C_s|^2 - |C_p|^2)/N$), where N is the total population for the isolated system. In the absence of population dissipation, we set $N = (|C_s|^2 + |C_p|^2) \equiv 1$. ϕ is the relative phase difference: $\phi \equiv \phi_s - \phi_p$. The BJJ formulation is obtained by substituting $\mathscr{C}_{p,s} = C_{p,s}e^{i\phi_{s,p}}$ into Eq. 2.10 (see Appendix B for details) and separating imaginary and real parts respectively.

$$\dot{C_p} = \frac{q}{2}C_s \sin\phi \tag{2.11}$$

$$\dot{C}_s = -\frac{q}{2} C_p \sin\phi \tag{2.12}$$

$$\dot{\phi}_p = -\frac{q}{2}\frac{C_s}{C_p}\cos\phi + \nu_p, \tag{2.13}$$

$$\dot{\phi}_s = -\frac{q}{2}\frac{C_p}{C_s}\cos\phi + \nu_s, \tag{2.14}$$

$$\dot{Z} = -q(Z)\sqrt{1-Z^2}\sin\phi, \tag{2.15}$$

$$\dot{\phi} = \Lambda Z + \Delta E + \frac{q(Z)Z}{\sqrt{1-Z^2}}\cos\phi. \tag{2.16}$$

where,

$$q(Z) = e^{-kd\sqrt{2\Lambda(1+Z)}}. \tag{2.17}$$

The parameters of this formulation are defined as $\Lambda \equiv \frac{\gamma N}{8}$, $\Delta E = \Lambda - \nu_p$, with $\eta = \frac{\gamma N}{4}$. Here, Λ becomes the nonlinearity parameter whereas ΔE parametrizes the asymmetry between the soliton and surface plasmon states occupied by the photons.

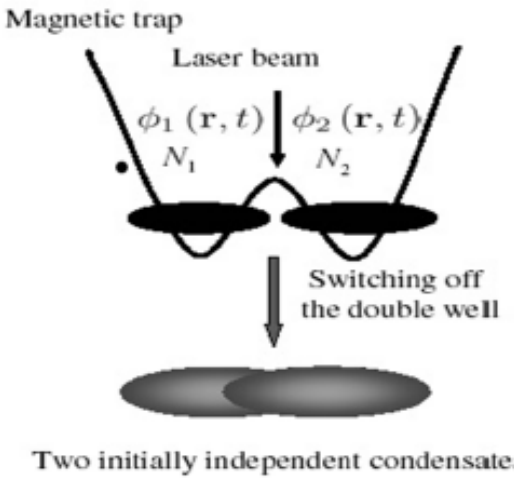

Figure 2.2: Schematic view of the Bose-Einstein condensate in a double-well trap(Figure taken from Ref. [62]).

2.2.1 Bosonic Josephson Junction

An immediate comparison reveals the similarities and differences with the bosonic Josephson junction (BJJ) in a double well trap [63, **?**]. In the BJJ model, in order to describe the tunnelling and the dynamical oscillations of the two weakly linked condensate atoms, a variational wave function is introduced :

$$\Psi(r,t) = c_1(t)\Phi_1(r) + c_2(t)\Phi_2(r) \tag{2.18}$$

This ansatz includes uniform amplitudes $c_{1,2} = C_{1,2}e^{i\phi_{1,2}(t)}$, where $N_{1,2}$ are the number of particles and $\phi_{1,2}$, phases in the trap 1 and 2, respectively. The total number of condensate atoms is defined as $N_T = (|C_1|^2 + |C_2|^2)$. $\Phi_{1,2}$ describe the spatial profile of the condensate in each trap. The fractional population imbalance is defined as $Z(t) \equiv (|C_1|^2 - |C_2|^2)/N_T$, and the relative phase $\phi(t) \equiv \phi_2(t) - \phi_1(t)$. The amplitudes of the condensate atoms in the traps are $|C_{1,2}(t)|$ and phases $\phi_{1,2}(t)$ obey the nonlinear two-mode dynamical equations [59, 63, 64]:

$$\begin{aligned} i\hbar\dot{C}_1 &= (E_1^0 + U_1N_1)C_1 - KC_2 \\ i\hbar\dot{C}_2 &= (E_2^0 + U_2N_2)C_2 - KC_1, \end{aligned} \tag{2.19}$$

where $E_{1,2}^0$ are the zero point energies for wells $1, 2$ and $U_{1,2}^0$ are proportional to the mean-field energy. By separating imaginary and real parts we get :

$$\dot{C}_1 = -\frac{K}{\hbar}C_2 \sin\phi, \tag{2.20}$$

$$\dot{C}_2 = \frac{K}{\hbar}C_1 \sin\phi, \tag{2.21}$$

$$\dot{\phi}_1 = \frac{K}{\hbar}\frac{C_2}{C_1}\cos\phi - \frac{E_1^0}{\hbar} - \frac{U_1N_1}{\hbar}, \tag{2.22}$$

$$\dot{\phi}_2 = \frac{K}{\hbar}\frac{C_1}{C_2}\cos\phi - \frac{E_2^0}{\hbar} - \frac{U_2N_2}{\hbar}. \tag{2.23}$$

Using $\dot{\phi} = \dot{\phi}_2 - \dot{\phi}_1$ and $\dot{Z} = \frac{2}{N_T}[\dot{C}_2C_1 - \dot{C}_1C_2]$, the equations of motion of BJJ model are as follows:

$$\dot{Z}(t) = -\sqrt{1 - Z(t)^2}\sin\phi(t), \tag{2.24}$$

$$\dot{\phi}(t) = \Lambda Z + \Delta E + \frac{Z(t)}{\sqrt{1 - Z(t)^2}}\cos\phi(t), \tag{2.25}$$

$$\Lambda = N_T \frac{U_1 + U_2}{4K}, \tag{2.26}$$

$$\Delta E = \frac{E_1^0 - E_2^0}{2K} + N_T \frac{U_1 - U_2}{4K}. \tag{2.27}$$

Here, Λ describes the interatomic interactions and ΔE is the difference between the zero-point energies of the trapping wells. Both Λ and ΔE are dimensionless parameters scaled by the coupling matrix element K [59]. In the DWSP-JJ model, the coupling parameter depends on the fractional population imbalance Z whereas the coupling parameter of the BJJ model is constant. We observe that the DWSP-JJ equations would reduce to that of the BJJ model for a constant coupling parameter $q(Z) \equiv 1$, provided that the other parameters are scaled accordingly.

2.2.2 Non-Rigid Pendulum Analogy

The dynamics of the BJJ system has a mechanical pendulum analogy as well. Figure 2.3 (b) shows this pendulum schematically, where the length of the pendulum is not constant (i.e. nonrigid). The coupled differential equations Eq. 2.28 and Eq. 2.29 describe the deviation angle $\phi(t)$ and the angular momentum $Z(t)$ for this pendulum [63, **?**]. Here, ϕ and Z are the canonically conjugate variables. The length l of the pendulum is proportional to $l{=}\sqrt{1 - Z^2}$ where l decreases with increasing angular momentum, Z. The equations of motion are :

$$\dot{Z}(t) = -\sqrt{1 - Z(t)^2}\sin\phi(t), \tag{2.28}$$

$$\dot{\phi}(t) = \Lambda Z + \Delta E + \frac{Z(t)}{\sqrt{1 - Z(t)^2}}\cos\phi(t). \tag{2.29}$$

In Figure 2.3(a), typical phase space portrait of the nonrigid pendulum is plotted where the fixed points and several trajectories are shown [57]. For the red and black colored phase space trajectories, the pendulum moves like a simple pendulum with harmonic (red) and anharmonic (black) oscillations. Two running trajectories are also shown for which the pendulum makes full rotations (green line and blue line). At $\phi = \pm\pi$, there exists three fixed points. Two of them are stable near $Z = \pm 1$, (violet circles) and one is unstable at $Z = 0$ (purple line). The length of the pendulum takes

maximum value at $Z = 0$ and minimum value near $Z = \pm 1$. The corresponding motion for closed trajectories are harmonic oscillations around fixed point and for running trajectory is full rotation of the pendulum.

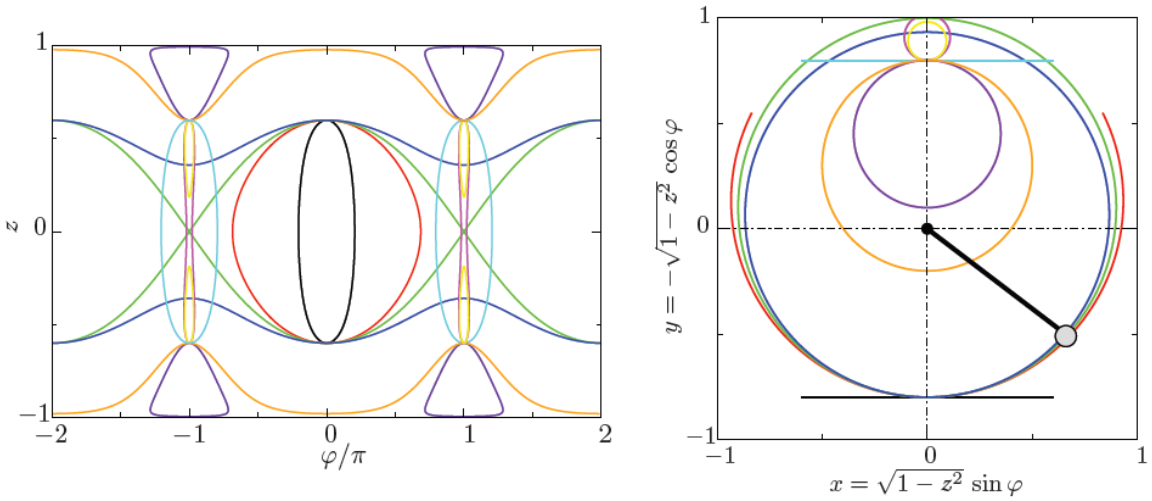

Figure 2.3: Phase space trajectories (*Left panel*) with corresponding real space motions of the non-rigid pendulum (*Right panel*) different trajectories are expressed with different colors Note the fixed points for $\phi = 0$ and $\phi = \pi$ modes around which closed (red, black, violet) and open (green, blue, orange) trajectories are shown(Figure taken from Ref. [57]).

2.3 Linear Stability Analysis of a Dynamical System

The Linear Stability Analysis investigates the behavior of a dynamical system under small deviations from its equilibrium states [65]. Here we consider a 2D system described by the first order ODE as, $\dot{x}=\frac{dx}{dt}$, $\dot{y}=\frac{dy}{dt}$, where

$$\dot{x} = f(x, y) \tag{2.30}$$

$$\dot{y} = g(x, y), \tag{2.31}$$

Denoting the steady states (equilibrium points), $\bar{x}$,$\bar{y}$ $f(\bar{x}, \bar{y})$ and $g(\bar{x}, \bar{y})$ are equal to zero. In order to see whether the steady state is stable or unstable, we introduce a small perturbation from the equilibrium point by letting

$$x = \bar{x} + u \tag{2.32}$$

$$y = \bar{y} + v \tag{2.33}$$

where u and v are the small perturbations. Substituting 2.32 and 2.33 into 2.30 and 2.31 yields :

$$\dot{u} = \dot{x} = f(x, y) = f(\bar{x} + u, \bar{y} + v) \tag{2.34}$$

$$\dot{v} = \dot{y} = g(x, y) = g(\bar{x} + u, \bar{y} + v) \tag{2.35}$$

Since u, v are small f and g can be expanded in Taylor series as follows:

$$\dot{u} = f(\bar{x}, \bar{y}) + \frac{\partial f}{\partial x}(\bar{x}, \bar{y})u + \frac{\partial f}{\partial y}(\bar{x}, \bar{y})v + ... \tag{2.36}$$

$$\dot{v} = g(\bar{x}, \bar{y}) + \frac{\partial g}{\partial x}(\bar{x}, \bar{y})u + \frac{\partial g}{\partial y}(\bar{x}, \bar{y})v + ... \tag{2.37}$$

$$\dot{u} = \frac{\partial f}{\partial x}(\bar{x}, \bar{y})u + \frac{\partial f}{\partial y}(\bar{x}, \bar{y})v + ... \tag{2.38}$$

$$\dot{v} = \frac{\partial g}{\partial x}(\bar{x}, \bar{y})u + \frac{\partial g}{\partial y}(\bar{x}, \bar{y})v + ... \tag{2.39}$$

Since u and v are the linear terms only the first terms in Taylor series are retained. The equation for system $\dot{u}$ and $\dot{v}$ can be written in matrix form:

$$\begin{bmatrix} \dot{u} \\ \dot{v} \end{bmatrix} = \begin{bmatrix} \frac{\partial f}{\partial x}(\bar{x}, \bar{y}) & \frac{\partial f}{\partial y}(\bar{x}, \bar{y}) \\ \frac{\partial g}{\partial x}(\bar{x}, \bar{y}) & \frac{\partial g}{\partial y}(\bar{x}, \bar{y}) \end{bmatrix} \begin{bmatrix} u \\ v \end{bmatrix} \tag{2.40}$$

The Jacobian Matrix of the system is given by:

$$J = \begin{bmatrix} \frac{\partial f}{\partial x}(\bar{x},\bar{y}) & \frac{\partial f}{\partial y}(\bar{x},\bar{y}) \\ \frac{\partial g}{\partial x}(\bar{x},\bar{y}) & \frac{\partial g}{\partial y}(\bar{x},\bar{y}) \end{bmatrix} \tag{2.41}$$

By diagonalizing the Jacobian

$$\begin{bmatrix} \dot{u'} \\ \dot{v'} \end{bmatrix} = \begin{bmatrix} \lambda_1 & 0 \\ 0 & \lambda_2 \end{bmatrix} \begin{bmatrix} u' \\ v' \end{bmatrix} \tag{2.42}$$

We find $u'(t)$ and $v'(t)$ as $u'(t)$=$u_0 e^{\lambda_1 t}$ and $v'(t)$=$v_0 e^{\lambda_2 t}$. To summarize, determination of the linear stability of the fixed point $\bar{x}$,$\bar{y}$ is as follows [66]:

1. The eigenvalues of the Jacobian matrix are calculated at the fixed point.

2. The following cases are determined.

Case1: $\lambda_1 \neq \lambda_2$ real, negative sign: fixed point is stable. $\lambda_1 \neq \lambda_2$ real, positive sign: fixed point is unstable.

Case2: λ_1 and λ_2 real, either equal or unequal magnitude with opposite sign: fixed point is unstable.

Case3: λ_1=λ_2=λ real, negative: fixed point is stable. λ_1=λ_2=λ real, positive: fixed point is unstable.

Case4: λ_1=$a + ib$, λ_2=$a - ib$ with a and b are real, $a < 0$: fixed point is stable.
λ_1=$a + ib$, λ_2=$a - ib$ with a and b are real, $a > 0$: fixed point is unstable.

Case5: λ_1=ib, λ_2=$-ib$ purely imaginary conjugate pair: fixed point is stable.

The dynamical equations of the system are as follows:

$$f = \dot{Z} = -q(Z)\sqrt{1 - Z^2}\sin\phi, \tag{2.43}$$

$$g = \dot{\phi} = \Lambda Z + \Delta E + \frac{q(Z)Z}{\sqrt{1 - Z^2}}\cos\phi. \tag{2.44}$$

The system at fixed points ϕ^*=0 and ϕ^*=π as follows:

$$J = \begin{bmatrix} \frac{\partial \dot{Z}}{\partial Z} & \frac{\partial \dot{Z}}{\partial \phi} \\ \frac{\partial \dot{\phi}}{\partial Z} & \frac{\partial \dot{\phi}}{\partial \phi} \end{bmatrix} \tag{2.45}$$

$$J_{11} = \frac{\partial \dot{Z}}{\partial Z} = 0 \tag{2.46}$$

$$J_{12} = \frac{\partial \dot{Z}}{\partial \phi} = \pm q(Z)\sqrt{1 - Z^2} \tag{2.47}$$

$$J_{21} = \frac{\partial \dot{\phi}}{\partial Z} = \Lambda \pm (-\frac{qZ}{\sqrt{1+Z}} kd \sqrt{\frac{2\Lambda}{1-Z^2}} + \frac{q}{1-Z^2}) \tag{2.48}$$

$$J_{22} = \frac{\partial \dot{\phi}}{\partial \phi} = 0 \tag{2.49}$$

The eigenvalues of the Jacobian matrix are then :

$$\lambda_1 = \sqrt{-\Lambda q(Z)\sqrt{1-Z^2} + q^2(Z\frac{kd}{2}\sqrt{\frac{2\Lambda}{1+Z}} - \frac{1}{1-Z^2})} \tag{2.50}$$

$$\lambda_2 = \sqrt{\Lambda q(Z)\sqrt{1-Z^2} + q^2(Z\frac{kd}{2}\sqrt{\frac{2\Lambda}{1+Z}} - \frac{1}{1-Z^2})} \tag{2.51}$$

In order to see how the Z coordinate of the fixed points are distributed for values of the control parameters Λ and ν_p, we plot them for (a)$\phi = 0$ and (b) $\phi = \pi$ respectively. We investigate the range of control parameters for $0.05 < \Lambda < 0.175$ and $0.1 < \nu_p < 0.35$. In Fig. 2.4(a), Fig. 2.5(a), Fig. 2.6(a), the system exhibits single fixed point for various values of Λ, and ν_p at $\phi = 0$ (b) whereas at $\phi = \pi$ for certain Λ, and ν_p the number of fixed points increases up to three. In Fig. 2.4(b) and Fig. 2.5(b) the system exhibits three fixed points, however, in Fig. 2.6(b) up to two fixed points do exist.

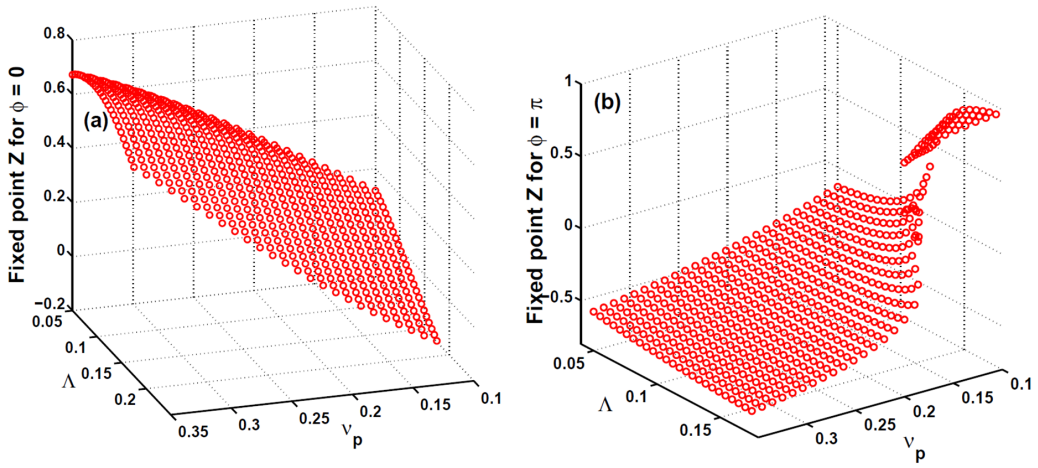

Figure 2.4: The fixed points Z with $kd = 3$, $0.05 < \Lambda < 0.175$ and $0.1 < \nu_p < 0.35$ (a) $\phi = 0$, (b)$\phi = \pi$.

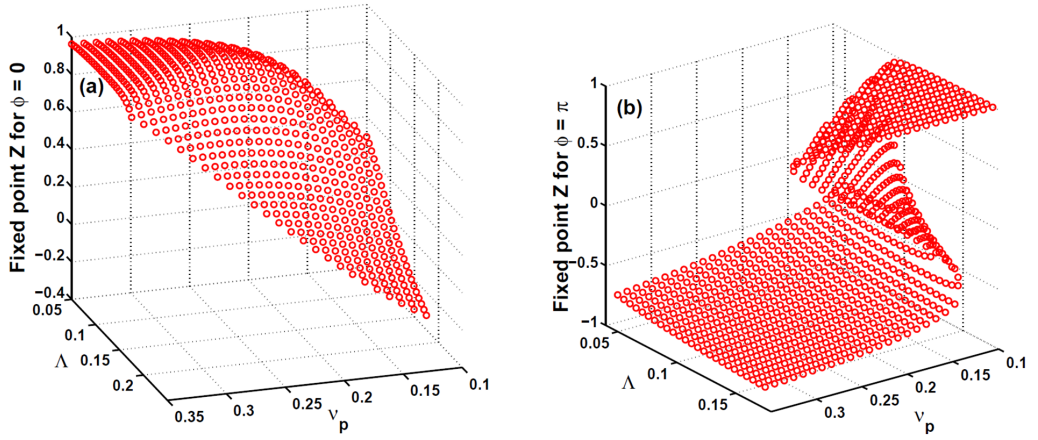

Figure 2.5: The fixed points Z with $kd = 6$, $0.05 < \Lambda < 0.175$ and $0.1 < \nu_p < 0.35$ (a) $\phi = 0$, (b)$\phi = \pi$.

In Fig. 2.7, Fig. 2.8, and Fig. 2.9 the eigenvalues of the system are investigated at $\phi = 0$ mode for $kd = 3$, $kd = 6$, $kd = 12$, respectively.

Case 1: $kd = 3$, $\phi = 0$, $\lambda = a + ib$. In Fig. 2.7(a) the real part of the eigenvalues are all zero ($a = 0$) and (b) the imaginary parts are nonzero($b \neq 0$). All eigenvalues are purely imaginary for $0.05 < \Lambda < 0.175$ with $0.1 < \nu_p < 0.35$. This type of fixed point

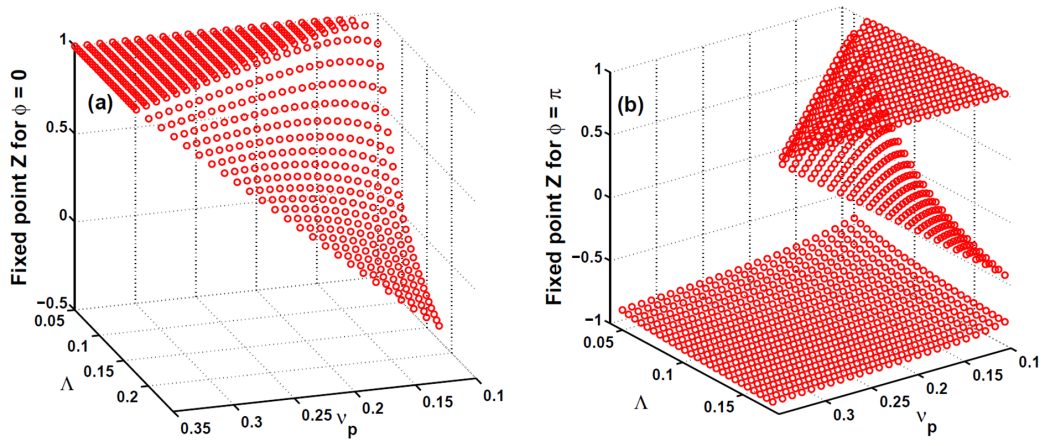

Figure 2.6: The fixed points Z with $kd = 12$, $0.05 < \Lambda < 0.175$ and $0.1 < \nu_p < 0.35$ (a) $\phi = 0$, (b)$\phi = \pi$.

is stable. System exhibits closed trajectories in the phase plane.

Case 2: $kd = 6$, $\phi = 0$, $\lambda = a + ib$. In Fig. 2.8(a) $a = 0$ and (b) $b > 0$. Eigenvalues are imaginary and positive for $0.05 < \Lambda < 0.175$ with $0.1 < \nu_p < 0.35$. No real eigenvalues exist. Fixed point is stable. The overall magnitude of eigenvalues decrease with increasing kd (Eq. 2.50).

Case 3: $kd = 12$, $\phi = 0$, $\lambda = a + ib$. In Fig. 2.9(a) $a = 0$ and (b) $b > 0$. Eigenvalues are purely imaginary. Therefore, the fixed point is stable. For large kd eigenvalues decrease. For some Λ and ν_p values $a = 0$ and $b = 0$ as a result $\lambda = 0$ so no fixed point exists.

Next, we investigate eigenvalues are investigated for $kd = 3$, $kd = 6$, $kd = 12$ at $\phi = \pi$ mode. Up to three, fixed points can occur. The following cases are presented for the first, second, and third fixed points, respectively.

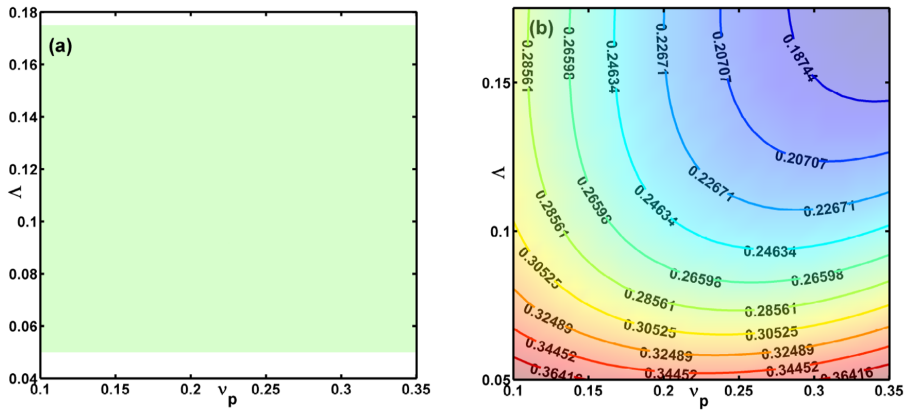

Figure 2.7: The Jacobian eigenvalue of the fixed point for $\phi = 0$ with $kd = 3$, $0.05 < \Lambda < 0.175$ and $0.1 < \nu_p < 0.35$ (a) real part is zero (b) imaginary part stable single fixed point

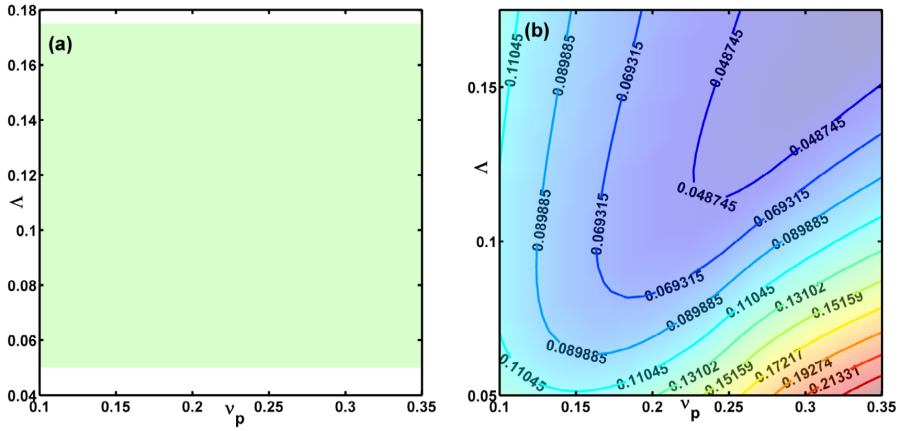

Figure 2.8: The Jacobian eigenvalue of the fixed point for $\phi = 0$ with $kd = 6$, $0.05 < \Lambda < 0.175$ and $0.1 < \nu_p < 0.35$ (a) real part is zero (b) imaginary part stable single fixed point

$kd = 3$

(i) First fixed point; $kd = 3$, $\phi = \pi$, $\lambda = a + ib$. In Fig. 2.10(a) real part of eigenvalues are zero ($a = 0$) and (b) imaginary part of eigenvalues are positive ($b > 0$). All eigenvalues are imaginary for $0.05 < \Lambda < 0.175$ with $0.1 < \nu_p < 0.35$. Fixed point is stable. System exhibits closed trajectories in phase plane. For constant Λ with

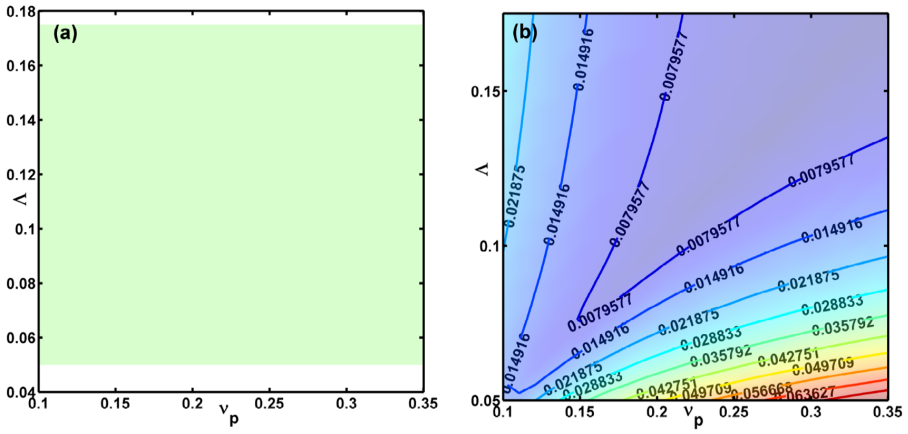

Figure 2.9: The Jacobian eigenvalue of the fixed point for $\phi = 0$ with $kd = 12$, $0.05 < \Lambda < 0.175$ and $0.1 < \nu_p < 0.35$ (a) real part is zero (b) imaginary part stable single fixed point

increasing ν_p, eigenvalues increase. For constant ν_p with increasing Λ, eigenvalues are almost constant.

(ii) However, as shown in Fig. 2.10 there is an unstable fixed point. This fixed point exist for $0.165 < \nu_p < 0.185$ with $0.161 < \Lambda < 0.171$ (imaginary part is zero real part is nonzero). System exhibits open trajectories in the phase plane. For constant Λ with increasing ν_p, eigenvalues increase up to critical ν_p, then decrease and go to zero. For constant ν_p with increasing Λ, eigenvalues are almost constant.

(iii) Third fixed point; $kd = 3$, $\phi = \pi$, $\lambda = e + if$. In Fig. 2.10(e) real part of eigenvalues is zero ($e = 0$). In Fig. 2.10(f) up to $\Lambda = 0.15$ no imaginary eigenvalues exist. However, for $0.165 < \Lambda < 0.169$ with $0.165 < \nu_p < 0.175$, system exhibit imaginary eigenvalues ($f > 0$). For this range fixed point is stable. System shows closed trajectories in phase plane. For constant Λ with increasing ν_p, eigenvalues increase up to critical ν_p, then then decrease and go to zero. For constant ν_p with increasing Λ, eigenvalues are almost constant.

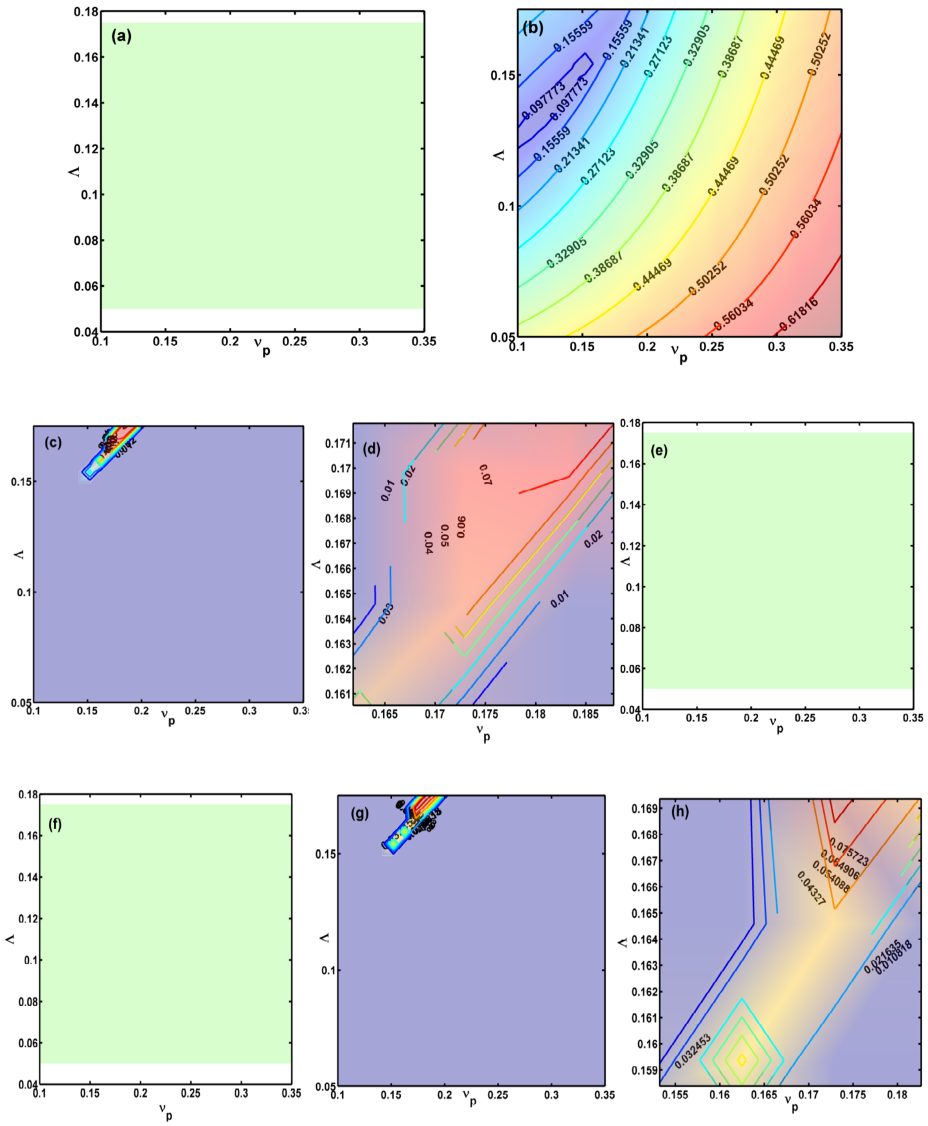

Figure 2.10: The Jacobian eigenvalue of the first fixed point for $\phi = \pi$ with $kd = 3$, $0.05 < \Lambda < 0.175$ and $0.1 < \nu_p < 0.35$ (a) real part of eigenvalues are zero (b) imaginary part stable fixed point. For the second fixed point (c) real part is not zero at certain Λ and ν_p, so unstable fixed point (d) eigenvalues are zoomed for $0.161 < \Lambda < 0.171$ and $0.165 < \nu_p < 0.185$ (e) imaginary part of eigenvalues are zero. For the third fixed point (f) real part is zero (g) $\Lambda > 0.15$ and $0.1 < \nu_p < 0.35$ imaginary stable fixed point (h) eigenvalues are zoomed for $0.165 < \Lambda < 0.169$ with $0.165 < \nu_p < 0.175$.

$kd = 6$

(i) First fixed point; $kd = 6$, $\phi = \pi$, $\lambda = a + ib$. In (Fig. 2.11)(a) real part of eigenvalues are zero ($a = 0$) and (b) imaginary part of eigenvalues are positive ($b > 0$).

All eigenvalues are imaginary for $0.05 < \Lambda < 0.175$ with $0.1 < \nu_p < 0.35$. Fixed point is stable. System exhibits closed trajectories in phase plane. For constant Λ with increasing ν_p, eigenvalues increase. For constant ν_p with increasing Λ, eigenvalues are almost constant.

(ii) Second fixed point; $kd = 6$, $\phi = \pi$, $\lambda = c + id$. In (Fig. 2.11) (c) Up to $\Lambda = 0.085$, real part of eigenvalues are zero ($c = 0$) and (d) imaginary part of the eigenvalues are zero ($d = 0$) so no fixed point exist. However, for certain values of Λ and ν_p there is an unstable fixed point (imaginary part is zero only positive real eigenvalue exist) shown in Fig. 2.11(c). System exhibits unbounded open trajectories in phase plane. For constant Λ with increasing ν_p, eigenvalues increase up to critical ν_p, then then decrease and go to zero. For constant ν_p with increasing Λ, eigenvalues are almost constant.

(iii) Third fixed point; $kd = 6$, $\phi = \pi$, $\lambda = e + if$. In Fig. 2.11(e) real part of eigenvalues are zero ($e = 0$), (f) up to $\Lambda = 0.085$ no imaginary eigenvalues so no fixed point exist. However, for certain values of Λ and ν_p there is a stable fixed point (eigenvalues are purely imaginary). System exhibits closed trajectories in phase plane. For constant Λ with increasing ν_p, eigenvalues increase up to critical ν_p, then decrease and go to zero. For constant ν_p with increasing Λ, eigenvalues are almost constant.

$kd = 12$

(i) First fixed point; $kd = 12$, $\phi = \pi$, $\lambda = a + ib$. In (Fig. 2.12) (a) real part of eigenvalues are zero ($a = 0$) and (b) imaginary part of eigenvalues are nonzero ($b \neq 0$). All eigenvalues are imaginary and positive between $0.05 < \Lambda < 0.175$ with $0.1 < \nu_p < 0.35$. Fixed point is stable. System exhibits closed trajectories in phase plane. For constant Λ with increasing ν_p, eigenvalues increase. For constant ν_p with increasing Λ, eigenvalues are almost constant.

(ii) Second fixed point; $kd = 12$, $\phi = \pi$, $\lambda = c + id$. In (Fig. 2.12) (c) Up to $\Lambda = 0.085$, real part of eigenvalues are zero ($c = 0$) and (d) imaginary part of the eigenvalues for $0.05 < \Lambda < 0.175$ with $0.1 < \nu_p < 0.35$ are zero ($d = 0$) so no fixed point exist. However, (Fig. 2.12) (c) for certain values of Λ and ν_p, there is an unstable fixed point (imaginary part of the eigenvalue is zero only positive real eigenvalue is exist). System exhibits open trajectories in phase plane. For constant Λ with increasing ν_p, eigenvalues increase up to critical ν_p, then decrease and go to zero. For constant ν_p with increasing Λ, eigenvalues are almost constant.

(iii) Third fixed point; $kd = 12$, $\phi = \pi$, $\lambda = e + if$. In Fig. 2.12(e) real part of eigenvalues is zero ($e = 0$), (f) up to $\Lambda = 0.075$ no imaginary eigenvalues so no fixed point exist. However, Fig. 2.12(e) for certain values of Λ and ν_p there is a stable fixed point (eigenvalues are purely imaginary). System exhibits closed trajectories in phase plane. For constant Λ with increasing ν_p, eigenvalues increase up to critical ν_p, then decrease and go to zero. For constant ν_p with increasing Λ, eigenvalues are almost constant.

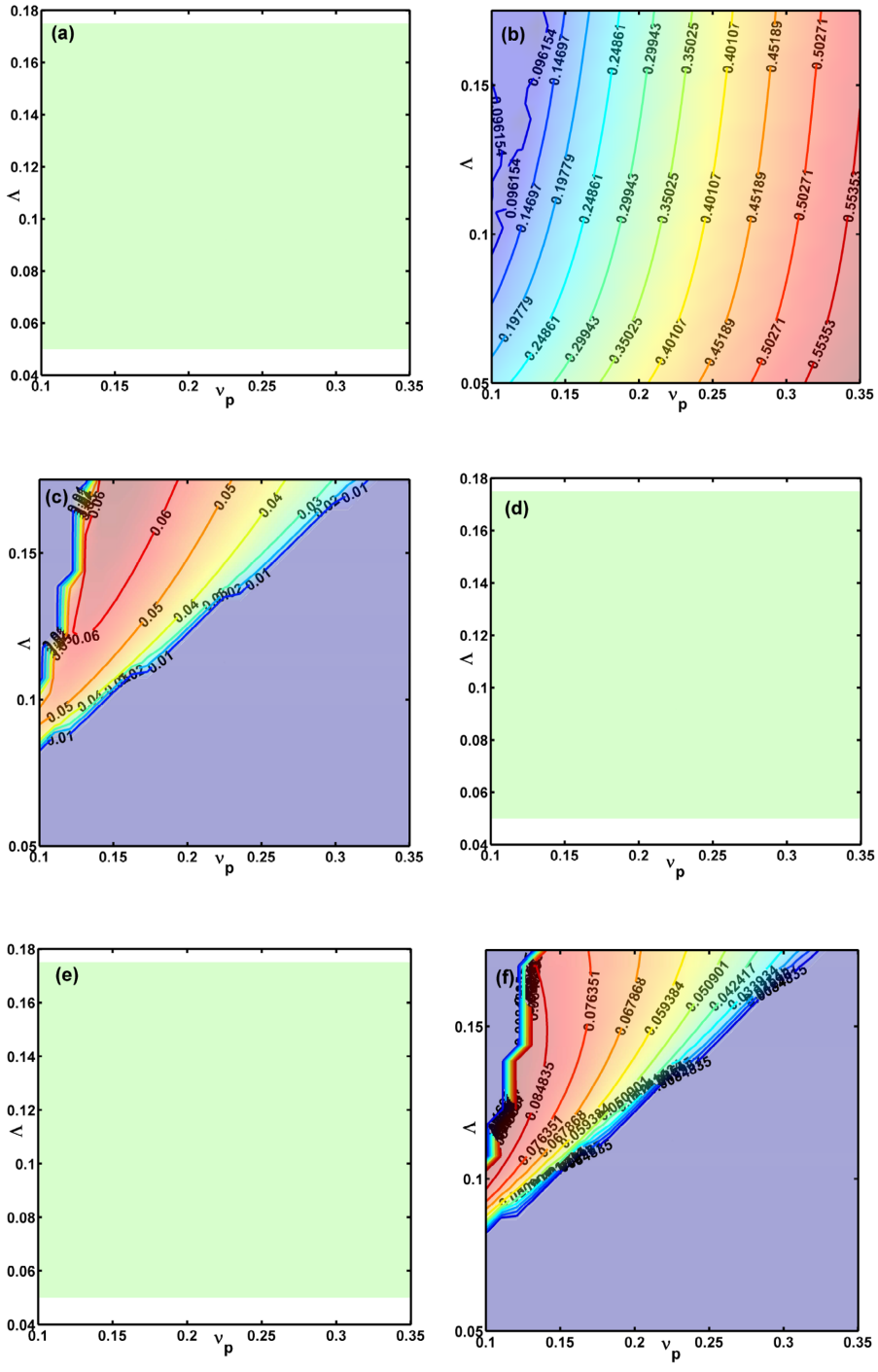

Figure 2.11: The Jacobian eigenvalue of the first fixed point for $\phi = \pi$ with $kd = 6$, $0.05 < \Lambda < 0.175$ and $0.1 < \nu_p < 0.35$ (a) real part is zero (b) imaginary part stable fixed point. For the second fixed point(c) real part unstable fixed point for certain Λ, and ν_p (d) imaginary part is zero. For the third fixed point (e) real part is zero (f) for certain Λ, and ν_p imaginary part stable fixed point.

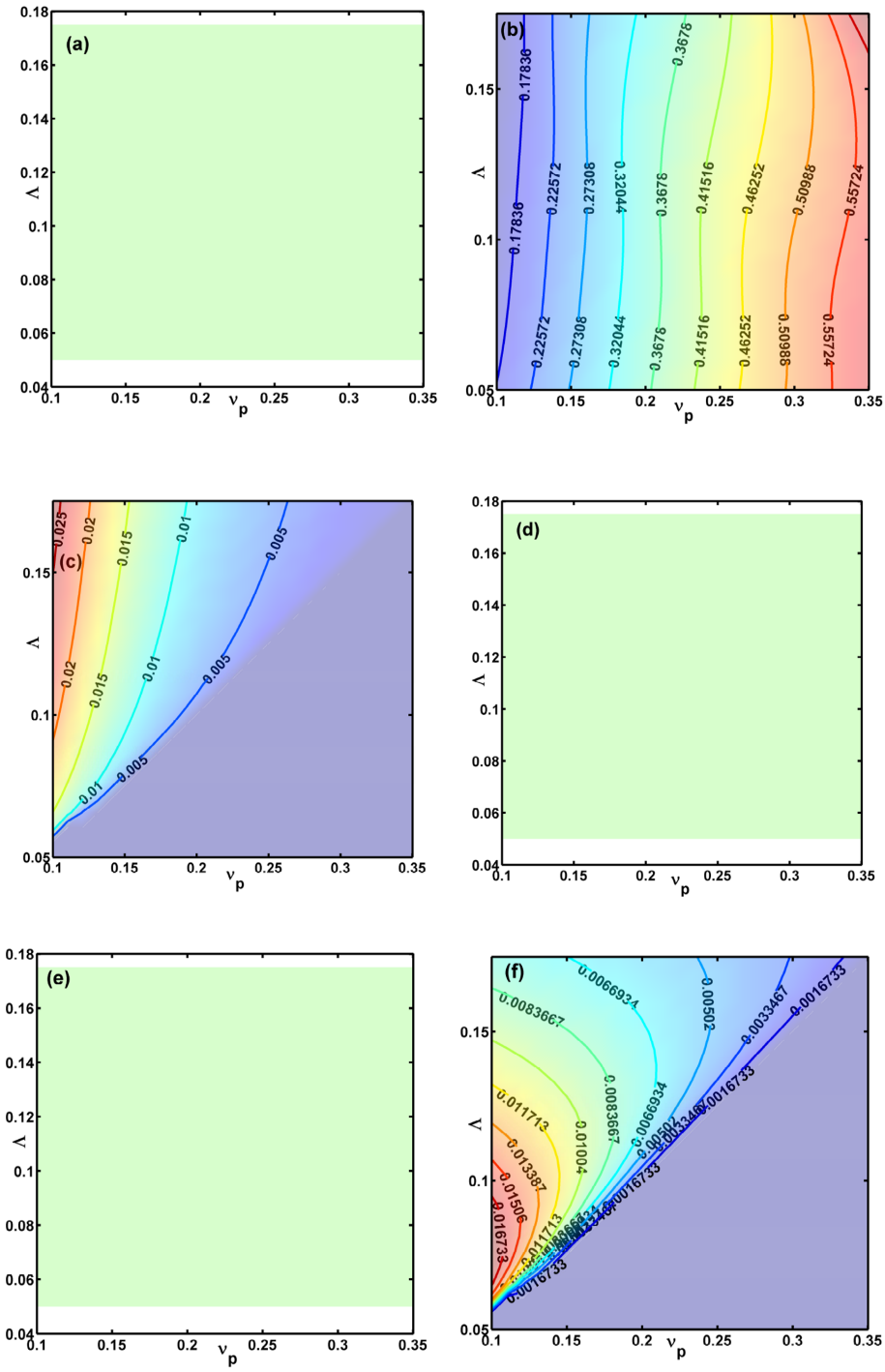

Figure 2.12: The Jacobian eigenvalue of the first fixed point for $\phi = \pi$ with $kd = 12$, $0.05 < \Lambda < 0.175$ and $0.1 < \nu_p < 0.35$ (a) real part zero (b) imaginary part stable fixed point. For the second fixed point For the second fixed point(c) real part unstable fixed point for certain Λ, and ν_p (d) imaginary part is zero. For the third fixed point (e) real part is zero (f) for certain Λ and ν_p imaginary part stable fixed point.

Chapter 3

DYNAMICAL ANALYSIS : RESULTS

In this Chapter, the dynamical analysis of the weakly coupled DWSP-JJ model is presented. The fixed points for the coupled system are shown in Section 3.1. In the next section, the phase portrait of the model is shown for different values of the control parameters. In Section 3.3, the phase portrait comparison of the BJJ and the DWSP-JJ model are presented. The propagation properties along the interface are discussed in Section 3.4 and finally the experimental feasibility is discussed in Section 3.5.

3.1 Fixed Point Analysis

The dynamical analysis of the DWSP-JJ, is done first by determining the stationary points. For the ϕ coordinate the critical points are trivial ϕ=0 and ϕ=$\pm\pi$. We then find the Z coordinate of the critical points from:

$$f(Z)|_{Z^*} = \Lambda Z^* + \Delta E + \frac{q(Z^*)Z^*}{\sqrt{1-(Z^*)^2}}\cos(\phi^*) = 0. \tag{3.1}$$

The resonant coupling $q_{res} = \exp[-kd\sqrt{2\nu_p}]$ occurs around $\nu_p = 0.2$, $\Lambda = 0.1$ [15]. Therefore, the relevant range for control parameters of the DWSP-JJ is chosen as $0.1 < \nu_p < 0.35$ and $0.05 < \Lambda < 0.175$. The zero-phase modes describe the transfer of energy between the soliton and surface-plasmon states with the zero time-average ($< \phi >$=0) value of the phase. In figures 3.1(a-c) f(Z) is plotted for different values of ΔE with $v_p = 0.15$ and $kd = 3, 6, 12$. For $\Delta E = 0$, the fixed point is at $Z = 0$, which can also be deduced by inspecting Eq. (3.1). This is analogous to the *symmetric double well* of the BJJ model. The case of $\Delta E < (>)0$, the fixed point occurs at nonzero fractional population imbalance $Z > (<)0$. In the example of the $\Delta E < 0$

the population imbalance shifts to soliton dominant mode whereas the $\Delta E > 0$, it shifts to plasmon dominant mode.

The other mode is the π-phase mode, where the time-average value of phase is $< \phi >= \pi$. In this case multiple critical points occur as shown in Fig. (3.2). The location of the fixed points depend also on the scaled distance kd.

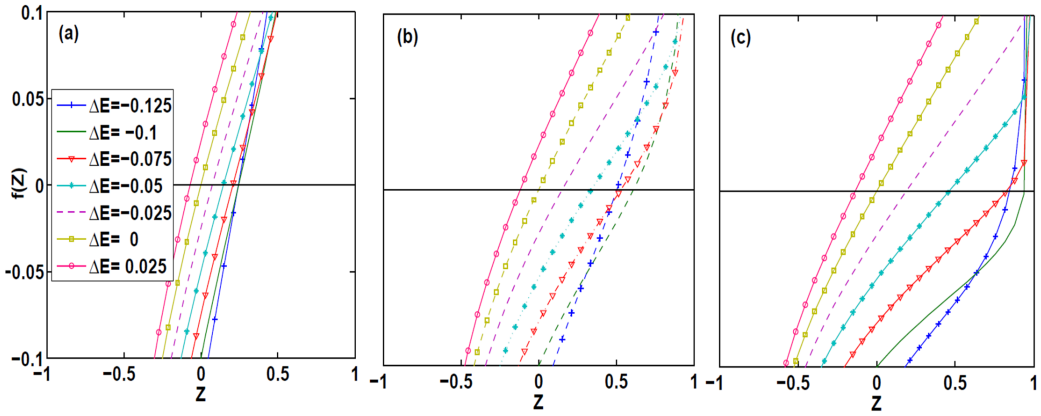

Figure 3.1: $f(Z)$ (Eq. 3.1) for zero-phase modes plotted at $\nu_p = 0.15$ with various values of ΔE and (a) $kd = 3$ (b) $kd = 6$ and (c) $kd = 12$ The critical points are the roots of $f(Z) = 0$.

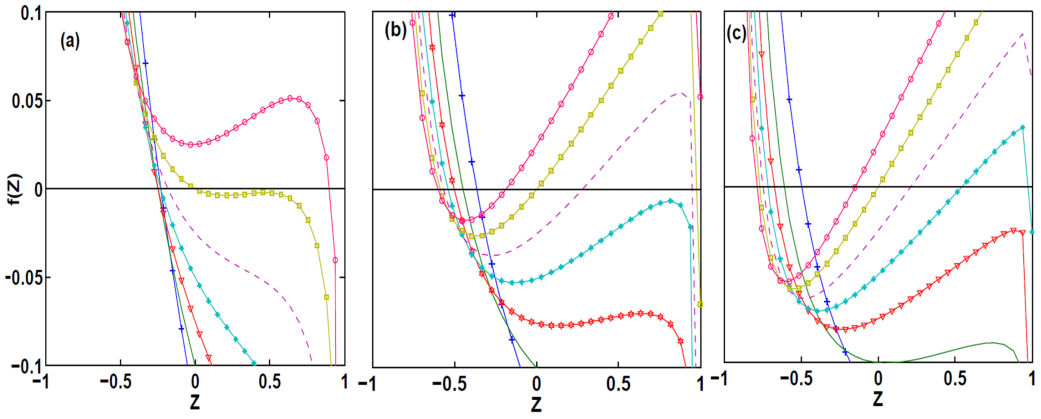

Figure 3.2: $f(Z)$ (Eq. 3.1) for π-phase modes plotted at $\nu_p = 0.15$ with various values of ΔE and (a) $kd = 3$ (b) $kd = 6$ and (c) $kd = 9$ The critical points are the root(s) of $f(Z) = 0$.

3.2 Phase Space Analysis

The dynamical system is usually described by ordinary differential equations subject to initial conditions and controlling parameters. In a phase space, every parameter of the system is given as an axis of a multidimensional space and the phase portrait is a geometric representation of orbits(trajectories) in the phase plane. The dynamical equations are solved and phase trajectories of the system are plotted with respect to various system parameters.

In DWSP-JJ model [67], ΔE presents the shift of fixed point Z^* at $\phi^* = 0$ different from BJJ model where ΔE presents the difference of on-site energies in a double well and parametrizes the symmetry of the system. In order to determine ΔE in a phase plane, we consider various values of ΔE by taking $kd = 12$ and $\nu_p = 0.15$. In Fig. 3.3(a) Λ and ν_p are equal so $\Delta E = 0$. Fixed point Z^* in mixed phased modes ($Z = 0$). In Fig. 3.3(b) Λ is greater than ν_p, $\Delta E > 0$, the fixed point Z^* shifts to surface plasmon dominant modes ($Z < 0$). In Fig. 3.3(c) Λ is smaller than ν_p, $\Delta E < 0$, the fixed point Z^* shifts to soliton dominant modes ($Z > 0$).

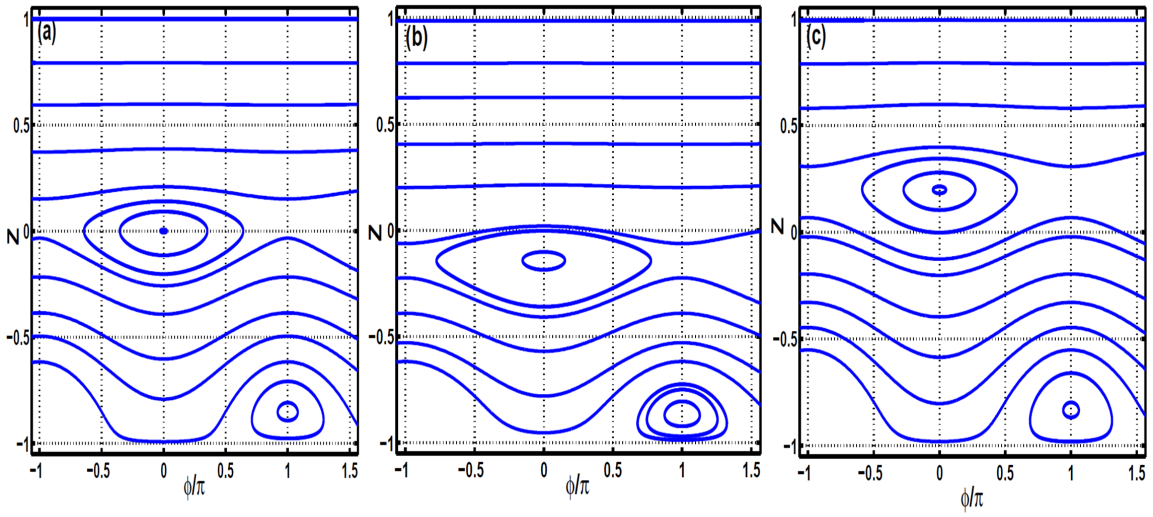

Figure 3.3: Phase-space trajectories of DWSP-JJ with $kd = 12$, $\nu_p = 0.15$ (a) $\Delta E = 0$, $\Lambda = 0.15$ (b) $\Delta E = 0.025$, $\Lambda = 0.175$ (c) $\Delta E = -0.025$, $\Lambda = 0.125$.

Next, we investigate the effect of nonlinearity (Λ) in the DWSP-JJ system. We increase Λ whereas ν_p and kd keep constant. In Fig. 3.4(a) two stable fixed points exist. One of them is at $\phi = 0$ in soliton dominant mode, and other one is at $\phi = \pi$ in surface plasmon dominant mode. For zero phase mode similar to rigid pendulum, photon harmonically oscillates between soliton and surface plasmon dominant modes. At large amplitudes oscillations are anharmonic. At π-phase mode, behavior of system is similar to zero phase mode. In Fig. 3.4(b) by increasing Λ further, system dynamics become very rich and similar to nonrigid pendulum. We observe additional fixed points at $\phi = \pi$. Two of them are stable and one is unstable fixed point. At $\phi = 0$ mode, small amplitude harmonic and large amplitude anharmonic oscillations occur between soliton and surface plasmon dominant modes. At $\phi = \pi$ mode, one of the stable fixed point is at pure soliton modes ($Z^* \approx 1$), other stable fixed point is on the surface plasmon dominant modes whereas unstable one is near to $Z^* = 0$. System also exhibits running trajectories at soliton dominant modes. For this case, photon is initally in soliton dominant mode and continue with the same mode and no transition to surface plasmon dominant mode occurs. In Fig. 3.4(c) we observe one stable fixed point at $\phi = 0$. At $\phi = 0$ mode, photon oscillates harmonically for small amplitudes and anharmonically for large amplitudes between soliton and surface plasmon dominant modes. At $\phi = \pi$ mode, no fixed points exist. Running trajectories dominates the system, full rotation of the pendulum occur. For constant kd and ν_p, increase of nonlinearity reduces the coupling between soliton and surface plasmon modes, decoupling occurs.

In the following, we increase ν_p whereas Λ and kd keep constant. The Fig. 3.5(a) is same as Fig. 3.4(b). In Fig. 3.5(b) two stable fixed points exist. One of them is at $\phi = 0$ on soliton dominant modes and other one is on the plasmon dominant modes at $\phi = \pi$. Large amplitude of running trajectories are observed. In Fig. 3.5(c) photon harmonically oscillates in pure soliton mode at $\phi = 0$, and oscillates in surface plasmon dominant modes at $\phi = \pi$. Running trajectories dominate the system. For $Z \geq 0.5$, photon fully rotates in soliton dominant modes, no transition to surface plas-

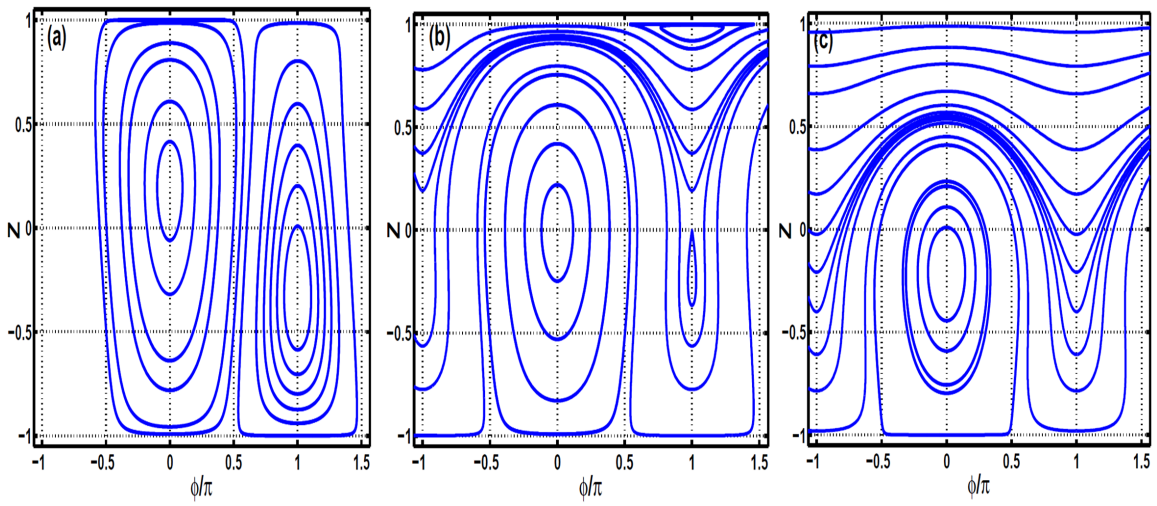

Figure 3.4: Several phase-space trajectories of DWSP-JJ system for $\nu_p = 0.1$, $kd = 6$ (a) $\Lambda = 0.07$, (b) $\Lambda = 0.1$, (c) $\Lambda = 0.14$.

mon dominant modes exist. For $Z \leq 0$, system has no transition to soliton dominant modes, and photon fully rotates in surface plasmon dominant modes. For constant kd and Λ, increase of ν_p reduces the number of fixed points. Mostly, running trajectories are observed.

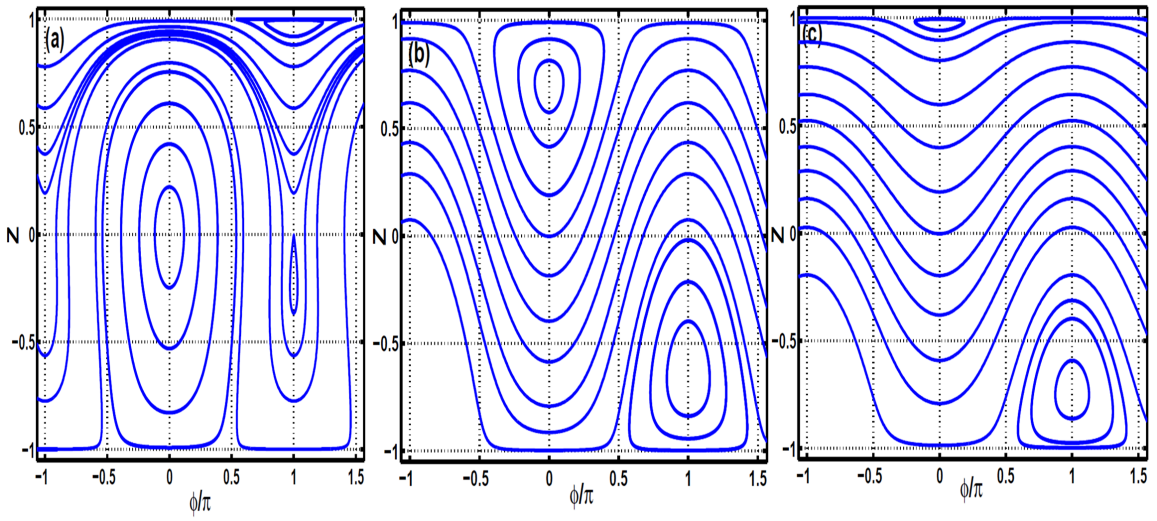

Figure 3.5: Several phase-space trajectories of DWSP-JJ system for $\Lambda = 0.1$, $kd = 6$ (a) $\nu_p = 0.1$, (b) $\nu_p = 0.2$ (c) $\nu_p = 0.3$.

In Figure 3.6(a-c), several phase space trajectories are given for $\Delta E = 0$ with $\nu_p = 0.15$ and $kd = 3$, 6, 12. For $kd = 3$ (Fig. 3.6(a)), zero-phase and π-phase modes exhibit similar behavior, with rigid-pendulum type closed-orbit oscillations at small amplitudes and anharmonic closed-orbit oscillations at large amplitudes. The running phase trajectories consists of $|Z| \sim 1$ plateau connected by a population inversion occuring close to $\phi \sim (2n+1)\pi/2$ points. All these features are similar to the dynamical modes of the BJJ model discussed elsewhere [59, 63, 68]. A drastic change in the phase-space portrait is observed by increasing kd to 6 (Fig 3.6(b)). The anharmonicity of the large-amplitude zero-phase modes become prominent. For the π-phase, three fixed points appear, of which the $Z^* \sim 0.98$ and $Z^* \sim -0.25$ are enclosed by bounded trajectories, whereas the $Z^* = 0$ is an unstable fixed point. In Figure 3.6(c), the increasing kd further ($kd = 12$) results in the decoupling of the system for soliton-dominant initial populations for ($Z(0) > 0.5$). This is expected, since the coupling parameter $q(Z)$ remains small. On the other hand, a surface-plasmon dominant initial population ($Z(0) < 0$) is still effectively strong coupled since the coupling parameter can be close to unity even though kd is large (see Eq. (2.17)). The closed-orbits of the zero phase mode widens in phase towards the two unstable fixed points as opposed to being confined around $|\phi| < \pi/2$. The closed orbit π-phase modes occurs around $Z^* \sim -0.8$. In accordance with Fig. 3.2(c) another fixed point exists that occurs almost at $Z^* = 1$ and invisible in this scale.

The phase trajectories for ($\Delta E \neq 0$) and fixed $\nu_p = 0.15$ are given in Fig. 3.7. Figure 3.7 (a) is plotted for $\Delta E = -0.025$, $kd = 6$. The zero-phase fixed point is located at $Z^* = 0.19$. The π-phase closed modes occur around $Z^* = -0.6$ and in a narrow region around $Z^* \sim 1$. For $\phi(0) = 0$ running phase orbits have large amplitude oscillations for $0.81 < Z < 0.85$ and small oscillations for $0.85 < Z$. The phase diagram for $\Delta E = 0.025$, $kd = 6$ is shown in Fig 3.7 (b). The zero phase mode is at $Z^* = -0.2$. The π-phase mode has closed orbits only around $Z^* = 0.95$. When kd is decreased ($kd = 3$) (Fig.3.7(c)) $\phi = \pi$ mode forms closed orbits around $Z^* = 0.9$. In the BJJ model, the parameter ΔE is a measure of the asymmetry between the two trapping

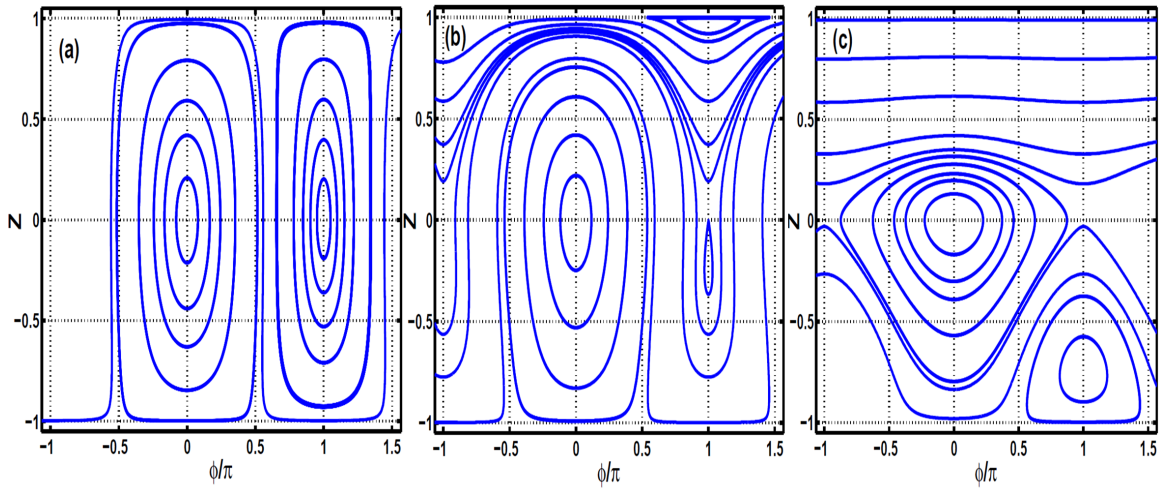

Figure 3.6: Several phase-space trajectories of DWSP-JJ system for $\Delta E = 0$, $\nu_p = 0.1$, $\Lambda = 0.1$, (a) $kd = 3$, (b) $kd = 6$, (c) $kd = 12$.

states of atoms. Evidently, a nonzero ΔE in DWSP-JJ model, this asymmetry is indicated by the location of the $\phi^* = 0, Z^* \neq 0$ fixed points.

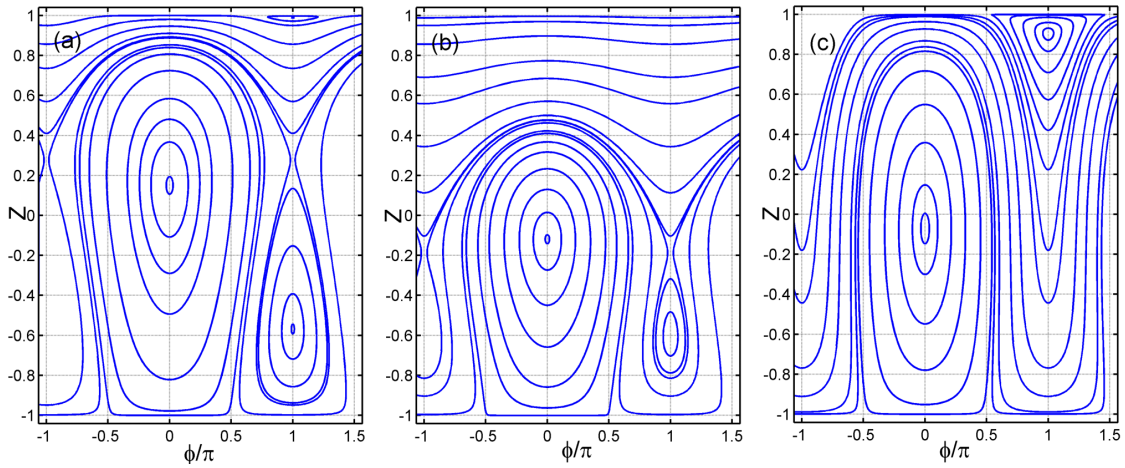

Figure 3.7: Several phase-space trajectories of DWSP-JJ system for (a)$\Delta E = -0.025$, $\nu_p = 0.15$, $kd = 6$, (b) $\Delta E = 0.025$, $\nu_p = 0.15$, $kd = 6$, (c) $\Delta E = 0.025$, $\nu_p = 0.15$, $kd = 3$.

3.3 Phase Space Comparison with Bosonic Josephson Junction Model

In this Section, the phase portraits of BJJ, DWSP-JJ and SJJ are compared which are shown in Fig. 3.8(a-c), respectively. The dynamical behavior of BJJ system under varius ΔE is investigated. The normalized SJJ AC current is plotted for a constant junction potential. A detailed comparison between SJJ and BJJ was reported in the literature [68]. But this Section is mostly based on the comparison of the BJJ and DWSP-JJ phase space features. The BJJ model is depicted with an effective coupling constant of $q \sim 0.03$ which is within the dynamic range of the $q(Z)$ of DWSP-JJ. The phase space of BJJ is decorated with open and bounded phase trajectories that are symmetric with respect to the Z axis. The $\phi(0) = 0$ trajectories are bounded for $|Z(0)| < 0.8$. The bounded orbits are harmonic for $|Z(0)| < 0.5$ and become anharmonic for $0.5 < Z(0) < 0.8$. The $\phi(0) = \pi$ trajectories are open for $|Z(0)| < 0.9$ and become bounded anharmonic orbits for $0.9 < |Z(0)| < 1$. In the DWSP-JJ phase portrait plotted with a comparable parameter set (Fig. 3.8(b)), the asymmetry in Z induced by the dynamical coupling parameter is prominent. The DWSP-JJ acts like a double-well trap BJJ system, where the barrier height (i.e. the coupling) between the two wells depends on the population of one well (i.e. the soliton amplitude). The bound trajectories are strongly anharmonic except for $|Z(0)| < 0.2$. For $\phi(0) = 0$, the orbits are closed for all negative $Z(0)$ values and for positive $Z(0) < 0.55$. The $\phi(0) = \pi$ states are bounded for $-0.9 < Z(0) < 0$.

3.4 Spatial Propagation Properties

3.4.1 Plot and Analysis of $Z(\xi)$, $\phi(\xi)$, and $q(\xi)$

The remarkable property of the DWSP-JJ system is the Z-dependence of the coupling parameter which causes rich dynamics in the phase space. In this Section, the variation of $Z(\xi)$, $q(Z(\xi))$, and $\phi(\xi)$ for various trajectories from Fig. 3.7(a) is investigated. The Figure 3.9 shows the propagation with initial relative phase $\phi(0) = 0$ for different initial values of $Z(0)$. These values are chosen to consider both soli-

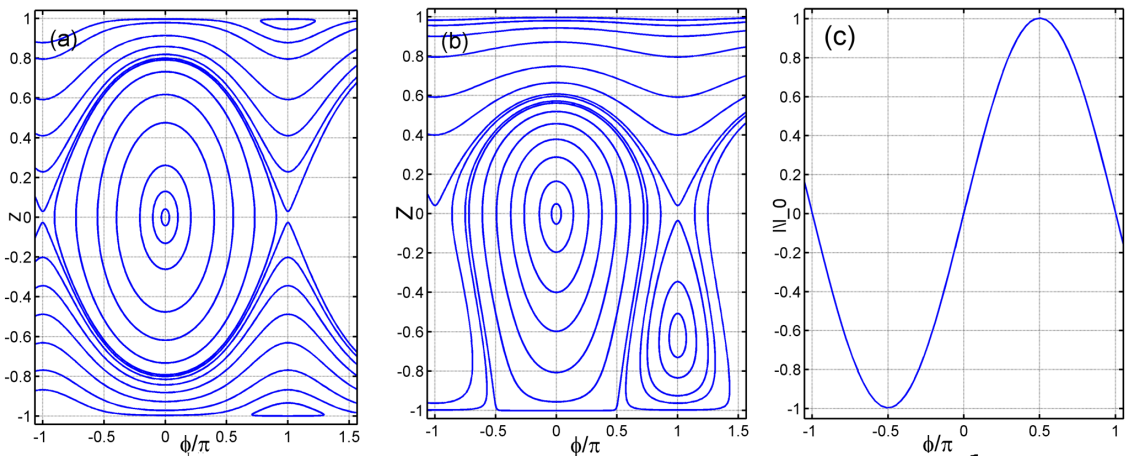

Figure 3.8: Comparison of the phase-space trajectories of (a) BJJ ($q \equiv 0.03$, $\Delta E = 0$, $\Lambda = 0.15$) and (b) DWSP-JJ ($kd = 6$, $\Delta E = 0$, $\Lambda = 0.15$) and (c) SJJ models

ton dominant modes, and surface plasmon dominant modes as well as mixed phase modes. In Fig 3.9(a), Z vs ξ is plotted. In Fig. 3.9(b), $q(\xi)$ is plotted. The coupling parameter is calculated with respect to $\phi(0) = 0$ and $Z(0) = -0.997$, $Z(0) = 0.03$, $Z(0) = 0.879$, $Z(0) = 0.997$. As we expected from the functional form in Eq. (2.17), the coupling parameter shows variations commensurate with that of the population imbalance. Small amplitude oscillations (Fig. 3.9(a), circle and dotted line) have small, almost constant $q(Z) \approx 0$ (Fig. 3.9(b), circle and dotted line) whereas large amplitude oscillations (Fig. 3.9(b), triangle and square) exhibit impulsive behavior of the coupling in Fig. 3.9(b). In the Fig. 3.9(c) the relative phase difference vs ξ is plotted for same initial populations. In Fig. 3.10(a) Z vs ξ and in Fig. 3.10(b), $q(\xi)$ is plotted with respect to $\phi(0) = \pi$ and $Z(0) = -0.997$, $Z(0) = -0.942$, $Z(0) = -0.69$, $Z(0) = 0.96$. Small amplitude oscillations (Fig. 3.10(a), square and dotted line) have (Fig. 3.10(b)), small variations in $q(Z)$ and almost constant for $Z = -0.96$. Large amplitude oscillations (Fig. 3.10(a), circle and triangle) exhibit impulsive behavior of $q(Z)$ (Fig. 3.10(b), circle and triangle). Relevant phase space trajectories of the DWSP-JJ are plotted in Fig. 3.11 by setting the control parameters $\Delta E = -0.025$, $kd = 6$, $\nu_p = 0.15$. In Fig. 3.11(a) ($\phi(0) = 0$) $Z(0) = -0.997$ (blue-line), the system

is in pure surface plasmon mode ($Z \approx -1$). A closed orbit with large amplitude anharmonic oscillations occur and the system exhibits large variations of the coupling parameter $q(Z)$. For $\phi(0) = 0$, $Z(0) = 0.03$ (red-circle), the system is initially in mixed population mode ($Z \approx 0$). A closed orbit with small amplitude harmonic oscillations exist and the system exhibits small coupling parameter $q(Z)$. For $\phi(0) = 0$ and $Z(0) = 0.997$ (black-dashed line), the system is in pure soliton mode ($Z \approx 1$). A running orbit with small amplitude harmonic oscillations occur, and the system exhibit almost constant coupling parameter $q(Z)$. In this case, the system is weakly coupled with $q(Z) \approx 0$. The Fig 3.11(b) similar to Fig. 3.11 (a), system is investigated for $\phi(0) = \pi$ with various $Z(0)$. In Fig. 3.11(b) ($\phi(0) = \pi$) $Z(0) = -0.997$ (blue-line), the system is in pure surface plasmon mode ($Z \approx -1$). A open orbit with large amplitude anharmonic oscillations occur and the system exhibits large variations of $q(Z)$. For $Z(0) = 0. - 69$ (pink-line), the system is initially in surface plasmon dominant mode. A closed orbit with small amplitude harmonic oscillations exist and the system exhibits large variations in $q(Z)$. For $Z(0) = 0.96$ (black-dashed line), the system is in pure soliton mode ($Z \approx 1$). A running orbit with small amplitude harmonic oscillations exist, and the system is weakly coupled with $q(Z) \approx 0$. To summarize, both $\phi(0) = 0$ and $\phi(0) = \pi$ in soliton dominant modes, system has small almost constant $q(Z)$. The soliton and surface plasmon system almost decoupled. However, in surface plasmon dominant modes system exhibits large changes of $q(Z)$.

3.4.2 Total Wave Function

The system is represented via the total field Ansatz as in the Eq. 3.2. The c_p, c_s are plasmon and soliton amplitudes. The Ψ_p and Ψ_s are the uncoupled plasmon and soliton fields. Here the ψ_p and ψ_s are the transverse fields of plasmon and soliton. In order to describe the coupled system under the Bosonic Josephson Junction model, the total field ansatz is defined in terms of population imbalance Z, and relative phase difference ϕ. Therefore the soliton and plasmon amplitudes are rewritten in terms

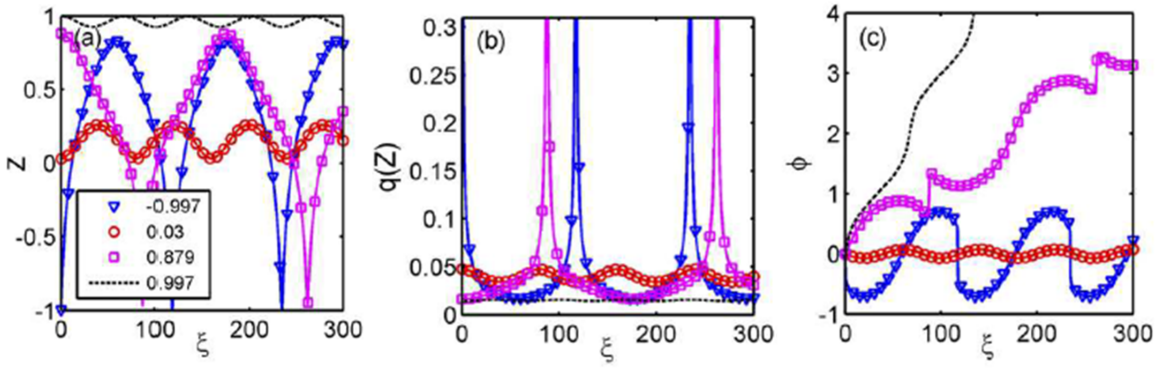

Figure 3.9: Spatial propagation of (a) Z (b) $q(Z)$, and (c) ϕ for initial values of $\phi(0) = 0$ and $Z = -0.997$(blue-triangle), $Z = 0.03$(red-circle), $Z = 0.879$(pink-square), $Z = 0.997$ (black-dashed line).

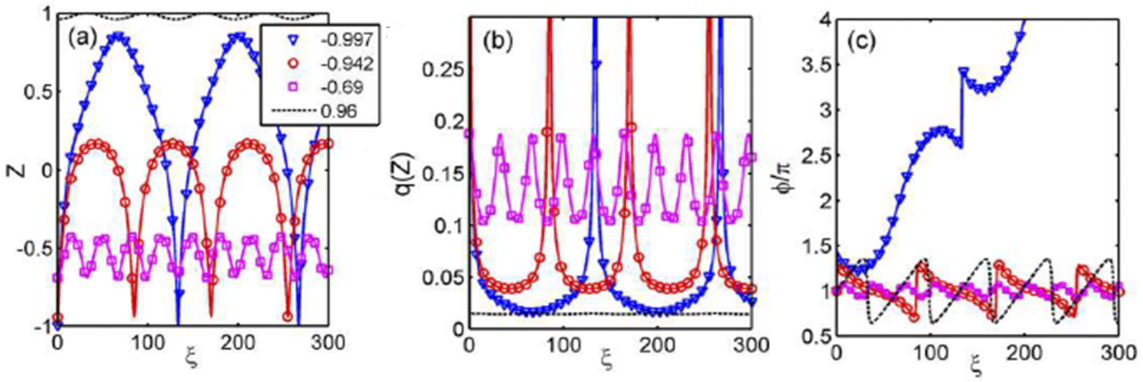

Figure 3.10: Spatial propagation of(a) Z (b) $q(Z)$, and (c) ϕ for initial values of $\phi(0) = \pi$ and $Z = -0.997$(blue-triangle), $Z = -0.942$(red-circle), $Z = -0.69$(pink-square), $Z = 0.96$ (black-dashed line).

of relative phase difference in Eq. 3.5, and Eq. 3.6 respectively. The dimensionless propagation constant for plasmon given in Eq. 3.7 and Eq. 3.8. The total field ansatz for DWSP-JJ (Eq. 3.9) is built by substituting both the Eq. 3.5 and Eq. 3.6 as well as Eq. 3.8 into Eq. 3.2. In Eq. 3.9, N is the total field with $N = |C_p|^2 + |C_s|^2$ and $N \equiv 1$, ν_p is the small deviations of the dimensionless propagation constant of surface plasmon, kd is dimensionless distance between surface plasmon and soliton, and Λ is the nonlinearity parameter of the coupled system. The total field Ansatz is in the

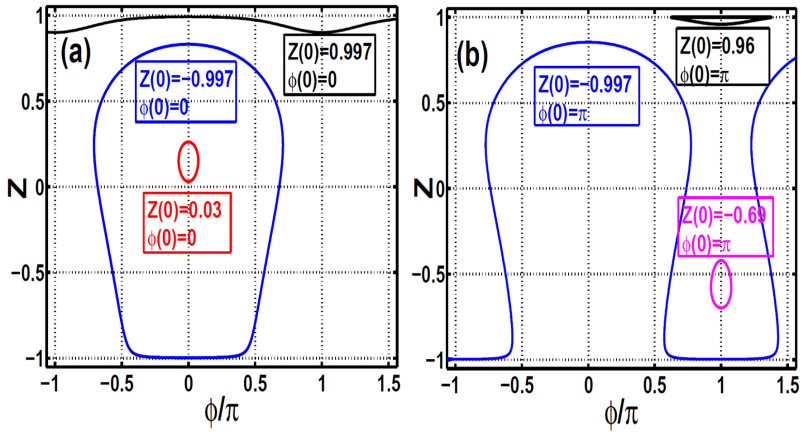

Figure 3.11: The corresponding phase portraits for (a) $Z = -0.997$, $Z = 0.03$, $Z = 0.997$ at $\phi(0) = 0$ (b) $Z = -0.997$, $Z = -0.69$, $Z = 0.96$ at $\phi(0) = \pi$.

following :

$$\Psi(x, y) = c_p(y)\psi_p(x) + c_s(y)\psi_s(x, |c_s|) \tag{3.2}$$

$$\psi_p = e^{\sqrt{k_p^2 - k^2}} \tag{3.3}$$

$$\psi_s = sech(k\sqrt{\frac{\gamma}{2}}|c_s|(x - d)) \tag{3.4}$$

$$c_p = |C_p|e^{i\phi_p} \tag{3.5}$$

$$c_s = |C_s|e^{i\phi_s} \tag{3.6}$$

$$\begin{aligned} \beta_p &= \tfrac{k_p}{k} \\ \nu_p &\equiv \beta_p - 1 \end{aligned} \tag{3.7}$$

$$\beta_p \equiv \nu_p + 1 \tag{3.8}$$

$$\begin{aligned} |\Psi|^2 = 0.5N[e^{-2kx\sqrt{\nu_p^2+2\nu_p}}(1 - Z) + sech^2(k\sqrt{4\Lambda}(x - d)(1 + Z)) + \\ 2(e^{-kx\sqrt{\nu_p^2+2\nu_p}} \cos\phi sech^2(k\sqrt{4\Lambda}(x - d))(\sqrt{1 - Z^2}))] \end{aligned} \tag{3.9}$$

In Fig. 3.12 and Fig. 3.13, the total field of the soliton and surface plasmon is plotted for different initial values of the population imbalances with initial relative phases $\phi(0) = 0$ and $\phi(0) = \pi$, respectively. The model parameters are taken from the Fig. 3.7(a) for $\Delta E = -0.025$, $\nu_p = 0.15$, $kd = 6$ and $\Lambda = 0.125$. In Fig. 3.12,

the total field is plotted for $\phi(0) = 0$ with (a) $Z(0) = 0.997$, (b) $Z(0) = 0.03$, (c) $Z(0) = -0.997$. In Fig. 3.13, the total field is plotted for $\phi(0) = \pi$ with (a) $Z(0) = -0.997$, (b) $Z(0) = -0.69$,(c) $Z(0) = 0.96$. The $|\Psi|^2$ is plotted for one period for all figures. Both Fig. 3.12 and Fig. 3.13, value of propagation coordinate $\xi = ky$, changes with respect to $Z(0)$. When system exhibits small amplitude oscillations such as Fig. 3.12 ($\phi(0) = 0$)(b) $Z(0) = 0.03$ one period is completed in a short distance $\xi = 5$. However, for large amplitude oscillations like Fig. 3.12(c) $Z(0) = -0.997$ and Fig. 3.12(a) $Z(0) = 0.997$ one period is completed in $\xi = 10$, and $\xi = 20$ which are two and four times larger than ξ of Fig. 3.12(b). In Fig. 3.13($\phi(0) = \pi$) (a) $Z(0) = 0.96$ and Fig. 3.13(c) $Z(0) = -0.997$ system exhibits large amplitude oscillations. A period is completed in $\xi = 20$ whereas in Fig. 3.13(c) for $Z(0) = -0.69$ it is completed in $\xi = 15$.

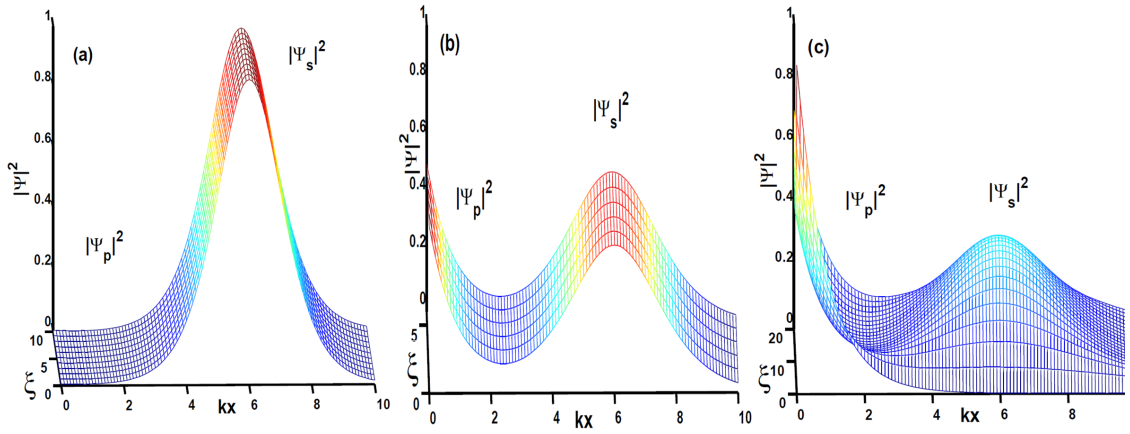

Figure 3.12: $|\Psi|^2$ vs kx and ξ. $\Delta E = -0.025$, $\nu_p = 0.15$, $kd = 6$, $\Lambda = 0.125$ (a) $\phi(0) = 0$ $Z(0) = 0.997$, (b) $\phi(0) = 0$ $Z(0) = 0.03$,(c) $\phi(0) = 0$ $Z(0) = -0.997$.

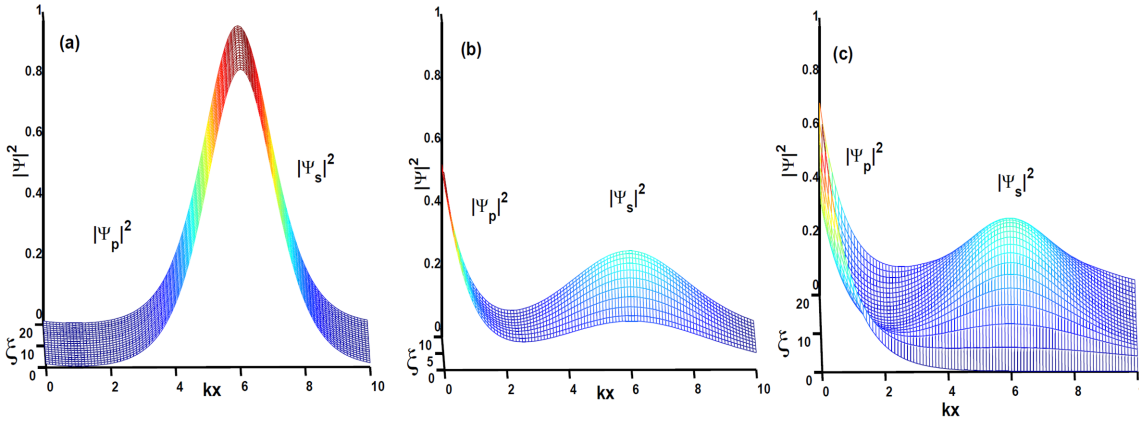

Figure 3.13: $|\Psi|^2$ vs kx and ξ. $\Delta E = -0.025$, $\nu_p = 0.15$, $kd = 6$, $\Lambda = 0.125$ (a) $Z(0) = 0.96$, $\phi(0) = \pi$ (b) $Z(0) = -0.69$, $\phi(0) = \pi$ (c) $Z(0) = -0.997$, $\phi(0) = \pi$.

3.5 Experimental Aspects

There are some typical parameter values that may serve as guidance for the experimentally realization of the system. For the infrared regime, the chalcogenide [69] glasses can provide the medium for soliton propagation [70]. They have a transmission band $0.7 - 10\mu m$, linear dielectric constant around $\sim 5 - 8$ and nonlinear index of refraction $n_2 = 10^{-16} m^2/W$. In these materials, the nonlinearity parameter γ $5 \times 10^{-}3$ can be achievable. For doped silica fibers, nonlinearity will be almost 2 orders weaker [71]. Surface plasmons are typically studied on gold or silver surfaces [72]. Depending on the lateral extend of the evanescent surface-plasmon and soliton fields, the kd for weak coupling regime would be typically around $\sim 10 - 100$ [15]. Considering the phase space portrait for $kd = 12$ given in Fig. 3.6 (c), we conclude that some of the features presented in the phase space may be suppressed under experimental conditions.

In the proper assessment of experimental feasibility, damping effect has to be taken account. Up to know it is is not considered. However, the qualitative features demonstrated that DWSP-JJ model expected to be present under weak dissipative conditions. In the DWSP-JJ coupled model, the nonlinearity of the system is defined

with both η and Λ. We investigate the control parameters of the system in range $0.1 < \nu_p < 0.35$, $0.1 < \eta < 0.35$, and $0.05 < \Lambda < 0.175$ to observe the resonant coupling of the DWSP-JJ ($\nu_p = 0.2$, $\eta = 0.2$) [15]. Since ν_p is the small deviations of the dimensionless propagation constant of surface plasmon and $\nu_p << 1$, small values imply $k_p \approx k$ regime. The η values considered in DWSP-JJ model, represent strong nonlinearity when compared with actual physical values. In the model the dimensionless distance between the surface plasmon and optical soliton kd,is investigated between the range 3-12. The values of the incoming light wave vector should be close to the wave vector of surface plasmon. By considering the Eq. 3.10, the nonlinearity parameter γ is defined in a range $0.4 < \gamma < 1.4$ with N is the total field $N = |C_p|^2 + |C_s|^2$ and $N \equiv 1$. The result shows that the γ should be very strong to generalize the DWSP-JJ model experimentally. The nonlinearity parameter γ is related to nonlinear refrective index n_2 by Eq. 3.12,where A_{eff} is the effective core area of the fiber and k is the incoming light wave vector.

$$\begin{aligned} \eta &= \tfrac{\gamma N}{4} \\ \Lambda &= \tfrac{\eta}{2} \end{aligned} \tag{3.10}$$

$$\nu_p = \frac{k_p}{k} - 1 \tag{3.11}$$

$$\gamma = \frac{n_2 k}{A_{eff}} \tag{3.12}$$

Chapter 4

DISSIPATIVE DWSP-JJ MODEL

In this chapter, we focus on DWSP-JJ coupled system in the presence of damping. The equation of motion of the system is introduced in Sec. 4.1, dynamical analysis are presented in Sec. 4.2 by phase portraits, and the corresponding spatial propagation properties are introduced in Sec. 4.3.

4.1 Dissipative Model

In order to investigate the damping effect on the DWSP-JJ model, we introduced the damping "ζ"term into the system. The damping parameter is considered in order of 10^{-3} to 10^{-1} for observe more clearly decaying period of the trajectory. We focus on damping through angular velocity (Eq. 4.3, $\dot{Z} = -\zeta\dot{\phi}$). However, in two state systems, for instance, two condensates in different hyperfine levels in a single harmonic trap, connected by tunnelling transitions [73] can have the damping from the finite lifetime of excited states through the angular momentum $\dot{Z} = -\zeta Z$.

We adopt the Bosonic Josephson Junction dynamical equations for nonrigid pendulum with damping in Ref [74] :

$$\dot{Z} = -\sqrt{1 - Z^2}\sin\phi - \alpha\dot{\phi}, \tag{4.1}$$

$$\dot{\phi} = \Lambda Z + \Delta E + \frac{Z}{\sqrt{1 - Z^2}}\cos\phi. \tag{4.2}$$

In the presence of damping equations of motion for the surface plasmon-soliton coupled system becomes :

$$\dot{Z} = -q(Z)\sqrt{1 - Z^2}\sin\phi - \zeta\dot{\phi}, \tag{4.3}$$

$$\dot{\phi} = \Lambda Z + \Delta E + \frac{q(Z)Z}{\sqrt{1 - Z^2}}\cos\phi. \tag{4.4}$$

4.2 Phase Space Analysis

The dynamical behavior of the coupled DWSP-JJ model is studied under various damping term ζ values. First of all, we consider $Z(0) = -0.63$, $\phi(0) = -3.2$ in Fig. 4.1. The system is initially in surface plasmon dominant mode. In Fig. 4.1(a), we considered $\zeta = 0.005$ and increased the order of the damping term as (b)$\zeta = 0.05$ and (c)$\zeta = 0.15$. According to the applied damping order, trajectory comes to rest in shorter periods. For all three cases, we observe that π-phase modes decay to zero-phase modes. The photon transfers from surface plasmon dominant mode to mixed-phased mode. At low dissipation, the phase space is no longer between ± 1, it is extended. We can squeezed in the phase space as in Fig. 4.1(b) and Fig. 4.1(c) by increasing the dissipation value. In Fig. 4.2, we investigate the system for $Z(0) = -0.25$, $\phi(0) = -0.92$. In order to observe phase-slip clearly, we just consider (a)$\zeta = 0.05$ and (b)$\zeta = 0.15$ respectively. The photon is initially in surface plasmon dominant mode by damping effect transfers to mixed-phased mode. The π-phase modes decay to zero-phase modes. Next, we consider the same initial relative phase $\phi(0) = 1$ with different Z values in Fig. 4.3(a), and Fig. 4.3(b). In Fig. 4.3(a), system is initially in surface plasmon dominant mode by $\zeta = 0.15$ it transfers to pure soliton mode. Due to the damping, the phase space is extended. In Fig. 4.3(b), photon is in pure soliton mode $Z(0) = 0.96$, by $\zeta = 0.05$ transfers to mixed phase mode. The π-phase modes decay to zer-phase modes. To summarize, the fixed points take the role of sources and sinks in the phase space. Damping also results in the so-called "phase-slip"effect where the π-phase modes (odd) decay into zero-phase modes (even).

In the following, we investigated $\phi(0)$ with various values of initial $Z(0)$. In both cases system is initially in π-phase modes. We considered the case in Fig. 3.7(a) and studied the system under the effect of $\zeta = 0.05$ in Fig. 4.4(a). We observed that for the stable fixed point at $\phi = \pi$ ($\phi(0) = -3$), which is in the pure soliton mode is mapped to the $\phi = 0$ ($\phi(0) = 2$). The fixed points at $\phi = \pi$ decays to the trajectories at $\phi = 0$. In the presence of dissipation, open orbits at $Z > 0.6$ become bounded. In the Fig. 4.4(b) for the same case the damping parameter is increased to $\zeta = 0.15$,

the extended phase space is squeezed and fixed points at $\phi = \pi$ decays to the $\phi = 0$ mode.

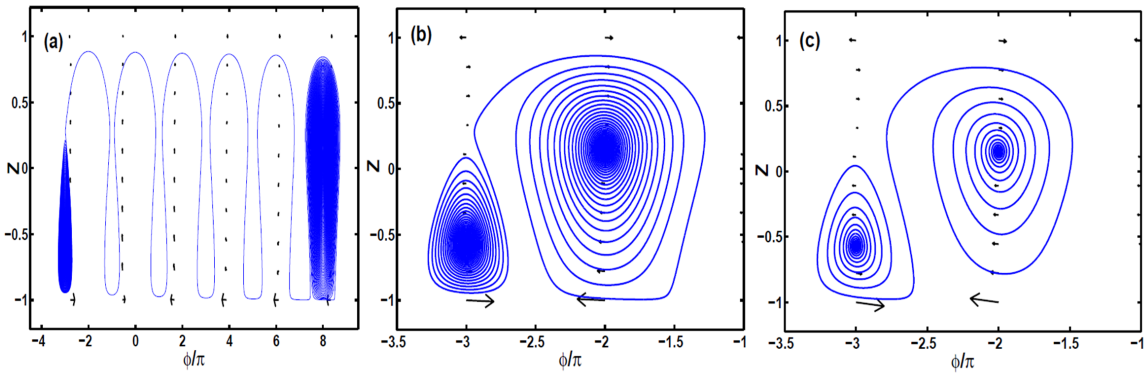

Figure 4.1: Phase portraits of the damped system $Z(0) = -0.63$, $\phi(0) = -3.2$, $\Delta E = -0.025$, $\Lambda = 0.125$, $kd = 6$ (a) $\zeta = 0.005$, (b) $\zeta = 0.05$ (c) $\zeta = 0.15$.

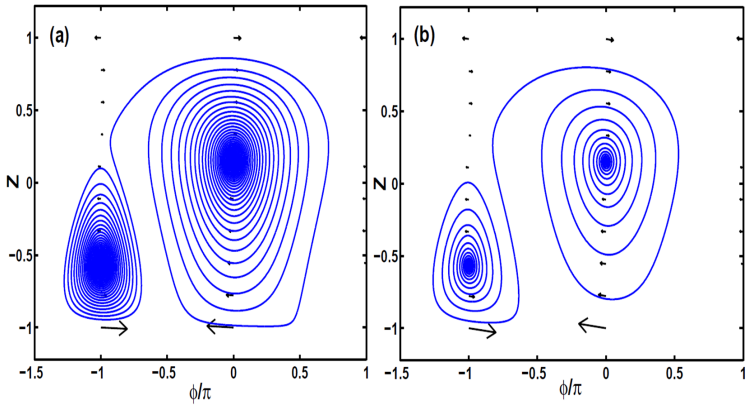

Figure 4.2: Phase portraits of the damped system $Z(0) = -0.25$, $\phi(0) = -0.92$, $\Delta E = -0.025$, $\Lambda = 0.125$, $kd = 6$ (a) $\zeta = 0.05$ (b) $\zeta = 0.15$.

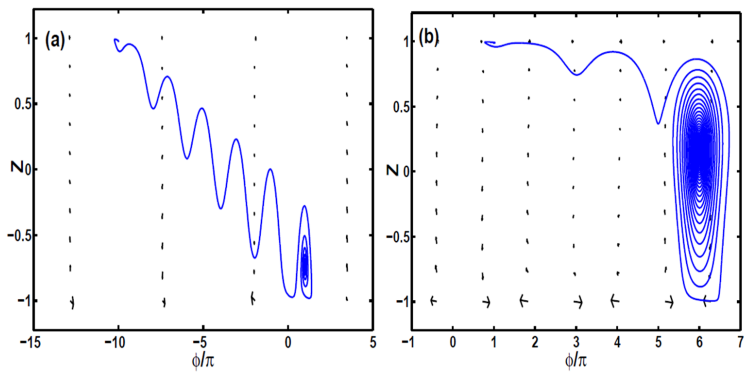

Figure 4.3: Phase portraits of the damped system $kd = 6$, $\Delta E = -0.025$, $\Lambda = 0.125$ (a) $Z(0) = -0.28$, $\phi(0) = 1$, $\zeta = 0.05$ (b) $Z(0) = 0.96$, $\phi(0) = 1$, $\zeta = 0.15$.

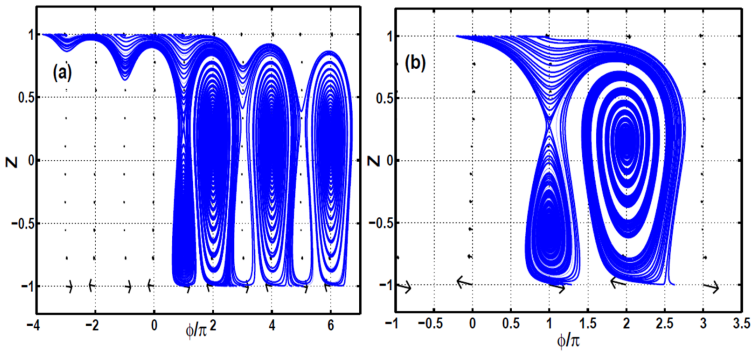

Figure 4.4: Phase portraits of the damped system $kd = 6$, $\Delta E = -0.025$, $\Lambda = 0.125$ (a) $\phi(0) = -3$, $\zeta = 0.15$ (b) $\phi(0) = 1$, $\zeta = 0.05$.

4.3 Spatial Propagation Properties

In this Section, the variation of $Z(\xi)$, $\phi(\xi)$, and $q(Z(\xi))$, are investigated for the corresponding damped systems in Sec. 4.2 respectively. In Fig. 4.5 damping is $\zeta = 5 \times 10^{-3}$ whereas in Fig. 4.6 is $\zeta = 5 \times 10^{-2}$, and in Fig. 4.7 is $\zeta = 0.15$. In these cases system initially in surface plasmon dominant mode ($Z(0) = -0.63$, $\phi(0) = -3.2$). In Fig. 4.5(a), Fig. 4.6(a), and Fig. 4.7(a) due to the damping, behavior of the system is not periodic. It exhibits both large and small oscillations. For large oscillations anharmonic oscillations occur. The system decays to zero modes. As damping increases, system reduce to zero mode at small ξ values. The phase-slip

is observed in Fig. 4.5(b), Fig. 4.6(b), Fig. 4.7(b). The source of system modes at $\phi = \pi$ and sink at $\phi = 0$ modes. The coupling parameter depends on soliton amplitude. The increase of soliton amplitude reduces the coupling constant. They have an exponentially decaying relation (Eq. (2.17)). Both Fig. 4.5(c), and Fig. 4.6(c) as well as Fig. 4.7(c) coupling parameter has its highest value at surface plasmon dominant mode and reduces by the system decays to zero modes. Next, we investigate the spatial propagation properties of $Z(0) = -0.25$, $\phi(0) = -0.92$. System is initially in surface plasmon dominant mode. In Fig. 4.8(a), Fig. 4.9(a), system exhibits both large and small oscillations whereas large oscillations are anharmonic. System decays to zero mode. The phase-slip from $\phi = \pi$ to $\phi = 0$ modes are observed in Fig. 4.8(b), Fig. 4.9(b). The coupling of the system under damping is shown in Fig. 4.8(c), Fig. 4.9(c). The highest value of the parameter in Fig. 4.8(c) is $q \approx 0.75$ whereas in Fig. 4.8(c) is $q \approx 0.55$.

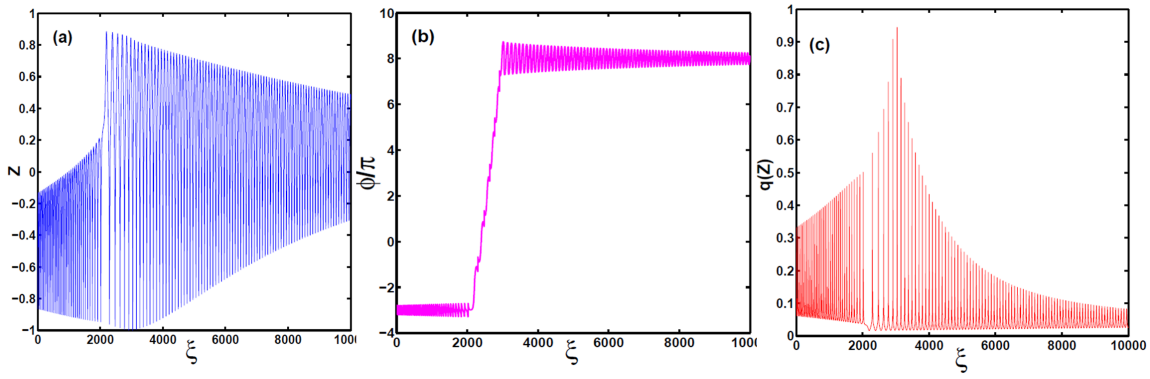

Figure 4.5: Propagation of (a) Z , (b) ϕ/π, (c) coupling parameter $q(Z)$ for $Z(0) = -0.63$, $\phi(0) = -3.2$ damped system $\zeta = 5 \times 10^{-3}$, $\Delta E = -0.025$, $\Lambda = 0.125$, $kd = 6$.

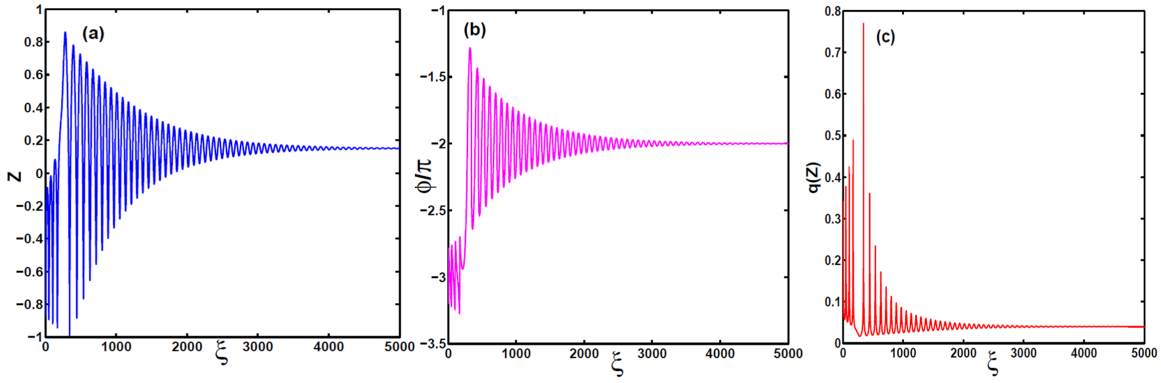

Figure 4.6: Propagation of (a) Z , (b) ϕ/π, (c) coupling parameter $q(Z)$ for $Z(0) = -0.63$, $\phi(0) = -3.2$ damped system $\zeta = 5 \times 10^{-2}$, $\Delta E = -0.025$, $\Lambda = 0.125$, $kd = 6$.

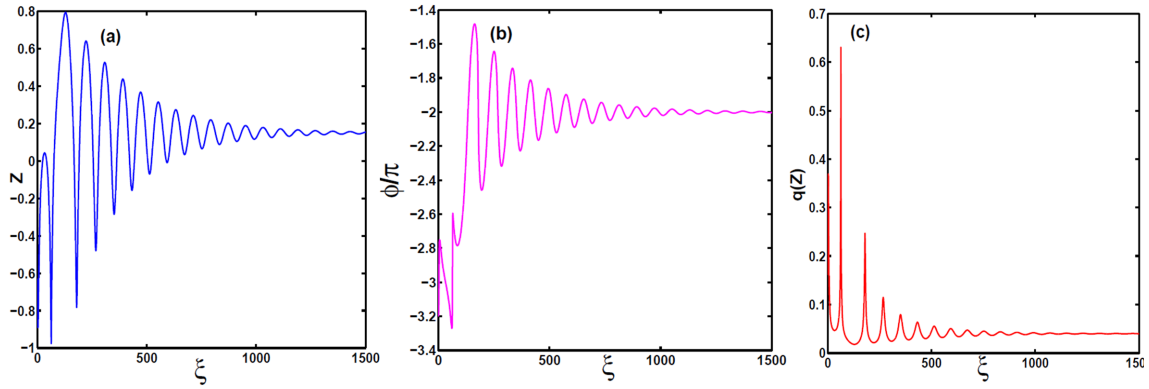

Figure 4.7: Propagation of (a) Z , (b) ϕ/π, (c) coupling parameter $q(Z)$ for $Z(0) = -0.63$, $\phi(0) = -3.2$ damped system $\zeta = 0.15$, $\Delta E = -0.025$, $\Lambda = 0.125$, $kd = 6$.

In Fig. 4.10 $Z(0) = -0.28$, $\phi(0) = 1$ is isvestigated. The damping value of the system is $\zeta = 0.15$. In Fig. 4.10(a) system is initially surface plasmon dominant mode and transfers to pure soliton dominant mode and trapped. The phase slip in Fig. 4.10(b) is observed from $\phi = \pi$ to $\phi = 0$ modes. Initially, the coupling parameter of the system is large. However, due to the increase of the soliton amplitude q decreases and close to almost consatnt value in Fig. 4.10(c). The final case is the $Z(0) = 0.96$ with $\phi(0) = 1$. Initially, system is in pure soliton mode. In Fig. 4.11(a), large amplitude anharmonic oscillations are observed. Then, the system decays to zero mode. Fig. 4.11(b), the corresponding phase relation shows the phase-slip between

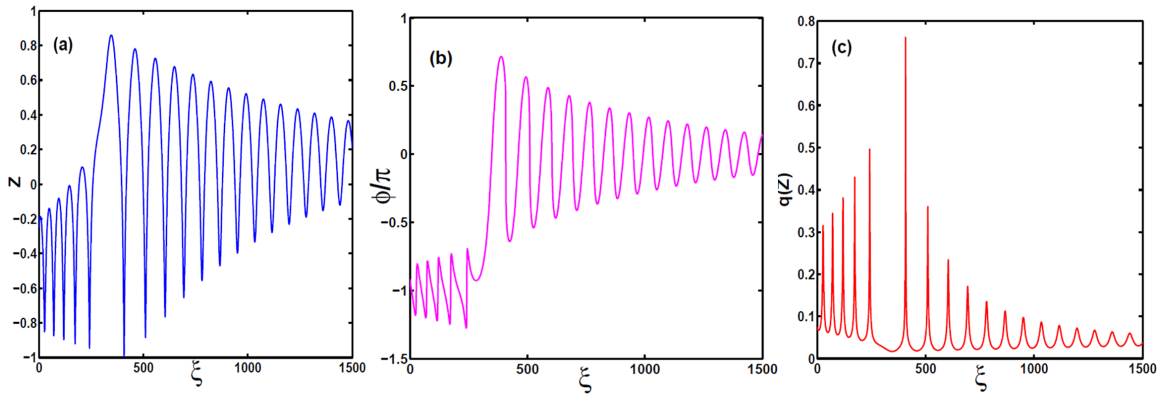

Figure 4.8: Propagation of (a) Z , (b) ϕ/π, (c) coupling parameter $q(Z)$ for $Z(0) = -0.25$, $\phi(0) = -0.92$ damped system $\zeta = 5 \times 10^{-2}$, $\Delta E = -0.025$, $\Lambda = 0.125$, $kd = 6$.

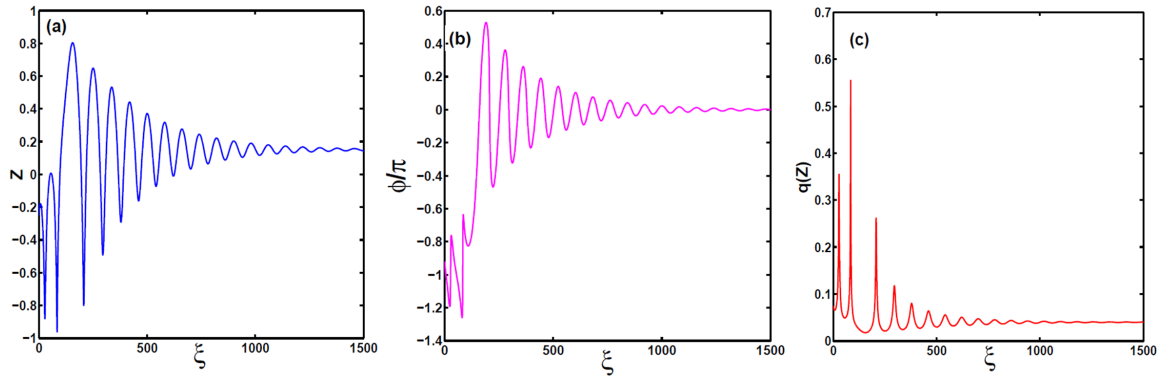

Figure 4.9: Propagation of (a) Z , (b) ϕ/π, (c) coupling parameter $q(Z)$ for $Z(0) = -0.25$, $\phi(0) = -0.92$ damped system $\zeta = 0.15$, $\Delta E = -0.025$, $\Lambda = 0.125$, $kd = 6$.

the π and zero modes. In Fig. 4.11(c), the coupling parameter decreases due to the high soliton amplitude. Then q increases as soliton amplitude decreases. The value of the coupling is almost constant when the system decays to zero mode.

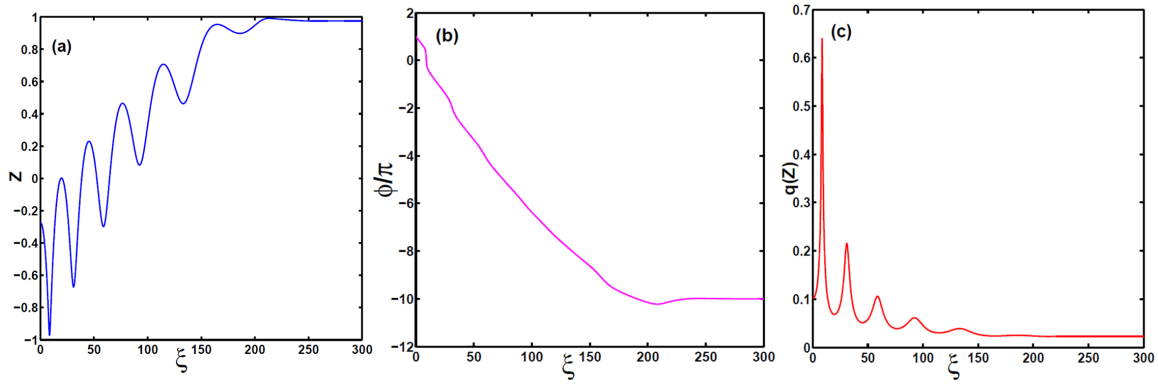

Figure 4.10: Propagation of (a) Z , (b) ϕ/π, (c) coupling parameter $q(Z)$ for $Z(0) = -0.28$, $\phi(0) = 1$ damped system $\zeta = 0.15$, $\Delta E = -0.2$, $\Lambda = 0.1$, $kd = 6$.

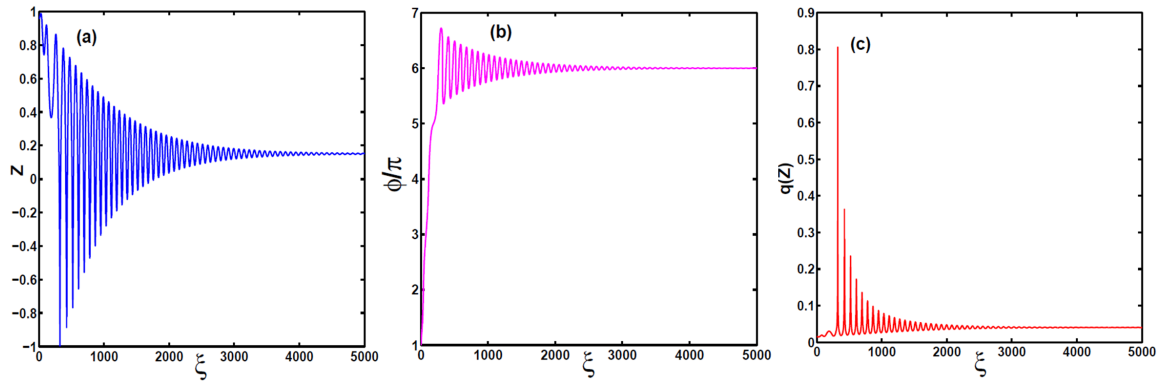

Figure 4.11: Propagation of (a) Z , (b) ϕ/π, (c) coupling parameter $q(Z)$ for $Z(0) = 0.96$, $\phi(0) = 1$ damped system $\zeta = 0.05$, $\Delta E = -0.2$, $\Lambda = 0.1$, $kd = 6$.

Chapter 5

SHAPIRO EFFECT

The Shapiro effect is the one of the most remarkable property of superconducting devices. It is spesific phenomenon that emerges when the frequency of the external field is commensurate with the intrinsic frequency of the system. It also provides a method for measuring the constant of nature $\frac{2e}{\hbar}$ with such precision and universality [75, 76] that since 1972 the revesed view has been adopted wherby $\frac{2e}{\hbar}$ is assumed to be known and it is used to define a standard unit of voltage [77, 78]. The Shapiro resonant modulation of the energy bias leads to a DC current accross the junction. In the inverse Josephson effect DC voltages are induced across an unbiased junction with the aid of an external microwave field. In this case current steps at constant voltages are occured. The total current is given in Eq. 5.1 :

$$I_t = I + I_{rf} cos(\omega_{rf} t) \tag{5.1}$$

The numerical solution of the total current (Eq. 5.1) leads to Shapiro steps. The effective applied voltage to the Josephson Junction is :

$$V(t) = V_0 + V_{rf} cos(\omega_{rf} t) \tag{5.2}$$

The substitution of Eq. 5.2 into Josephson dynamical equations Eq. 1.11 and Eq. 1.12 yields :

$$\phi(t) = \phi_0 + \frac{2e}{\hbar} V_0 t + \frac{2e}{\hbar \omega_{rf}} V_{rf} sin(\omega_{rf} t) \tag{5.3}$$

and the corresponding Josephson current is :

$$\begin{aligned} I(t) &= I_0 sin(\phi_0 + \tfrac{2eV_0}{\hbar} t + \tfrac{2eV_{rf}}{\hbar\omega_{rf}} sin(\omega_{rf} t)) \\ \tfrac{2eV_0}{\hbar} &= \omega_{ac} \\ I(t) &= I_0 sin(\phi_0 + \omega_{ac} t + \tfrac{\omega ac}{\omega_{rf}} \tfrac{V_{rf}}{V_0} sin(\omega_{rf} t)) \end{aligned} \tag{5.4}$$

Next, we write m to simplify the Eq. 5.4 :

$$\begin{aligned} m &= \tfrac{\omega ac}{\omega_{rf}} \tfrac{V_{rf}}{V_0} \\ I(t) &= I_0 sin(\omega_{ac} t + \phi_0 + m sin(\omega_{rf} t)) \\ I(t) &= I_0[sin(\omega_{ac} t + \phi_0) cos(m sin(\omega_{rf} t)) + sin(m sin(\omega_{rf} t)) cos(\omega_{ac} t + \phi_0)] \end{aligned} \tag{5.5}$$

Let us introduce Fourier-Bessel expansion for $cos(msin\omega t)$ and $sin(msin\omega t)$ [79]:

$$\begin{aligned} \cos(msin(\omega_{rf} t)) &= J_0(m) + 2\sum_{k=0}^{\infty} J_{2k}(m) cos(2k\omega_{rf} t) \\ sin(msin(\omega_{rf} t)) &= 2\sum_{k=0}^{\infty} (-1)^k J_{2k+1}(m) cos((2k+1)\omega_{rf} t) \end{aligned} \tag{5.6}$$

Here, $J_k(m)$ are Bessel functions of the first kind of integer order.

$$\begin{aligned} I(t) \;=\; & I_0[J_0(m) sin(\omega_{ac} t + \phi_0) + 2\sum_{k=1}^{\infty} J_{2k}(m) cos(2k\omega_{rf} t) sin(\omega_{ac} t + \phi_0) + \\ & 2\sum_{k=0}^{\infty} J_{2k+1}(m) sin((2k+1)\omega_{rf} t) cos(\omega_{ac} t + \phi_0)] \end{aligned} \tag{5.7}$$

By using trigonometric relations, the Josephson current becomes :

$$\begin{aligned} I(t) \;=\; & I_0[J_0(m) sin(\omega_{ac} t + \phi_0) + 2\sum_{l=1}^{\infty} J_l(m)[sin[(l\omega_{rf} + \omega_{ac})t + \phi_0] \\ & -(-1)^l sin[(l\omega_{rf} - \omega_{ac})t + \phi_0]] \end{aligned} \tag{5.8}$$

$$V_n = \pm n \frac{\hbar \omega_{rf}}{2e} \tag{5.9}$$

The time-averaged current vanishes except for the case $n\omega_{rf} = \frac{2eV_0}{\hbar} = \omega_{ac}$. When the AC Josephson current frequency (ω_{ac}) equals to the integer multiple of the radio frequency,($\omega_{ac} = \pm n\omega_{rf}$) constant voltage steps are occured in voltage current characteristics of the Josephson junction. These steps are called Shapiro Steps after their discovery in superconductor by Sidney Shapiro [80, 81].

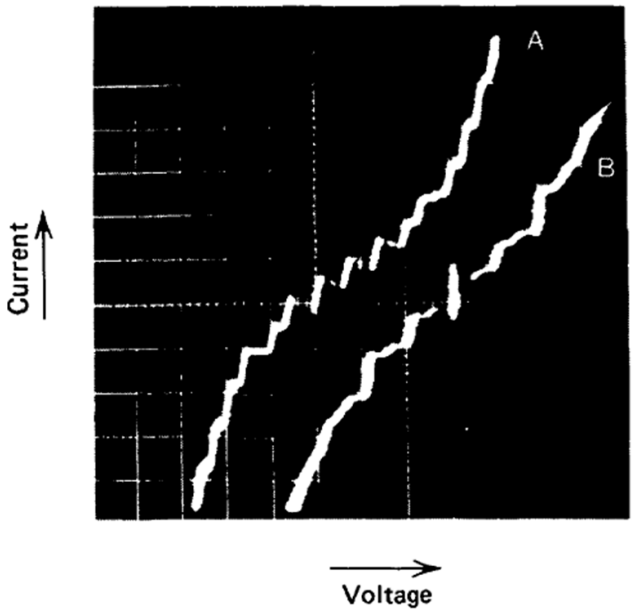

Figure 5.1: Current-Voltage charactistics of Josephson Junction [42].

5.1 Shapiro Resonances in Damped Driven BJJ systems

The realization of Shapiro resonances in Bosonic Josephson Junction (BJJ) systems are proposed in Ref. [82, 83]. The equations of motion for the damped and driven systems are:

$$\dot{\phi} = \Lambda z + \frac{z}{\sqrt{1-z^2}} \cos\phi + \varepsilon \cos \Omega t = \Delta\mu/\hbar \tag{5.10}$$

$$\dot{z} = -\sqrt{1-z^2} \sin\phi - \gamma\dot{\phi}, \tag{5.11}$$

Here, the potential of double well trap is harmonically time dependent. This results in a periodic shift of the chemical potential difference $\Delta\mu$ with amplitude ϵ. The effective interaction constant is represented with Λ and external driving frequency is denoted by Ω. The last term in Eq. 5.11 is introduced to describe the dissipative current. In Fig. 5.2, the stochastic character of the dynamical process is considered. Starting from the same initial value $Z(0)$, population imbalance is shown as a function of the time after the connection for a collection of uniformly distributed initial values of ϕ. The shapiro resonances is of the order of 0.1, in good agreement with systematic numerical

simulations [82, 83]. The realization of Shapiro is not simple, no consecutive relation between the initial phase and shapiro is exist.

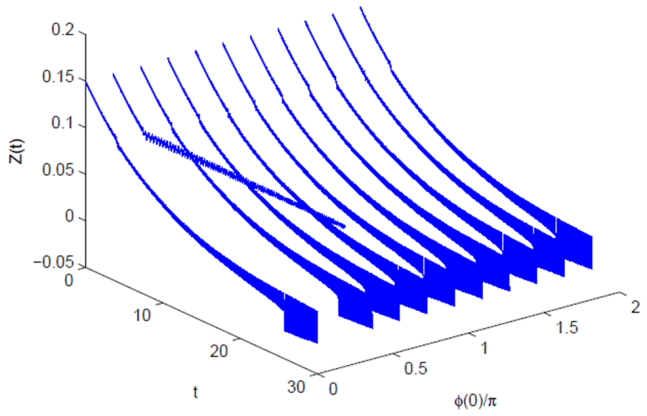

Figure 5.2: The shapiro resonances in BJJ system ($\bar{z} = 0.1$). Population imbalance $z(t)$ vs t and different collection of initial values of relative phase ϕ. The parameters are $\Lambda = 1 \times 10^4$, $\gamma = 1 \times 10^{-5}$, $\Omega = 1 \times 10^3$, $\epsilon = 100$.

5.2 Shapiro Resonaces in Damped Driven DWSP-JJ System

We have investigated surface-plasmon-soliton coupled system in the presence of AC driving. As the system goes towards to equilibrium under damping, the effect of damping can be compensated with an external driving. Hence, system has an appreciable possibility of being trapped in Shapiro resonances. In order to investigate Shapiro resonances, we adopt the model Ref. [82, 83] (Eq. 5.11). The equations of motion for DWSP-JJ systems is in the following :

$$\dot{\phi} = \tilde{\Lambda} Z + \tilde{q} \frac{Z}{\sqrt{1 - Z^2}} \cos\phi + \tilde{\varepsilon} \cos t \tag{5.12}$$

$$\dot{Z} = -\tilde{q}\sqrt{1 - Z^2} \sin\phi - \zeta\dot{\phi}, \tag{5.13}$$

In the presence of an ac driving, Shapiro resonance is formed in the phase space for values of Z :

$$\bar{Z}\Lambda = k\Omega \tag{5.14}$$

$$\frac{d\bar{Z}}{dt} = 0 \tag{5.15}$$

where k is an integer, $\bar{Z}$ average number of population imbalance.

The existence and the stability of so-called phase-locked solutions, where small fluctuations are considered, are investigated in DWSP-JJ model by introducing the Ansatz [82, 83]:

$$\dot{\phi} = qZ\cos\phi + \Lambda Z + \varepsilon\cos(\Omega t) \tag{5.16}$$

$$\dot{Z} = -q\sin\phi + \beta\dot{\phi} \tag{5.17}$$

We are interested in $\delta\phi$, and δZ to display only slow, decaying oscillations around a stationary solution $\delta\phi = const$ and $\delta Z = 0$. The equations of motion for $\delta\phi$, δZ are obtained by substituting Eq. 5.18 and Eq. 5.19 into Eq. 5.16 and Eq. 5.17. The resulting system of equations involves rapidly oscillating coefficients of period $2\pi/\Omega$. The different time scales can be separated consistently and all time-dependent coefficients can be replaced by their time averages and $|Z| << 1$.

$$\phi = k\Omega t + \frac{\varepsilon}{\Omega}\sin(\Omega t) + \delta\phi \tag{5.18}$$

$$Z = \frac{k\Omega}{\Lambda} + \beta\cos(k\Omega t) + \delta Z \tag{5.19}$$

$$\dot{\phi} = k\Omega + \varepsilon\cos(\Omega t) + \frac{d}{dt}\delta\phi \tag{5.20}$$

$$\dot{Z} = -\beta\sin(k\Omega t)k\Omega + \frac{d}{dt}\delta Z \tag{5.21}$$

$$\dot{Z} = -q\sin[k\Omega t + \frac{\varepsilon}{\Omega}\sin(\Omega t) + \delta\phi] - \gamma[k\Omega + \varepsilon cos(\Omega t) + \frac{d}{dt}\delta\phi] \tag{5.22}$$

by using the trigonometric relation $\sin(a+b) = \sin a\cos b + \sin b\cos a$ with $a = k\Omega t + \frac{\varepsilon}{\Omega}$ and $b = \delta\phi$, we rewrite Eq. 5.22 :

$$\begin{aligned}\dot{Z} &= -q(\sin[k\Omega t + \frac{\varepsilon}{\Omega}sin(\Omega t)]\cos(\delta\phi) + \cos[k\Omega t + \frac{\varepsilon}{\Omega}\sin(\Omega t)]\sin(\delta\phi)) \\ &\quad -\gamma[k\Omega + \varepsilon\cos(\Omega t) + \frac{d}{dt}\delta\phi]\end{aligned} \tag{5.23}$$

we take the advantage of trigonometric relation $\sin(e+f) = \sin e \cos f + \cos e \sin f$ with $e = k\Omega t$ and $f = \frac{\varepsilon}{\Omega}\sin(\Omega t)$, we rewrite Eq. 5.23

$$\begin{aligned}\dot{Z} &= -q\sin(k\Omega t)\cos(\frac{\varepsilon}{\Omega}\sin(\Omega t))\cos(\delta\phi) - q\cos(k\Omega t)\sin(\frac{\varepsilon}{\Omega}\sin(\Omega t))\cos(\delta\phi) \\ &\quad -q\cos[k\Omega t + \frac{\varepsilon}{\Omega}\sin(\Omega t)]sin(\delta\phi) - \gamma[k\Omega + \varepsilon\cos(\Omega t) + \frac{d}{dt}\delta\phi] \qquad (5.24)\end{aligned}$$

By taking the average of Eq. 5.24, we have :

$$\begin{aligned}-\frac{\Omega}{2\pi}\int_0^{\frac{2\pi}{\Omega}}\sin(k\Omega t)d\tau + \frac{\Omega}{2\pi}\int_0^{\frac{2\pi}{\Omega}}\frac{d}{dt}\delta Z d\tau &= -q\frac{\Omega}{2\pi}\int_0^{\frac{2\pi}{\Omega}} sin(k\Omega t) \\ &\quad \cos(\frac{\varepsilon}{\Omega}\sin(\Omega t))\cos(\delta\phi)d\tau \\ &\quad -q\frac{\Omega}{2\pi}\int_0^{\frac{2\pi}{\Omega}}\cos(k\Omega t) \\ &\quad \sin(\frac{\varepsilon}{\Omega}\sin(\Omega t))\cos(\delta\phi)d\tau \\ &\quad -q\frac{\Omega}{2\pi}\int_0^{\frac{2\pi}{\Omega}}\cos[k\Omega t + \frac{\varepsilon}{\Omega}\sin(\Omega t)]\sin(\delta\phi)d\tau \\ &\quad -\frac{\Omega}{2\pi}\int_0^{\frac{2\pi}{\Omega}}\gamma[k\Omega + \varepsilon\cos(\Omega t) + \\ &\quad \frac{d}{d\tau}\delta\phi]d\tau \qquad (5.25)\end{aligned}$$

$$\begin{aligned}\frac{d}{dt}\delta Z &= -q\frac{\Omega}{2\pi}\int_0^{\frac{2\pi}{\Omega}}\cos[k\Omega t + \frac{\varepsilon}{\Omega}\sin(\Omega t)]\sin(\delta\phi)d\tau \\ &\quad -\frac{\Omega}{2\pi}\int_0^{\frac{2\pi}{\Omega}}\gamma[k\Omega + \frac{d}{d\tau}\delta\phi]d\tau \qquad (5.26)\end{aligned}$$

By exploiting k^{th} order first kind Bessel functions $J_n(x) = \frac{1}{\pi}\int_0^{\pi}\cos(n\tau - x\sin\tau)d\tau$

$$\frac{d}{dt}\delta Z = -qJ_k(\frac{\varepsilon}{\Omega})\sin\delta\phi - \gamma k\Omega - \gamma\frac{d}{dt}\delta\phi \qquad (5.27)$$

Now we take the average by considering $k\Omega = \Lambda\bar{Z}$ yields :

$$k\Omega + \frac{d}{dt}\delta\phi = qZ\cos\phi + \Lambda\bar{Z} \qquad (5.28)$$

$$\frac{d}{dt}\delta\phi = \Lambda\delta Z \qquad (5.29)$$

Finally, we obtain equations of motion with the new canonical coordinates $\delta\phi$ and δZ which describe a dissipative particle with the dissipative force $F = -\gamma\Lambda\delta Z$:

$$\begin{aligned} \tfrac{d}{dt}\delta Z &= -qJ_k(\tfrac{\varepsilon}{\Omega})\sin\delta\phi - \gamma k\Omega - \gamma\Lambda\delta Z \\ \tfrac{d}{dt}\delta\phi &= \Lambda\delta Z \end{aligned} \tag{5.30}$$

In order to observe Shapiro resonances, we decided for the values of Z and ϕ by considering damped driven non-rigid pendulum system in Ref. [82, 83], and scaled the dynamical equations with external driving frequency Ω as $\tilde{t} = \Omega t$, $\tilde{\Lambda} = \Lambda/\Omega$, $\tilde{\varepsilon} = \varepsilon/\Omega$, $\tilde{q} = q/\Omega$. The dynamical equations are solved similar to BJJ. We found shapiro resonances at the same time-averaged value $\bar{Z} = 0.1$ for $\Delta E = 0$, $\Lambda = 0.1$, $\zeta = 8 \times 10^{-5}$, $\Omega = 0.01$, $\varepsilon = 1 \times 10^{-4}$, $q(Z) = 1 \times 10^{-5}$ (Fig. 5.3). In Fiq. 5.3, due to the dissipative current in the Eq. 5.13 the population imbalance Z decays towards the equilibrium. The dynamics is the same as in undriven case except for the small kink (blue line), which exhibits an Shapiro resonances. In this case, system gets trapped in the resonance island and the transient decay comes to a standstill instead of continuing towards the equilibrium solution. The system oscillates with driven amplitude ε around non-zero value. In Fig. 5.4, the collection of different initial relative phase and same initial population imbalance are plotted to show the Shapiro resonances.

Next, we describe the system in phase plane for various distance values $kd = 15, 19, 24$ with parameters $\Lambda = 0.1$, $\Omega = 0.01$, $\varepsilon = 1 \times 10^{-3}$, $\zeta = 0$ at stroboscopic time. In the absence of damping, we observed Shapiro resonances for different population imbalances in Fig. 5.5(a) $kd = 15$, (b) $kd = 19$, (c) $kd = 24$, respectively. The coupling parameter $q = e^{-kd\sqrt{2\Lambda(1+Z)}}$ is exponentially related to the kd. Therefore by increasing kd coupling parameter reduces and decoupling occurs. According to decoupling, for certain relative phases in driven system, photon has no tunnelling between surface plasmon and soliton dominant modes. It is trapped one of these modes, and system exhibits shapiro resonances. In Fig. 5.5(a) resonances are mostly at $\bar{Z} = 0.1$ and $\bar{Z} = -0.1$ whereas in Fig. 5.5(b) $kd = 19$ multiple resonances are observed. The resonances are not related to the increase of kd. For instance, in

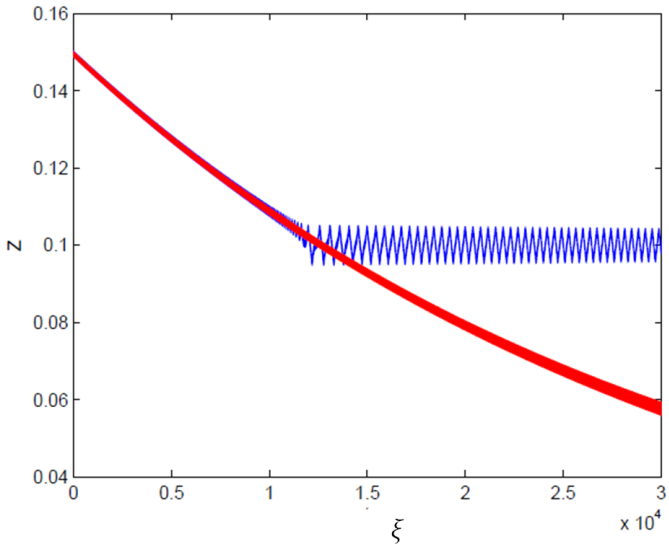

Figure 5.3: Initial value of population imbalance $Z(0) = 0.15$ with initial value of relative phase $\phi(0) = 9\pi/5$. The parameters $\Lambda = 0.1$, $\zeta = 8 \times 10^{-5}$, $\Omega = 0.01$, $q(Z) = 1 \times 10^{-5}$. The driven case $\varepsilon = 1 \times 10^{-3}$, Shapiro resonances at $\bar{Z} = 0.1$ (blue line). For the undriven case ($\varepsilon = 0$), under damped system decays towards equilibrium (red line).

Fig. 5.5(c) for $kd = 24$, most of Shapiro resonances disappears. Shapiro occurs only for certain initial values of relative phases at stroboscopic times. In the following, we investigate the driven ($\varepsilon = 1 \times 10^{-3}$) and damped ($\zeta = 1 \times 10^{-4}$) system for $kd = 19$ and $kd = 24$, respectively. In order to show the Shapiro effect, same initial $Z(0)$ with different two initial values of relative phases are plotted on the same figure. At some certain initial relative phases, no transition between surface plasmon and soliton occurs, system is trapped. In Fig. 5.6(a) for $kd = 19$ with $Z(0) = 0.12$, $\phi(0) = 0.4$(blue-line) initially system in soliton dominant mode and decays slowly towards its equilibrium value $\bar{Z} = 0$ whereas at $\phi(0) = 0$, $\bar{Z} = 0.1$ (red-line) shapiro resonances are observed. Photon is trapped in the soliton dominant mode no transition to surface plasmon exist. In Fig. 5.6(b) $kd = 19$ system is in soliton dominant mode with $Z(0) = 0.15$, $\phi(0) = -0.3$(blue-line) and system decays to $\bar{Z} = 0$, but for $\phi(0) = 0.8$, $\bar{Z} = 0.1$ (red-line) it is trapped in soliton dominant mode.

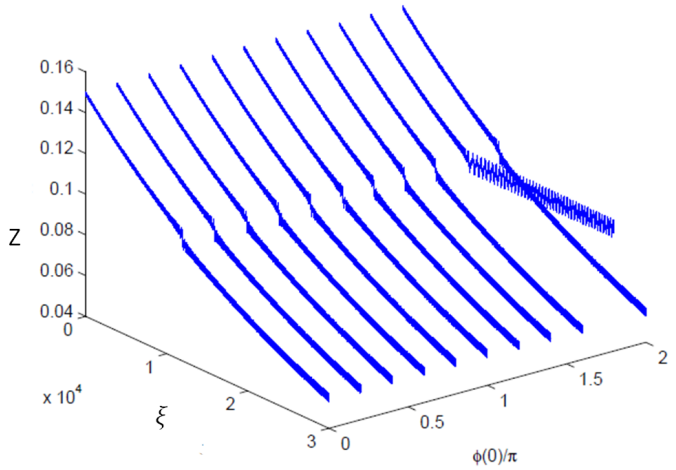

Figure 5.4: The shapiro resonances in DWSP-JJ system ($\bar{Z} = 0.1$). Population imbalance Z vs ξ and different collection of initial values of relative phase ϕ. The parameters are $\Lambda = 0.1$, $\zeta = 8 \times 10^{-5}$, $\Omega = 0.01$, $\varepsilon = 1 \times 10^{-3}$, and $q(Z) = 1 \times 10^{-5}$

.

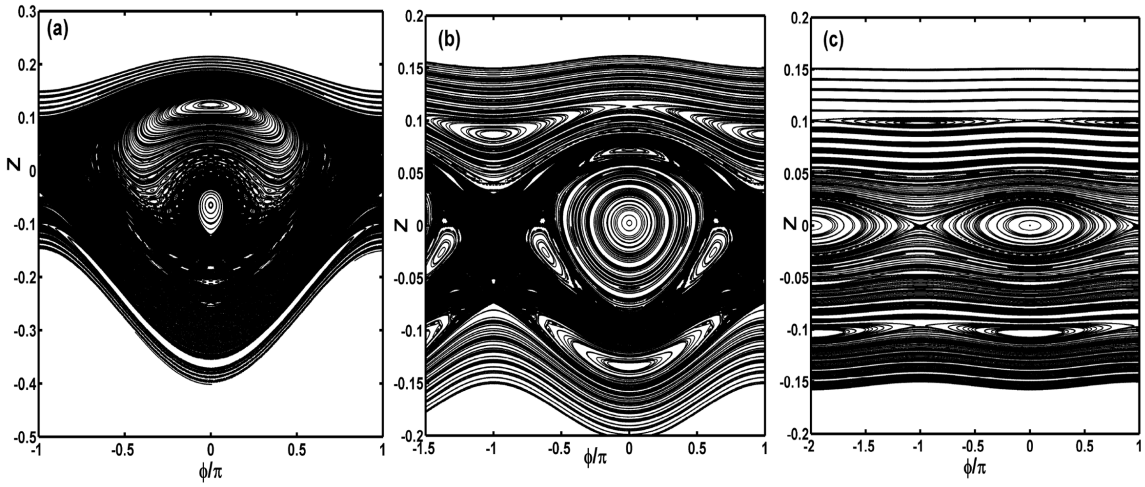

Figure 5.5: Phase portraits of the driven $\varepsilon = 1 \times 10^{-3}$ undamped $\zeta = 0$ system at stroboscopic times $2\pi/\Omega(1 : 4000)$, $\Lambda = 0.1$, $\Omega = 0.01$, (a) $kd = 15$ (b)$kd = 19$ (c) $kd = 24$.

In Fig. 5.7(a) for $kd = 24$ with initially soliton dominant mode $Z(0) = 0.12$, $\phi(0) = 0.7$(blue-line) system decays to equilibrium value $\bar{Z} = 0$. At $\phi(0) = -0.3$, $\bar{Z} = 0.1$

(red-line) shapiro islands are observed. In Fig. 5.7(b) $kd = 24$ with initially surface plasmon dominant mode $Z(0) = -0.15$, $\phi(0) = -0.7$(blue-line) system decays to $\bar{Z} = 0$, but for $\phi(0) = -0.1$, $\bar{Z} = -0.1$ (red-line), photon is trapped in surface plasmon dominant mode.

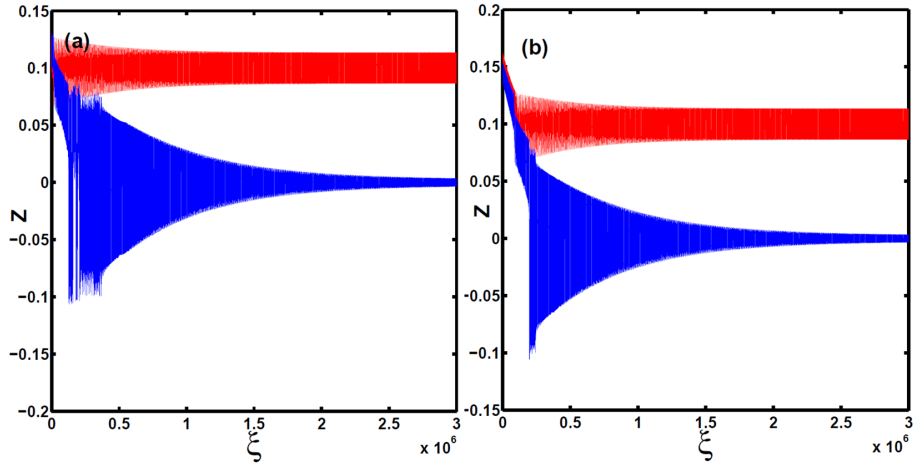

Figure 5.6: The driven and damped system. Population imbalance vs ξ; $kd = 19$, $\Lambda = 0.1$, $\zeta = 1 \times 10^{-4}$, $\varepsilon = 1 \times 10^{-3}$, $\Omega = 0.01$ (a) $Z(0) = 0.12$, $\phi(0) = 0.4$, $\phi(0) = 0$ (b)= $Z(0) = 0.15$, $\phi(0) = -0.3$, $\phi(0) = 0.8$.

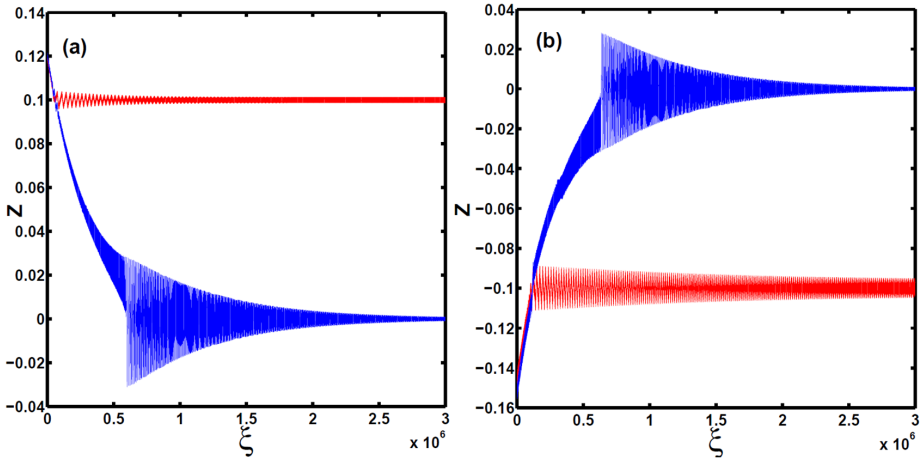

Figure 5.7: The driven and damped system. Population imbalance vs ξ; $kd = 24$, $\Lambda = 0.1$, $\zeta = 1 \times 10^{-4}$, $\varepsilon = 1 \times 10^{-3}$, $\Omega = 0.01$ (a) $Z(0) = 0.12$, $\phi(0) = 0.7$, $\phi(0) = -0.3$ (b)= $Z(0) = -0.15$, $\phi(0) = -0.7$, $\phi(0) = -0.1$.

In order to investigate the effect of damping on shapiro resonance at same driving $\varepsilon = 1 \times 10^{-3}$, we increase the value of the damping. Here, we consider Fig. 5.6(a), Fig. 5.6(b) and Fig. 5.7(a), Fig. 5.7(b) respectively. In Fig. 5.8(a) the damping value is $\zeta = 2.2 \times 10^{-4}$ whereas $\zeta = 1.1 \times 10^{-4}$ in Fig. 5.9(a). The Shapiro island at soliton dominant mode, decays towards to $\bar{Z} = 0$. It occurs at $\bar{Z} = 0.1$ for both in Fig. 5.6(a) and Fig. 5.6(b). The Fig. 5.8(b) and Fig. 5.9(b) show the breaking point of shapiro by zoom at $\bar{Z} = 0.1$. The driving of the system is not sufficient to overcome the damping. System can not be trapped. Photon travels to mixed phase modes. In Fig. 5.10(a)

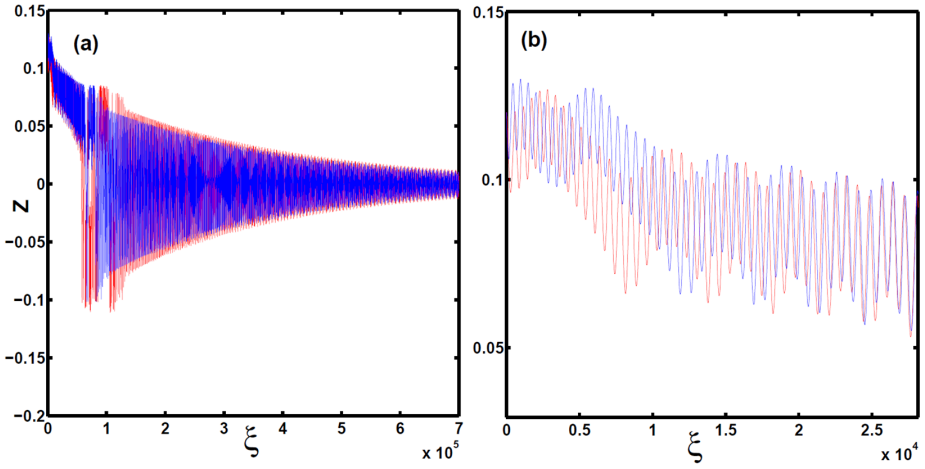

Figure 5.8: The driven and damped system. Population imbalance vs ξ; $kd = 19$, $\Lambda = 0.1$, $\varepsilon = 1 \times 10^{-3}$, $\Omega = 0.01$ (a) $\zeta = 2.2 \times 10^{-4}$, $Z(0) = 0.12$, $\phi(0) = 0.4$, $\phi(0) = 0$ (b)Figure with zoom in.

and in Fig. 5.11(a) the damping values are same $\zeta = 1.1 \times 10^{-4}$. The shapiro resonance in Fig. 5.7(a) at soliton dominant mode $\bar{Z} = 0.1$ by increasing damping, photon travels to mixed phase modes $\bar{Z} = 0$. The breaking point of shapiro is given by zoom in Fig. 5.10(b)(red-line). In Fig. 5.7(b) shapiro resonance at surface plasmon dominant mode $\bar{Z} = -0.1$ by increasing damping, photon travels to mixed phase modes $\bar{Z} = 0$. The breaking point of shapiro is given by zoom in Fig. 5.11(a)(red-line). The Shapiro occurs at $\bar{Z} = 0.1$ for Fig. 5.7(a) and Fig. 5.6(b). The Fig. 5.8(b) shows the breaking point of shapiro by zoom at $\bar{Z} = 0.1$.

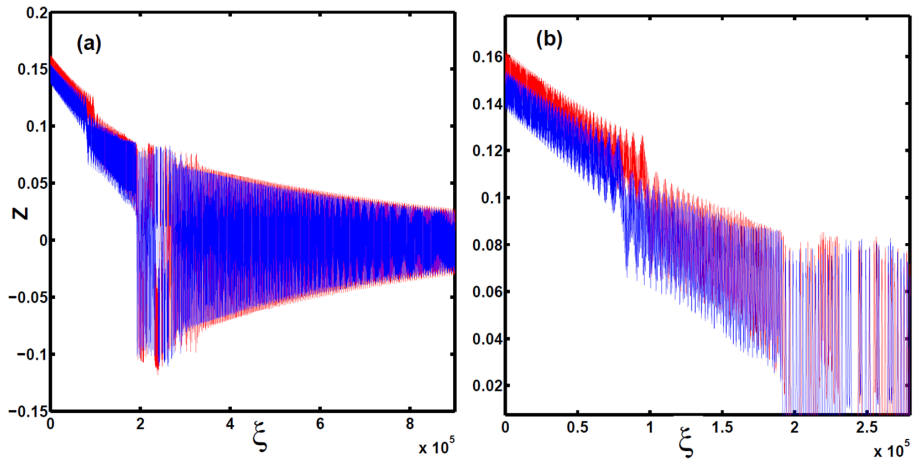

Figure 5.9: The driven and damped system. Population imbalance vs ξ; $kd = 19$, $\Lambda = 0.1$, $\varepsilon = 1 \times 10^{-3}$, $\Omega = 0.01$ (a)$\zeta = 1.1 \times 10^{-4}$ $Z(0) = -0.15$, $\phi(0) = -0.3$, $\phi(0) = 0.8$ (b)Figure with zoom in.

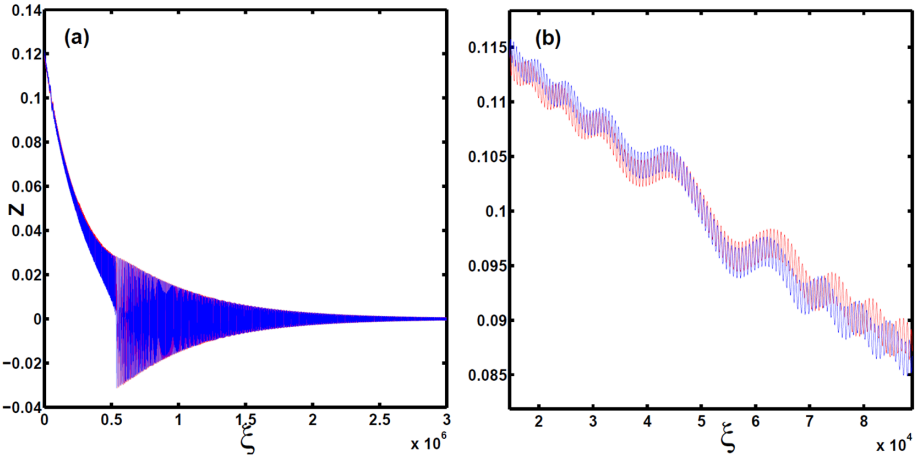

Figure 5.10: The driven and damped system. Population imbalance vs ξ; $kd = 24$, $\Lambda = 0.1$, $\varepsilon = 1 \times 10^{-3}$, $\Omega = 0.01$ (a) $\zeta = 1.1 \times 10^{-4}$, $Z(0) = 0.12$, $\phi(0) = -0.3$, $\phi(0) = 0.7$ (b)Figure with zoom in.

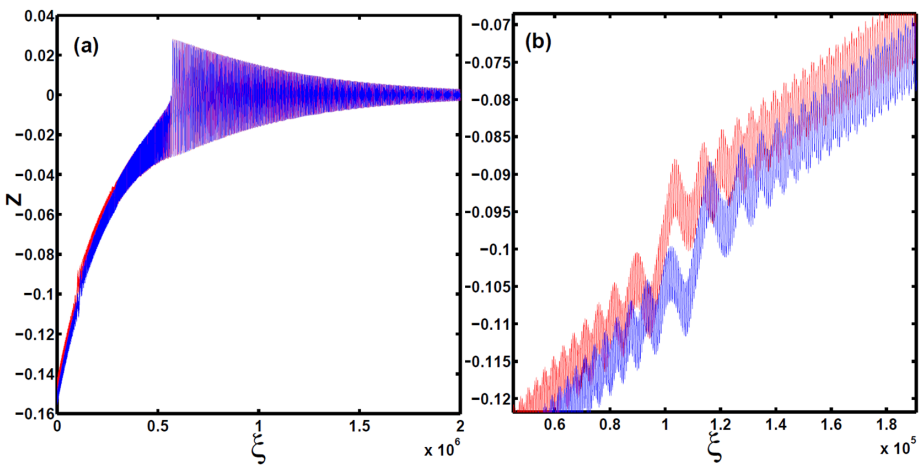

Figure 5.11: The driven and damped system. Population imbalance vs ξ; $kd = 24$, $\Lambda = 0.1$, $\varepsilon = 1 \times 10^{-3}$, $\Omega = 0.01$ (a) $\zeta = 1.1 \times 10^{-4}$, $Z(0) = -0.15$, $\phi(0) = -0.7$, $\phi(0) = -0.1$ (b)Figure with zoom in.

In Fig. 5.12(a)-(b) the control parameters are $kd = 24$, $\Lambda = 0.1$, $\varepsilon = 1 \times 10^{-3}$, $\Omega = 0.01$,with initial values $Z(0) = 0.12$, $\phi(0) = 0.7$, $\phi(0) = -0.3$, and in Fig. 5.13(a)-(b) $Z(0) = -0.15$, $\phi(0) = -0.7$, $\phi(0) = -0.1$. The increase of damping breaks the Shapiro resonances at short ξ. In Fig. 5.12(a), and Fig. 5.12(b), the behavior of the coupled system is shown for the same ξ with damping $\zeta = 1 \times 10^{-4}$ and $\zeta = 1.1 \times 10^{-4}$, respectively. And also, in Fig. 5.13(a), and Fig. 5.13(b) the system is presented for the same ξ with damping $\zeta = 1 \times 10^{-4}$ and $\zeta = 1.1 \times 10^{-4}$, respectively. The Fig. 5.12(a)and Fig. 5.13(a) exhibits Shapiro resonances whereas the Fig. 5.12(b)and Fig. 5.13(b) system decays to zero modes. Finally, we investigate the system for high ξ values. As an example, we worked with surface plasmon dominant mode $kd = 24$, $Z(0) = 0.12$, $\phi(0) = 0.7$, $\phi(0) = -0.3$. We keep the driving term $\varepsilon = 1 \times 10^{-3}$ and the damping value $\zeta = 1 \times 10^{-4}$. We worked with $\xi = 3 \times 10^{8}$ and observe that, shapiro resonances survived as in the case of $\xi = 3 \times 10^{6}$.

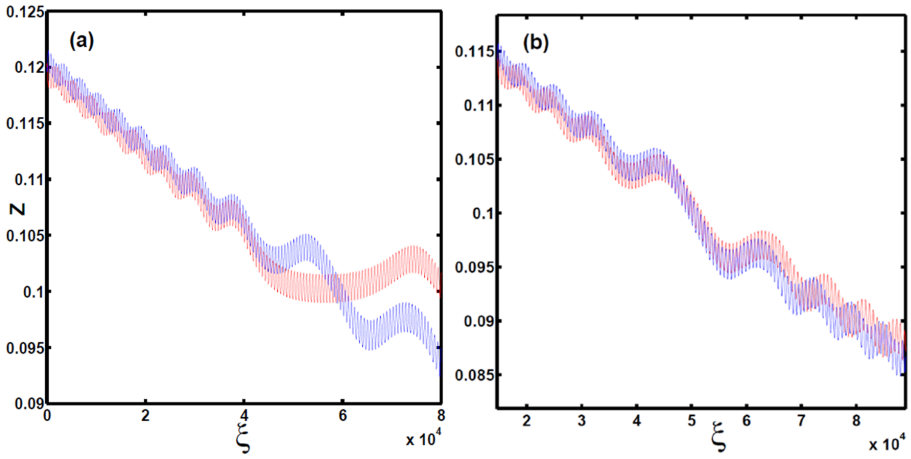

Figure 5.12: The driven and damped system. Population imbalance vs ξ; $kd = 24$, $\Lambda = 0.1$, $\varepsilon = 1\times10^{-3}$, $\Omega = 0.01$, $Z(0) = 0.12$, $\phi(0) = 0.7$, $\phi(0) = -0.3$ (a) $\zeta = 1\times10^{-4}$ (b)$\zeta = 1.1 \times 10^{-4}$.

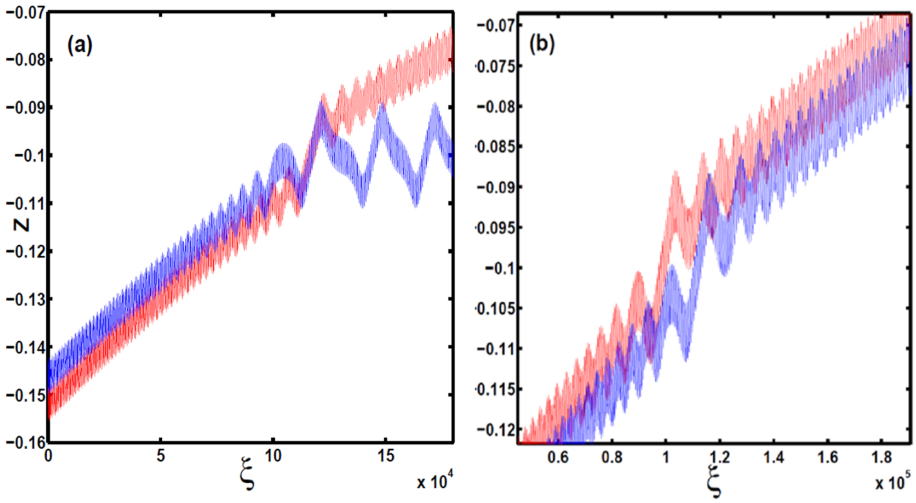

Figure 5.13: The driven and damped system. Population imbalance vs ξ; $kd = 24$, $\Lambda = 0.1$, $\varepsilon = 1 \times 10^{-3}$, $\Omega = 0.01$, $Z(0) = -0.15$, $\phi(0) = -0.7$, $\phi(0) = -0.1$ (a) $\zeta = 1 \times 10^{-4}$ (b)$\zeta = 1.1 \times 10^{-4}$.

Chapter 6

CONCLUSION AND OUTLOOK

In the presented work, we studied the dynamical behavior of the coupled optical soliton and surface plasmon system by using linear stability analysis method. We first discussed undamped and undriven cases under BJJ Analogy. In BJJ systems, the coupling parameter is constant whereas in DWSP-JJ model it is a dynamical parameter which changes with soliton amplitude. We have found that soliton amplitude dependent coupling parameter allows rich dynamical features, different than that observed in bosonic Josephson Junctions. The coupling parameter generates self-trapped oscillatory states at nonzero fractional populations. The fixed points of the coupled system showed one critical point at $\phi = 0$ whereas number of fixed points increases up to three under the various values of the control parameters kd, ΔE, ν_p, Λ at $\phi = \pi$. In BJJ systems, ΔE parameterizes the asymmetry of the energy levels populated by the atoms in the trap. In DWSP-JJ systems, ΔE parameterizes the asymmetry of the soliton and surface plasmon levels populated by the photons. When we increased kd by keeping other parameters constant, we found that additional fixed points occur at $\phi = \pi$. Two of them are stable and one is unstable. We observed that increase of Λ, reduces the number of fixed points at $\phi = \pi$. When we increased the ν_p, we found that both stable closed trajectory in the pure soliton mode and unstable fixed point at $\phi = \pi$ disappears, running trajectories dominates the system.

Next, we discussed damped and undriven coupled DWSP-JJ system. The damping effects are investigated by adding a phase-velocity damping term into the dynamical equations. In the presence of damping, we observed that fixed points take the role of sources and sinks in the phase space depending on the Jacobian eigenvalues. Damping also results in the so-called "phase-slip" effect where the π-phase modes decay into

zero-phase modes.

Finally, we discussed damped and driven DWSP-JJ system (under damping and external drive). By increasing the kd values of the system, we found that in addition to the expected Shapiro resonances, several resonance points emerge in the stroboscopic phase portrait, which may survive under weak dissipative conditions. However, Shapiro resonances are not only related to the value of the kd. We observe that they only exist at some certain initial relative phases. At that point, no tunneling between soliton and surface plasmon dominant modes occur and system is trapped. By the small amount of increase in damping, shapiro resonances decay to zero modes as a nature of damping.

6.1 Outlook

In this work, coupled system dynamics are investigated in a classical model. By progressing the present work, the dynamical behavior of the coupled DWSP-JJ system may be investigated in quantum model by introducing two-mode second quantized Bose-Hubbard type Hamiltonian. In a current model, we studied soliton and surface plasmon coupled system in two dimensions. However, different metal geometries can be studied. For instance, surface plasmons on corrugated metal surfaces, finite-size metal surfaces (metallic spheres) or surface plasmon dielectric array structures can be considered. In this work, we deal with the soliton (nonlinear) and surface plasmon (linear) coupled system. The coupling of nonlinear surface plasmons (nonlinear dielectric present on metal surface) with solitons generate two nonlinear systems that can be also studied.

Appendix A

THE LINERIZATION OF COUPLED HARMONIC OSCILLATOR EQUATIONS

$$\begin{aligned} \ddot{c}_p + \beta_p^2 &= q(|c_s|)c_s \\ \ddot{c}_s + \beta_s^2(|c_s|)c_s &= q(|c_s|)c_p \end{aligned} \tag{A.1}$$

Energy exchange occurs only near the resonance $\beta_p = \beta_s$

$|c_s|_{res} = \sqrt{4(\beta_p - 1)/\gamma}$.

In vicinity of resonance $|\beta_p - \beta_s| << \beta_p$, making substitution

$c_p = \mathscr{C}_p e^{i\xi}$ $c_s = \mathscr{C}_s e^{i\xi}$ and assuming that new amplitudes $|\mathscr{C}_{p,s}|$ vary very slowly as: $(|\dot{\mathscr{C}}_{p,s}| \ll |\mathscr{C}_{p,s}|)$

$$\begin{aligned} \dot{\mathscr{C}}_p &= \dot{\mathscr{C}}_p e^{i\xi} + i\mathscr{C}_p e^{i\xi} \\ \ddot{\mathscr{C}}_p &= |\ddot{\mathscr{C}}_p|e^{i\xi} + i|\dot{\mathscr{C}}_p|e^{i\xi} + i|\dot{\mathscr{C}}_p|e^{i\xi} - |\mathscr{C}_p|e^{i\xi} \\ \dot{\mathscr{C}}_s &= \dot{\mathscr{C}}_s e^{i\xi} + i\mathscr{C}_s e^{i\xi} \\ \ddot{\mathscr{C}}_s &= |\ddot{\mathscr{C}}_s|e^{i\xi} + i|\dot{\mathscr{C}}_s|e^{i\xi} + i|\dot{\mathscr{C}}_s|e^{i\xi} - |\mathscr{C}_s|e^{i\xi} \end{aligned} \tag{A.2}$$

$$\|\dot{\mathscr{C}}_s| = \frac{q\mathscr{C}_s - \mathscr{C}_p[\beta_p^2 - 1]}{2i} \tag{A.3}$$

$$|\dot{\mathscr{C}}_s| = \frac{q\mathscr{C}_p - |\mathscr{C}_s|[\beta_s^2 - 1]}{2i} \tag{A.4}$$

$$\begin{aligned} |\dot{\mathscr{C}}_p| &= \tfrac{q(|\mathscr{C}_s|)|\mathscr{C}_s| - |\mathscr{C}_p|[\beta_p^2 - 1]}{2i} \\ |\dot{\mathscr{C}}_s| &= \tfrac{q(\mathscr{C}_s)|\mathscr{C}_p| - |\mathscr{C}_p|[\beta_s^2 - 1]}{2i} \end{aligned} \tag{A.5}$$

$$\begin{aligned} i|\dot{\mathscr{C}}_p| &= \tfrac{q(|\mathscr{C}_s|)|\mathscr{C}_s|}{2} - |\mathscr{C}_p|\tfrac{(\beta_p^2 - 1)}{2} \\ i|\dot{\mathscr{C}}_s| &= \tfrac{q(|\mathscr{C}_s|)|\mathscr{C}_p|}{2} - |\mathscr{C}_p|\tfrac{(\beta_s^2 - 1)}{2} \end{aligned} \tag{A.6}$$

by considering;

$$\begin{aligned} v_p &\equiv (\beta_p - 1) \ll 1 \\ v_s &\equiv (\beta_s - 1) \ll 1 \end{aligned}$$

$\beta_p^2 - 1$ can be written in terms of v_p. $\beta_p^2 = v_p(v_p + 2) = v_p^2 + 2v_p$. Similarly $\beta_s^2 = v_s(v_s + 2) = v_s^2 + 2v_s$ we can neglect v_p^2 and v_s^2:

$$\begin{aligned} -i|\dot{\mathscr{C}}_p| &= |\mathscr{C}_p|v_p - \tfrac{q|\mathscr{C}_s|}{2} \\ -i|\dot{\mathscr{C}}_s| &= |\mathscr{C}_s|v_s - \tfrac{q|\mathscr{C}_p|}{2} \end{aligned} \tag{A.7}$$

Appendix B

THE DYNAMICAL EQUATIONS OF THE DWSP-JJ IN BOSONIC JOSEPHSON ANALOGY

We would like to describe the DWSP-JJ system in terms of BJJ equations.

$$\begin{aligned} -i|\dot{C}_p| &= |C_p|v_p - \tfrac{q(C_s)|C_s|}{2} \\ -i|\dot{C}_s| &= |C_s|v_s - \tfrac{q(C_s)|C_p|}{2} \end{aligned} \tag{B.1}$$

let us substitude $\mathscr{C}_p = |C_p|e^{i\phi_p}$ with $\mathscr{C}_s = |C_s|e^{i\phi_s}$ into Eq.(B.1), and introduce the relative phase between soliton and surface plasmon-soliton ϕ. Next. we separate the real and imaginary parts yields :

$$\begin{aligned} &-i|\dot{C}_p|e^{i\phi_p} + i\dot{\phi_p}|C_p|e^{i\phi_p} = |C_p|e^{i\phi_p}v_p - \tfrac{q}{2}|C_s|e^{i\phi_s} \\ &e^{i\phi_p}[-i|\dot{C}_p| + |C_p|(\dot{\phi_p} - v_p)] = -\tfrac{q}{2}|C_s|e^{i\phi_s} \\ &\phi = \phi_s - \phi_p \\ &-i|\dot{C}_p| + |C_p|(\dot{\phi_p} - v_p) = -\tfrac{q}{2}|C_s|e^{i\phi} \\ &-i|\dot{C}_p| + |C_p|(\dot{\phi_p} - v_p) = -\tfrac{q}{2}|C_s|(\cos\phi + i\sin\phi) \\ &\qquad\qquad |\dot{C}_p| = \tfrac{q}{2}|C_s|\sin\phi \\ &\qquad\qquad \dot{\phi}_p = -\tfrac{q}{2}\tfrac{|C_s|}{|C_p|}\cos\phi + v_p \end{aligned} \tag{B.2}$$

$$\begin{aligned} &-i|\dot{C}_s|e^{i\phi_s} + i\dot{\phi_s}|C_s|e^{i\phi_s} = |C_s|e^{i\phi_s}v_s - \tfrac{q}{2}|C_s|e^{i\phi_p} \\ &e^{i\phi_s}[-i|\dot{C}_s| + |C_s|(\dot{\phi_s} - v_s)] = -\tfrac{q}{2}|C_p|e^{i\phi_p} \\ &-i|\dot{C}_s| + |C_s|(\dot{\phi_s} - v_s) = -\tfrac{q}{2}|C_p|e^{-i\phi} \\ &-i|\dot{C}_s| + |C_s|(\dot{\phi_s} - v_s) = -\tfrac{q}{2}|C_p|(\cos\phi - i\sin\phi) \\ &\qquad\qquad |\dot{C}_s| = -\tfrac{q}{2}|C_p|\sin\phi \\ &\qquad\qquad \dot{\phi}_s = -\tfrac{q}{2}\tfrac{|C_p|}{|C_s|}\cos\phi + v_s \end{aligned} \tag{B.3}$$

We introduce the population imbalance Z and total field N :

$$\dot{\phi} = \dot{\phi_s} - \dot{\phi_p}$$
$$\dot{\phi} = -\frac{q}{2}\frac{|C_p|}{|C_s|}\cos\phi + v_s + \frac{q}{2}\frac{|C_s|}{|C_p|}\cos\phi + \nu_p$$
$$\nu_s \equiv \frac{\gamma|C_s|^2}{4}$$
$$\dot{\phi} = \frac{q}{2}\cos\phi\frac{|C_s|^2-|C_p|^2}{|C_s||C_p|} + \frac{\gamma|C_s|^2}{4} - \nu_p$$

$$N \equiv |C_p|^2 + |C_s|^2$$
$$Z = \frac{|C_s|^2-|C_p|^2}{N}$$
$$\sqrt{1-Z^2} = \sqrt{1-\frac{|C_s|^2-|C_p|^2}{|C_s|^2+|C_p|^2}} = \frac{2}{N}|C_s||C_p|$$
$$\dot{\phi} = \frac{q}{2}\frac{ZN\cos\phi}{|C_s||C_p|} + \frac{\gamma|C_s|^2}{4} - \nu_p$$
$$\frac{N}{|C_s||C_p|} = \frac{1}{\sqrt{1-Z^2}}$$
$$\dot{\phi} = \frac{qZ}{\sqrt{1-Z^2}}\cos\phi + \frac{\gamma|C_s|^2}{4} - \nu_p$$
$$\eta = \frac{\gamma N}{4}$$
$$\Lambda \equiv \frac{\eta}{2}$$
$$\Lambda(1+Z) = \Lambda(1+\frac{|C_s|^2-|C_p|^2}{N}) = \frac{2\Lambda|C_s|^2}{N}$$
$$\frac{\gamma|C_s|^2}{4} \equiv \Lambda(1+Z)$$
$$\dot{\phi} = \Lambda + \Lambda Z - v_p + \frac{qZ}{\sqrt{1-Z^2}}\cos\phi$$
$$\Delta E = \Lambda - \nu_p$$

Finally, we obtain the equations of motion for the DWSP-JJ system in terms of Z and ϕ in Eq. B.4, Eq. B.5 :

$$\dot{\phi} = \Lambda Z + \Delta E + \frac{qZ}{\sqrt{1-Z^2}}\cos\phi \tag{B.4}$$

$$\dot{Z} = \frac{2}{N}[|C_s||\dot{C_s}| - |C_p||\dot{C_p}]$$
$$\dot{Z} = \frac{2}{N}[-|C_s||C_p|\frac{q}{2}\sin\phi - |C_p||C_s|\frac{q}{2}\sin\phi]$$
$$\dot{Z} = -\frac{2}{N}q|C_s||C_p|\sin\phi$$
$$\dot{Z} = -q\sqrt{1-Z^2}\sin\phi \tag{B.5}$$

BIBLIOGRAPHY

[1] E. A. Stern and R. A. Ferrell, Phys. Rev. **120**, 130 (1960).

[2] W. L. Barnes, A. Dereux and T. W. Ebbesen, Nature **424**, 824 (2003).

[3] A. V. Zayats, I. I. Smolyaninov and A. A. Maradudin, Phys.Rep. **408**, 131 (2005).

[4] Stefan Alexander Maier, *Plasmonics: Fundamentals and Applications* (Springer, United Kingdom 2007).

[5] A. R. Davoyan, I. V. Shadrivov and Y. S. Kivshar, Optics Express **17**, 21732 (2009).

[6] S. I. Bozhevolnyi, *Plasmonic Nanoguides and Circuit* (Pan Stanford, Singapore 2009)

[7] Mark L. Brongersma, Pieter G. Kik, *Surface Plasmon Nanophotonics* (Springer, Netherlands 2007).

[8] E. Ozbay, Science **311**, 189 (2006).

[9] A. Otto, Z Phys. **216**, 398 (1968).

[10] Y. P. Bliokh, J. Felsteiner and Y. Z. Slutsker, Phys. Rev. Lett. **95**, 165003 (2005); Y. P. Bliokh, Opt. Commun. **259**, 436 (2006).

[11] S. I. Bozhevolnyi, V. S. Volkov , E. Devaux and T. W. Ebbesen Phys. Rev. Lett. **95**, 046802 (2005).

[12] R. Y. Chiao, E. Garmire and C. H. Townes Phys. Rev. Lett. **13(15)**, 479 (1964).

[13] Yuri S. Kivshar, Govind P. Agrawal, *Optical Solitons: from fibers to photonic crystals* (Academic Press, USA 2002).

[14] D. E. Chang, A. S. Sorensen, P. R. Hemmer and M. D. Lukin, Phys. Rev. Lett.**97**, 053002 (2006).

[15] K. Y. Bliokh, Y. P. Bliokh and A. Ferrando, Phys. Rev. A **79**, 041803R (2009).

[16] E. Feigenbaum and M. Orenstein, Opt. Lett. **32**, 674 (2007).

[17] H. Raether, *Surface Plasmons on Smooth and Rough Surfaces and on Gratings* (Springer-Verlag, 1988)

[18] Anatoly V. Zayats, Igor I. Smolyeninov, Alexei A. Mardudin, Physics Reports **408**, 131 (2005).

[19] R. H. Ritchie, Phys. Rev. **106**, 874 (1957).

[20] C. J. Powell , J. B. Swan, Phys. Rev. **118**, 640 (1960).

[21] Charles Kittel, *Introduction to Solid State Physics* (Wiley, USA 1995).

[22] J. S. Russell, Rep. 14th Meet. Brit. Assoc. Adv. Sci **pp 311-390** (1844).

[23] N. J. Zabusky and M. D. Kruskal, Phys.Rev.Lett **15**, 240 (1965).

[24] $http://www.oscar.desu.edu/research/optical_solitons.html$

[25] A. Ciattoni, B. Crosignani, P. DiPorto, and A Yariv Opt. Soc. Am. B **22** 1384 (2005).

[26] K. Porsezian, V. C. Kuriakose (eds.), *Optical Solitons: theoretical and Experimental Challenges* (Springer, Berlin, New York 2003).

[27] Zakharov, Shabat, Sov.Phys.JETP **34**, 62 (1972).

[28] P. G. Drazin, R. S. Johnson, *Solitons: an Introduction* (Cambridge University Press, Great Britain 1989).

[29] J. S. Aitchison, A. M. Weiner, Y. Silberberg, M. K. Oliver, J. L. Jackel, D. E. Leaird, E. M. Vogel, P. W. Smith, Opt. Lett **15**, 471 (1990).

[30] J. S. Aitchison, Y. Silberberg, A. M. Weiner,D. E. Leaird, M. K. Oliver, J. L. Jackel, P. W. Smith, J. Opt. Soc. Am. **B 8**, 1290 (1991).

[31] A. Barthelemy, S. Maneuf, C. Froehly, Opt. Commun. **55**, 201 (1985).

[32] R. De. La. Fuente, A. Barthelemy, C. Froehly, Opt. Lett. **16**, 793 (1991).

[33] George I. A. Stegeman, N. Christodoulides Demetrios and S. Mordechai, Ieee Journal on Selected Topics in Quantum Electronics **6**, 6 (2000).

[34] B. D. Josephson, Phys. Lett **1**, 251 (1962).

[35] L. N. Cooper, Phys. Rev. **104**, 1189 (1956).

[36] J. Bardenn, L. N. Cooper and J. R. Scrieffer, Phys. Rev. **106**, 162 (1957).

[37] J. Bardenn, L. N. Cooper and J. R. Scrieffer, Phys. Rev. **108**, 1175 (1957).

[38] M. Albeiz, *Observation of a Bose-Einstein condensate in a single Josephson Junction* (PhD Thesis, University of Heidelberg 2005).

[39] B. D. Josephson, Phys. Lett. **1A**, 251 (1962).

[40] B. D. Josephson, Rev. Mod. Phys. **46**, 251254 (1974).

[41] F. Sols Physica B, **194**, 1389 (1994).

[42] A. Barone, G. Paterno, *Physics and Applications of the Josephson Effect* (Wiley, New York 1982).

[43] D. E. McCumber Journal of Applied Physics **39**, 3113 (1968).

[44] R.P. Feynman, *Lectures on Physics, volume 3* (Addison-Wesley, New York 1965).

[45] C. P. Poole, H. A. Farach, R. J. Creswick, *Superconductivity* (Academic Press, USA 1995) .

[46] M. Tinkham, *Introduction to Superconductivity* (Dover Publications, Inc. Mineola, New York 2004).

[47] M. Suzuki and I. S. Suzuki, *Lecture note on solid state physics Josephson Junction and DC SQUID* (Department of Physics, State University of New York at Binghamton, New York 2006).

[48] P. L. Anderson, J. W. Rowell, Phys. Lett **10**, 230 (1963).

[49] S. N. Bose, Z. Phys. Rev. **26**, 178 (1924).

[50] A. Einstein Sitzber, Kgl. Preuss. Akad. Wiss., **261** (1924).

[51] A. Einstein, Kgl. Sitzber. Preuss. Akad. Wiss.**3** (1925).

[52] L. P. Pitaevskii and S.Stringari, *Bose-Einstein Condensation* (Clarendon Press, Oxford 2003).

[53] C. J. Pethick and H. Smith *Bose-Einstein Condensation in Dilute Gases* Cambridge (ISBN 0-521-66194-3) (ISBN 0-5212004-66580-9)

[54] M. Anderson, J. Ensher, M. Matthews, C. Wieman and E. Cornell, Science **269**, 198 (1995).

[55] K. Davis, M. O. Mewes, M. Andrews, N. Van Druten, N. Durfee, D. Kurn and W. Ketterle, Phys. Rev. Lett. **75(22)**, 3969 (1995).

[56] J. Javanainen, Phys. Rev. Lett. **57**, 3164 (1986).

[57] N. Didier *The Josephson Effect in superconductors and quantum gases* (PhD. Thesis, University of Joseph Fourier 2010).

[58] I. Zapata, F. Sols and A. Leggett, Phys. Rev. A 57 **R28**, (1998).

[59] A. Smerzi, S. Fantoni, S. Giovanazzi and S. R. Shenoy, Phys. Rev. Lett. **79**, 4950 (1997).

[60] R. Gati and M. K. Oberthaler, J. Phys. B: At. Mol. Opt. Phys **40**, R61 (2007).

[61] F. Sols, in *Proceedings of the International School of Physics Enrico Fermi,* Ed. by M. Inguscio, S. Stringari, and C. Wieman (IOS Press, Amsterdam 1999).

[62] Hongwei Xiong, Shujuan Liu and Mingsheng Zhan, New J. Phys. **8**, 245 (2006).

[63] S. Raghavan, A. Smerzi, S. Fantoni and S. R. Shenoy, Phys. Rev. A **59**, 620 (1999).

[64] Yang Hong-Wei, Zuo Wei, Chin.Phys.Lett **24**, 620 (2007).

[65] Shankar Sastry, *Nonlinear Systems: Analysis,Stability and Control*(Springer-Verlag, New York 1999).

[66] Tom W. B. Kibble, Frank H. Berkshire, *Classical Mechanics* (Imperial College Press, London 2004).

[67] Y. Ekşioğlu , Ö. E. Müstecaplıoğlu ,K. Güven, Phys. Rev. A **84**, 033805 (2011).

[68] I. Marino , S. Raghavan , S. Fantoni , S. R. Shenoy and A. Smerzi, Phys. Rev. A **60**, 487 (1999).

[69] Asobe, T. Kanamori and K. Kubodera, IEEE J. Quantum Electron **29**, 2325 (1993).

[70] M. Chauvet, G. Fanjoux, K. P. Huy, V. Nazabal, F. Charpentier, T. Billeton, G. Boudebs, M. Cathelinaud and S. P. Gorza, Optics Letters **34**, 1804 (2009).

[71] G. P. Agrawal, *Nonlinear Fiber Optics* (Academic Press, USA 2007)

[72] T. Kaczmarek, Adv. Electr. and Telecomm. **1**, 59 (2010).

[73] J. Williams, R. Walser, J. Cooper, E. Cornell and M. Holland, Phys. Rev. A **59**, R31 (1999).

[74] I. Marino, S. Raghavan, S. Fantoni, S. R. Shenoy and A. Smerzi, Phys. Rev. A **60**, 487 (1999).

[75] F. Bloch, Phys. Rev. B **2**, 109 (1970).

[76] T. A. Fulton, Phys. Rev. B **7**, 981 (1973).

[77] B. N. Taylor, W. H. Parker, D. N. Langenberg and A. Denestein, Metrologia **3**, 89 (1967).

[78] R. Pöpel, Metrologia **29**, 153 (1992).

[79] M. Abramowitz and I. A. Stegun *Handbook of Mathematical Functions: with Formulas, Graphs, and Mathematical Tables* (Dover Publications, 1965).

[80] S. Shapiro, Phys. Rev. Lett **11**, 80 (1963).

[81] W. C. Stewart, Applied Physics Letters **474**, 589 (1968).

[82] F. Sols and S. Kohler, Laser Physics **14**, 1259 (2004) .

[83] F. Sols and S. Kohler, New J.Phys. **5**, 94 (2003).

VITA

Yasa Ekşioğlu Özok was born in Istanbul, Turkey. She received her B.Sc. degree in Physics Department from Istanbul University, in 2002. She accepted for the M.Sc. Programme in Physics at the same University in the same year. In 2003-2004, with a INFM Research Unit fellowship, she attended research activities on the subject of "Quantum Atomic Gases" in Pisa at Scuola Normale Superiore, under the responsibility of Prof. Dr. Mario Tosi. In 2006, she graduated as a M.Sc. under the supervision of Prof. Dr. Zehra Akdeniz and co-supervision Prof. Dr. Mario Tosi with thesis entitled *"Bose-Einstein Yoğunlaşmasıyla Lineer Sıralanmış çeşitli Potansiyel Kuyularından Madde İletimi "* from Istanbul University. In 2007, she started Ph.D. studies under the supervision of Assoc. Prof. Özgür E. Müstecaplıoğlu in Koç University Material Science and Engineering programme and in 2008, she transferred to Physics programme in the same University. In 2009, she started the work under the supervision of Assist.Prof. Kaan Güven. From August 2007 to August 2011 she worked as a teaching assistant in Koç University. She is currently working on the nonlinear dynamical analysis of optical soliton surface metal coupled systems.